
Parametric Instabilities of Interacting Bosons in Driven Optical Lattices

Jakob Näger



München, 2019

Parametric Instabilities of Interacting Bosons in Driven Optical Lattices

Dissertation
an der Fakultät für Physik
der Ludwig-Maximilians-Universität
München

vorgelegt von
Jakob Näger
aus Nürnberg

München, 01. März 2019

Erstgutachter: Prof. Immanuel Bloch

Zweitgutachter: Prof. Frank Pollmann

Weitere Prüfungskommissionsmitglieder: Prof. Matthias Punk, Prof. Jan Lipfert

Tag der mündlichen Prüfung: 08. April 2019

Zusammenfassung

Periodisch getriebene Quantengittersysteme sind interessante Untersuchungsobjekte, um neue topologische Phasen zu realisieren. Ultra-kalte Atome eignen sich optimal für diese Floquet-Engineering Ansätze, da sich ihre Eigenschaften, wie Bandstrukturen und Wechselwirkungen, gut kontrollieren lassen. Während sowohl wechselwirkende Systeme als auch topologische Bandstrukturen schon erfolgreich demonstriert wurden, haben die hohen Heizraten, die mit periodischem Treiben aus einem effektiv unerschöpflichen Energiereservoir verbunden sind, bisher eine Kombination der beiden verhindert. Daher stellen Enthüllung, Verständnis und letzten Endes Kontrolle über die Mechanismen der Energieabsorption einen großen Schritt in Richtung topologischer, wechselwirkender Systeme dar. Diese Dissertation berichtet von der Entdeckung theoretisch vorhergesagter parametrischer Resonanzen in Bose-Einstein-Kondensaten in periodisch getriebenen optischen Gittern. Diese Resonanzen führen zu einem exponentiellen Anwachsen instabiler Impulsmoden in den ersten Zyklen des Treibens und stellen somit den Beginn der Zerstörung des Kondensats durch Heizen dar.

Wir beobachten die Entwicklung dieser Impulszustände, nutzen Time-of-Flight Messungen zur Identifikation der instabilsten Moden und erfassen die entsprechenden Wachstumsraten quantitativ. Die gewonnenen Ergebnisse werden mit Vorhersagen aus der Bogoliubov-Theorie verglichen.

Unsere Ergebnisse bestätigen außerdem die zentrale Rolle, die kontinuierliche Freiheitsgrade spielen, d.h. Dimensionen ohne Gitter, die das zuvor stabile Regime oberhalb der Bogoliubov-Bandbreite instabil machen.

Außerdem haben wir mit der harmonischen Falle, die das Kondensat hält, noch eine weitere Quelle störender Einflüsse gefunden. Sie erzeugt Zustände in der Bandlücke, die das System auch für Treibfrequenzen oberhalb der Bandbreite instabil machen. Da der Überlapp dieser Tamm-Zustände mit dem Kondensat für zunehmende Energie abnimmt, nimmt auch die Instabilität des Systems zu noch größeren Treibfrequenzen hin ab.

Abstract

Periodically driven quantum lattice systems are an interesting subject of investigation in view of reaching new topological phases of matter. Ultra-cold atoms are well suited for these Floquet-engineering approaches, as they offer great control over their properties, such as band structures and interactions. While both interacting systems and topological band structures have been successfully demonstrated, the high heating rates that are associated with periodically driving an interacting system from an effectively infinite energy reservoir, have so far prevented the combination of both features. One step towards the realization of topological interacting systems is thus to unveil, understand and finally control the mechanisms responsible for energy absorption. This thesis reports on the identification of theoretically predicted parametric resonances in a Bose-Einstein condensate in a periodically driven one-dimensional optical lattice. These resonances lead to an exponential growth of unstable momentum modes in the first few cycles of the periodic driving, marking the onset of the destruction of the condensate by heating.

We monitor the time evolution of these modes, identify the momentum of the most unstable modes in time of flight measurements and quantitatively capture the respective growth rates. We compare these findings to predictions from Bogoliubov theory.

Our findings also confirm the crucial role played by continuous degrees of freedom, i.e. dimensions without lattice, which render the previously stable regime above the Bogoliubov bandwidth unstable.

We also discovered an additional destructive feature in the harmonic confinement of the condensate, which produces states located in the band gap that keep the system unstable even for driving frequencies higher than the bandwidth. Because the overlap of these Tamm states with the condensate decreases with increasing energy, so does the instability of the system for even higher driving frequencies.

Contents

Zusammenfassung	v
Abstract	vii
1 Introduction	1
2 Theoretical Concepts	5
2.1 Ultra-cold Bose Gases	7
2.2 Band Theory	9
2.2.1 Bloch's Theorem	9
2.2.2 Sinusoidal Lattice	11
2.2.3 Wannier Functions	12
2.3 Gross-Pitaevskii Equation	14
2.4 Bogoliubov Approximation	16
2.4.1 Bogoliubov Hamiltonian	16
2.4.2 Bogoliubov Transformation	17
2.4.3 Bose-Hubbard Hamiltonian	18
2.5 Thomas-Fermi Approximation	20
2.5.1 Thomas-Fermi Approximation in the Trap	20
2.5.2 Thomas-Fermi Approximation in the 1D lattice	21
2.6 Floquet Theory	24
2.6.1 Floquet's Theorem	24
2.6.2 Transformation to the Floquet Frame	26
2.6.3 Properties	27
2.6.4 Transformation to the Rotating Frame	28
2.6.5 Renormalized Tunneling	29
2.6.6 Floquet Fermi's Golden Rule	30
2.7 Parametric Oscillator	33
2.7.1 Classical Parametric Oscillator	33
2.7.2 Mapping to Bogoliubov Hamiltonian	36
2.8 Bogoliubov-de Gennes Formalism	37
2.8.1 Bogoliubov-de Gennes Equations of Motion	37
2.8.2 Parametric Oscillator Mapping	38
2.8.3 Limitations of the Bogoliubov-de Gennes Description	42

3	Experimental Setup	43
3.1	Setup	45
3.2	Physical Principles	48
3.2.1	Magneto-Optical Trap	48
3.2.2	Optical Molasses	48
3.2.3	Magnetic Quadrupole Trap	49
3.2.4	Optical Dipole Trap	51
3.2.5	Feshbach Resonance	52
3.3	1D Lattice	53
3.3.1	Lattice Potential	53
3.3.2	Lattice Acceleration	55
3.3.3	Band-Mapping	56
3.4	Imaging	57
4	Measurements	59
4.1	Dynamical Instabilities	60
4.1.1	Experimental Sequence	61
4.1.2	Evaluation of the q_x -Component of the Most Unstable Mode	61
4.1.3	Evaluation of the q_y -Component of the Most Unstable Mode	65
4.2	Calibration	66
4.2.1	Magnification Factor	66
4.2.2	Dipole Trapping Frequencies	67
4.2.3	Atom Number	67
4.2.4	Trapping Frequencies in the Presence of the Lattice	68
4.2.5	Brillouin Zone Width	68
5	Results	69
5.1	q_x -Component of the Most Unstable Mode	70
5.2	q_y -Component of the Most Unstable Mode	72
5.3	Instability Rate	73
5.4	Benchmarking the Bogoliubov-de Gennes Model	74
5.5	Effect of Harmonic Confinement	75
5.6	Interaction Parameter g	78
5.6.1	Definition of g	78
5.6.2	\bar{g} vs. g_{\max}	79
5.6.3	Difference 2D - 3D	79
6	Conclusion and Outlook	81
7	Appendix	85

A	Band Structure	87
A.1	Proof of Bloch's Theorem	87
A.2	Orthonormal Bloch Functions	88
A.3	Equation for Bloch Functions	89
A.4	Orthogonal Wannier Functions	90
B	Energy of the BEC in Hamiltonian 2.27	91
C	Bogoliubov Approximation	95
C.1	Transformation to Momentum Space	95
C.2	Extraction of the zero-Momentum Mode	97
C.3	Bogoliubov Transformation	98
C.4	Bose-Hubbard Hamiltonian	101
D	Thomas-Fermi Approximation in the Lattice	103
E	Floquet Theory	109
E.1	Fourier Coefficients $\Phi^{(m)}$ of $\Phi(t)$	109
E.2	Effective Hamiltonian $\hat{H}_{F'}$	110
E.3	Time-Evolution Operator $\hat{U}(t_2, t_1)$	110
E.4	Transformation to the Rotating Frame	112
E.5	Commutators $[\hat{a}, e^{x\hat{n}}]$ and $[\hat{a}^\dagger, e^{x\hat{n}}]$	114
F	Parametric Oscillator	117
F.1	Mapping to Hill Differential Equation	117
F.2	Classical Parametric Oscillator	118
F.3	Mapping to Bogoliubov Hamiltonian	121
G	Bogoliubov-de Gennes Equations of Motion	123
H	Weak Coupling Conserving Approximation	125
I	Truncated Wigner Approximation	127
	References	129
	Danksagung	149

Introduction

Based on works of Satyendra Nath Bose on the quantum statistics of photons [1] in 1924, Albert Einstein made the prediction that an ideal gas of Bosons will condense into the ground state at low temperatures [2] in 1925. While reaching the necessary low temperatures seemed impossible for decades, the invention of the laser by Theodore Maiman [3] in 1960, based on stimulated emission, another prediction from Albert Einstein [4], brought a new, powerful tool into the game. It led to the idea that atoms moving with thermal velocities could be slowed down by nearly resonant light [5]. This was first achieved with ions [6], as they are more easily confined than neutral atoms. With the invention of the magneto-optical trap (MOT) [7] it was finally possible, to not only cool down atoms to temperatures below 1mK, but also to hold them for seconds or even minutes. With even further increase of phase-space density by evaporative cooling in magnetic and optical dipole potentials, the first Bose-Einstein condensates (BEC) of alkali atoms were finally observed in 1995 [8–13]. Since then, Fermions have also been cooled to quantum degeneracy [14, 15], molecules have been cooled down to their ground state [16–18], and even Bose-Fermi mixtures have been investigated [19]. Excitations of degenerate gases have been studied, e.g. vortices [20, 21] and phonons [22, 23]. Feshbach resonances made it possible to tune interactions in cold gases [24, 25], so e.g. a Tonks-Girardeau gas could be realized [26, 27]. Improvements in imaging systems allowed for observation [28–34] and manipulation [35] of individual atoms.

Numerous direct applications for cold atoms have also been found since. They include the measurement of very low pressures via the loss rate of cold atoms trapped in a MOT [36]. Atomic interferometry [37–40] is used in atomic clocks, e.g. strontium lattice clock which have recently reached a stability of $5 \cdot 10^{-19}$ with averaging over 1 hour [41] which corresponds to detecting a difference of ≈ 5 mm in the gravitational potential of the earth. Gravimeters in turn have reached a sensitivity of $39 \frac{\text{mm}}{\text{s}^2}$ [42, 43] and are used to e.g. map the geoid [44] or locate mineral deposits [45]. Technological advances in the field made it possible to cheaply work with cold atoms in atom-on-a-chip applications, e.g. a MOT etched in silicon [46].

A very interesting application from a fundamental point of view is the realization of Richard Feynman’s proposal of using a well controllable quantum system to simulate another quantum system of interest [47]. For example, there are proposals to simulate quantum lattice gauge theories with ultra-cold atoms [48, 49]. A big step in that direction has been made with the advent of optical lattices [50] in multiple geometries, including square [51], honeycomb [52, 53], checkerboard [54], triangular [55] and Kagome [56]. They were used to realize the Hubbard model [15, 51, 57, 58], study magnetic frustration [59], or produce synthetic magnetic fields [60, 61]. In disorder potentials [62–64] Anderson [63, 65, 66] and many-body localization [67–70] have been shown and thoroughly investigated.

High efforts and hopes are also put in the investigation of topological band structures [71, 72]. While topology has been studied in mathematics for a long time [73, 74], it is a relatively young field in physics that historically is tightly connected to the discovery of the quantum Hall effect in 1980 [75], which led to the discovery of new topologi-

cal phases of matter [76–79]. Due to its topological protection, the quantum Hall effect proved very robust against shape and distortions in the material [80] and is now used as a practical standard of resistance [81]. The concept of geometric phases [82–85] is very important to topology. After the quantum Hall effect had been discovered, geometric phases have been observed in photons [86, 87] and nuclear spins [88–90]. With cold atoms, a direct observation of topological band-structures was possible [91–93]. To what extent topology survives in the presence of strong interactions [94] is still under investigation, as are fractional quantum Hall states [95–97].

Topological band structures can be characterized e.g. by transport dynamics [98, 99], quenching the band structure [92, 100], or by observation of edge states [101–103].

The area of Floquet-engineering is concerned with the creation of tailored band-structures, especially topological ones [96, 104–107]. Circular shaking has been used to create topologically non-trivial band structures and realize the Haldane model [108–110]. Numerous works have been published on the creation of artificial gauge fields by periodic driving [111–116], e.g. artificial magnetic fields [104, 107, 117]. A big goal is the realization of a Floquet topological insulator [118–120]. Recently, these techniques have been applied in order to develop protocols for engineering Z_2 lattice gauge theories [121].

The effects of periodic driving have been studied for a long time [122]. In lattice systems, periodic driving has been shown to hybridize bands in the resonant case [123] or affect the tunneling rate [124, 125] due to a suppression of Bloch bands [126–129]. This effect of dynamical localization [130, 131] survives even in the presence of interactions [132, 133]. It was possible to use this effect to observe a dynamical transition from a super-fluid to a Mott insulating phase [134].

A great problem that arises in periodically-driven systems is their trend to infinite temperatures [135, 136]. This is due to the provision of an effectively infinite energy reservoir by the external drive and imposes a fundamental limit on the timescales experiments in driven ultra-cold atoms can be performed on. Many groups have worked towards understanding the fundamental mechanisms behind heating in driving systems [137–141]. This even lead to the idea of characterizing a system’s topology via its heating rates [142, 143].

This thesis reports on the identification of parametric resonances in a BEC in a periodically-driven one-dimensional optical lattice. These resonances lead to dynamical instabilities that grow exponentially in the first few cycles of the driving and lead to measurable population of momentum modes outside the BEC. We observe the growth of the respective modes stroboscopically over many cycles and identify a regime in which the linear Bogoliubov description of the instability is valid. In this regime, we determine the most unstable mode and compare its momentum components to theoretical predictions, as we do for its growth rate. This reveals the detrimental effect of continuous degrees of freedom perpendicular to the lattice. In the context of this work, we also identify the harmonic confinement of the BEC as another source of instability.

The results of this work have been published in:

- J. Näger, K. Wintersperger, M. Bukov, S. Lellouch, E. Demler, U. Schneider, I. Bloch, N. Goldman, and M. Aidelsburger. *Parametric instabilities of interacting bosons in periodically-driven 1D optical lattices*. [arXiv \(2018\)](#)

Another group has also found signatures of these parametric resonances with a different approach [144].

Apart from this work, I also contributed to a publication on heating rates in a shaken one-dimensional optical lattice, however these findings are not part of this thesis and have been presented in the PhD thesis of Martin Reitter [145]:

- M. Reitter, J. Näger, K. Wintersperger, C. Sträter, I. Bloch, A. Eckardt, and U. Schneider. *Interaction Dependent Heating and Atom Loss in a Periodically-Driven Optical Lattice*. [Physical Review Letters 119 \(2017\)](#)

Theoretical Concepts

This part shall give an overview of the most important theoretical concepts behind the experiments performed in this thesis. During the execution of this project, many problems and misunderstandings arose from the usage of different conventions by different parties of the team. To avoid or at least reduce problems like this in the future, this part shows a very detailed, consistent version of all relevant theoretical frameworks, down to relevant derivations in the appendix.

We will start with a short chapter about the thermodynamics in an ultra-cold Bose gas in chapter 2.1 as a general background, explaining how many particles macroscopically occupy the same state at low temperatures, forming a Bose-Einstein condensate (BEC). Then we move on to lattice physics and the associated band structures as well as the connected basis states based on Bloch and Wannier functions in chapter 2.2. Afterwards, in chapter 2.3 we introduce the non-linear Gross-Pitaevskii equation (GPE) by including contact interactions in the Hamiltonian of the previously non-interacting Bose gas. chapter 2.4 contains an explanation of how collective excitations on top of the BEC can be described with the help of the Bogoliubov transformation. The first part of this transformation will also help us arrive at the Bose-Hubbard Hamiltonian, which we use in the theoretical description of our experiment. In the Thomas-Fermi approximation in chapter 2.5, we will neglect the kinetic term in the GPE, arriving at an explicit formula for the radii of a harmonically trapped BEC in a 1D lattice. In chapter 2.6 we introduce the concepts of Floquet physics describing the dynamics of periodically-driven systems. There, we will also shortly visit the Floquet Fermi's golden rule approach to estimating heating rates of the driven BEC on long timescales, a concept described in detail in the PhD thesis of Martin Reitter [145] and the corresponding publication [146]. From there, we move on to the parametric oscillator in chapter 2.7, a model connected to the interpretation of the observations in our experiments. Finally, the Bogoliubov-de Gennes (BdG) formalism will be introduced in chapter 2.8, where we derive the BdG equations of motion for the BEC's excitations.

2.1 Ultra-cold Bose Gases

All experiments were performed on ultra-cold Bosons. In an ideal, non-interacting gas of Bosons in a thermal state of temperature T , the average number of atoms in any given state is [147, 148]:

$$f_i^0 = \frac{1}{e^{(\varepsilon_i - \mu)/(k_B T)} - 1}, \quad (2.1)$$

with the energy ε_i of state i , the Boltzmann constant k_B and the chemical potential μ , which is fixed by the total particle number $N = \sum_i f_i^0$. This means that with lower temperatures, the occupation of the ground state n_0 rises and gets macroscopically occupied. This happens when the fugacity $\zeta = e^{\mu/(k_B T)}$ becomes of order unity (for $\zeta = 1$ the occupation of the ground state diverges). The collective of particles in the ground state is then called a "Bose-Einstein condensate" (BEC) and constitutes the initial state for us to start our experiments from. In the high-temperature limit $k_B T \gg \Delta\varepsilon$ ($\Delta\varepsilon$ denotes the level spacing) the particle number sum $N = \sum_i f_i^0$ can be approximated by an integral $N \approx \int_0^\infty d\varepsilon g(\varepsilon) f^0(\varepsilon)$, with $g(\varepsilon)$ the density of states, which fails for low temperatures due to the large occupation of the ground state. However, a valid description is recovered, if the number of particles in the ground state N_0 is carried along separately in addition to the integral [147]. This way, the number of thermal atoms $N_{\text{th}} := N - N_0$ can be written as:

$$N_{\text{th}} = \int_0^\infty d\varepsilon g(\varepsilon) f^0(\varepsilon). \quad (2.2)$$

In a harmonic oscillator with quadratic potential $V(x, y, z) = \frac{1}{2} m (\omega_x^2 x^2 + \omega_y^2 y^2 + \omega_z^2 z^2)$, the density of states can be evaluated to $g(\varepsilon) = \frac{\varepsilon^2}{2\hbar^3 \omega_x \omega_y \omega_z}$ in a straight forward manner [147]. The critical temperature T_c at which Bose-Einstein condensation occurs, is reached when the number of thermal atoms N_{th} can only account for all atoms N if the chemical potential vanishes ($\mu = 0$). Below that temperature, the ground state becomes macroscopically occupied $N_0 > 0$ to compensate for the missing atoms:

$$N \stackrel{!}{=} N_{\text{th}}(T_c) = \int_0^\infty d\varepsilon \frac{\varepsilon^2}{2\hbar^3 \omega_x \omega_y \omega_z} \frac{1}{e^{\varepsilon/(k_B T_c)} - 1}, \quad (2.3)$$

which evaluates to:

$$N = \frac{\zeta(3) (k_B T_c)^3}{\hbar^3 \omega_x \omega_y \omega_z} \quad (2.4)$$

$$\Rightarrow T_c = \frac{\hbar}{k_B} \left(\frac{\omega_x \omega_y \omega_z N}{\zeta(3)} \right)^{\frac{1}{3}}, \quad (2.5)$$

with $\zeta(\cdot)$ the Riemann zeta function. This puts the critical temperature in our experiment (see part 3) to $T_c \approx 100 \text{ nK}$. The number of atoms in the excited thermal states at any temperature $T < T_c$ can be calculated by inserting T in eq. 2.4 :

$$N_{\text{th}} = \frac{\zeta(3) (k_B T)^3}{\hbar^3 \omega_x \omega_y \omega_z} \quad (2.6)$$

$$N_0 = N - N_{\text{th}} \quad (2.7)$$

$$\frac{N_0}{N} = 1 - \frac{N_{\text{th}}}{N} \quad (2.8)$$

$$N_0 = N \left(1 - \left(\frac{T}{T_c} \right)^3 \right). \quad (2.9)$$

In any experimental setup, the gas has to be confined by some means, else it will expand due to its finite temperature (in our experiment, the expansion velocity is on the order $\mu\text{m/ms}$) and fall due to gravity. While the latter can be circumvented by so called "Zero-G" experiments in outer space or drop tubes [149, 150], the former always calls for a confining potential if some steady state is to be achieved. Making use of the AC-Stark effect [151], such potentials can be obtained optically by using beams of light, whose frequency is red detuned with respect to a transition of two internal states of the used atomic species (see section 3.2.4). Such potentials can be almost arbitrary in shape, e.g. box-like, if created by a digital micro-mirror device [152] or spacial light modulator [153]. In our experiment however, we use the much simpler harmonic confinement created at the center of overlapping Gaussian beams (which from now on will be referred to as optical dipole trap, see section 3.2.4).

2.2 Band Theory

Our experiment is conducted in a 1D optical lattice. The lattice has a big impact on the dispersion relation of the captured atoms: The free space parabola is deformed into a set of bands. In this chapter, we will show how Bloch's theorem can be used to theoretically understand what the energy eigenstates of the lattice Hamiltonian look like. Then we will solve for the band structure in the special case of a sinusoidal lattice. Finally, we will show how Wannier functions can be used as a different basis to help describe the Hamiltonian in terms of states that are maximally localized at one lattice site. They will later be used in the derivation of a Bose-Hubbard model of the experiment.

2.2.1 Bloch's Theorem

Bloch's theorem deals with Hamiltonians that are periodic in real space [154–156]:

$$\hat{H}(x) = \frac{\hat{p}^2}{2m} + V(x) \quad (2.10)$$

$$V(x) \stackrel{!}{=} V(x+d) \quad (2.11)$$

$$\Rightarrow V(x) = \sum_j V_j e^{i(jG)x} \quad (2.12)$$

$$d = \frac{2\pi}{G} \quad (2.13)$$

$$\Rightarrow \hat{H}(x) = \hat{H}(x+d), \quad (2.14)$$

with the periodic potential $V(x)$, period d and reciprocal lattice constant G . The periodicity defined by eq. 2.11 implies the possibility to expand the potential in a Fourier series (eq. 2.12). It is important to note that because the potential breaks continuous translational invariance, momentum conservation, which is connected to translational invariance by Noether's theorem [157], is lost. Instead, a quantity called quasi-momentum q , that is only conserved up to multiples of $\hbar G$, is connected to discrete translational invariance. Bloch's theorem states that the eigenstates of this Hamiltonian will have the form:

$$\psi_k(x) := u_k(x) e^{ikx} \quad (2.15)$$

$$u_k(x) \stackrel{!}{=} u_k(x+d), \quad (2.16)$$

which means: The eigenfunctions of a Hamiltonian with a potential periodic in space have the form of a plane wave multiplied by a function that has the same periodicity as the Hamiltonian. A simple proof of Bloch's theorem can be found in appendix A.1. We will call $\psi_k(x)$ the Bloch function and $u_k(x)$ the Bloch mode.

It follows from Bloch's theorem, that states with Bloch functions $\psi_k(x)$, with wave numbers k that differ by multiples of G , are equal (see section A.1), so we can restrict

wave numbers to the range $k \in [-\frac{\pi}{d}, \frac{\pi}{d}]$, with $k = -\frac{\pi}{d}$ and $k = \frac{\pi}{d}$ describing the same state. This range is called the Brillouin zone (BZ). A more intuitive approach is to think about the wave function as being sampled at the lattice sites [154]. In this case, the Nyquist–Shannon sampling theorem limits the bandwidth of wave numbers $|k| < \frac{2\pi}{2d}$ [158]. The formation of the band structure in a periodic potential is depicted in figure 2.1.

Bloch functions form an orthonormal basis of the Hilbert space, see appendix A.2.

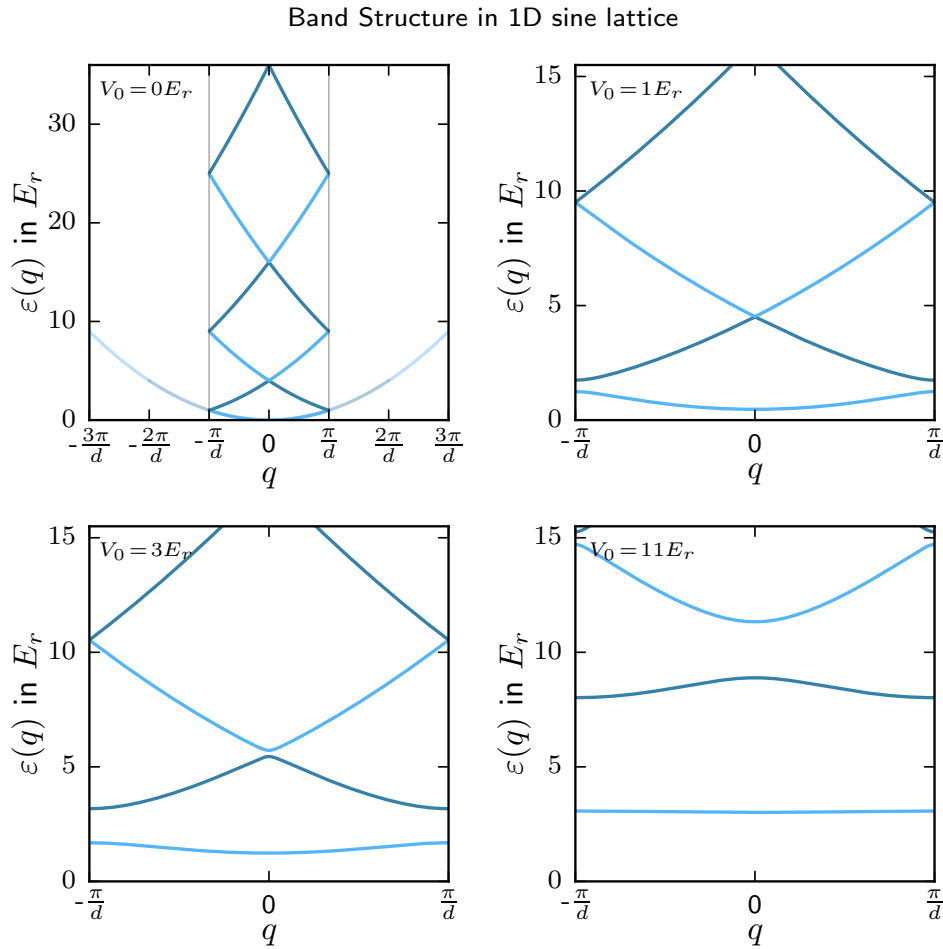


Figure 2.1: Band structure. The dispersion relation of a 1D sinusoidal lattice is shown for different lattice depths. The **top right** panel shows the limit of no lattice for reference: A free space dispersion folded in on the Brillouin zone (BZ). The gray lines indicate the BZ borders and the original free space dispersion is plotted in light colors.

The **other** panels display the dispersion relation for lattice depths of $V_0 = 1E_r$, $3E_r$ and $11E_r$, where E_r is the recoil energy as defined in chapter 3.3 and $11E_r$ corresponds to the lattice depth used for the experiments described in part 4.

2.2.2 Sinusoidal Lattice

In the experimental setup used in this work, the atoms are confined within an optical lattice that imposes a sinusoidal potential via the AC-Stark shift (see part 3), so the effective single-particle Hamiltonian differs from a free-space one in a manner that can be handled using Bloch's theorem.

$$\hat{H} = \frac{\hat{p}^2}{2m} + V(x) \quad (2.17)$$

$$V(x) = V_0 \frac{(1 + \cos(Gx))}{2} \quad (2.18)$$

$$= \frac{V_0}{2} + \frac{V_0}{4} e^{iGx} + \frac{V_0}{4} e^{-iGx} \quad (2.19)$$

The eigenfunctions $\psi(x)$ of this Hamiltonian can be easily found by equating the coefficients of the Fourier series of $\psi(x)$ and $\hat{H}\psi(x)$. We end up with an equation of the form (see appendix A.3) [154]:

$$\psi(x) = \sum_k c_k e^{ikx}, \quad (2.20)$$

$$\begin{pmatrix} \ddots & \vdots & \vdots & \vdots & \vdots & \vdots & \ddots \\ \dots & \frac{V_0}{2} + \frac{\hbar^2(k-2G)^2}{2m} - \varepsilon & \frac{V_0}{4} & 0 & 0 & 0 & \dots \\ \dots & \frac{V_0}{4} & \frac{V_0}{2} + \frac{\hbar^2(k-G)^2}{2m} - \varepsilon & \frac{V_0}{4} & 0 & 0 & \dots \\ \dots & 0 & \frac{V_0}{4} & \frac{V_0}{2} + \frac{\hbar^2 k^2}{2m} - \varepsilon & \frac{V_0}{4} & 0 & \dots \\ \dots & 0 & 0 & \frac{V_0}{4} & \frac{V_0}{2} + \frac{\hbar^2(k+G)^2}{2m} - \varepsilon & \frac{V_0}{4} & \dots \\ \dots & 0 & 0 & 0 & \frac{V_0}{4} & \frac{V_0}{2} + \frac{\hbar^2(k+2G)^2}{2m} - \varepsilon & \dots \\ \ddots & \vdots & \vdots & \vdots & \vdots & \vdots & \ddots \end{pmatrix} \begin{pmatrix} \vdots \\ c_{k-2G} \\ \dots \\ c_{k-G} \\ \dots \\ c_k \\ \dots \\ c_{k+G} \\ \dots \\ c_{k+2G} \\ \vdots \end{pmatrix} = \mathbf{0}. \quad (2.21)$$

Eq. 2.21 can be solved numerically using standard techniques for sparse matrices. This involves for example solving only a finite block (like the one depicted in eq. 2.21). Obviously, the amount of solutions (i.e. bands) will be equal to the size of the used matrix, so the higher number of the bands of interest, the larger the matrix has to be. At this point, we introduce the quasi-momentum $\mathbf{q} = \hbar k$ (in vector notation to allow for higher dimensions), as announced before, and denote the resulting dispersion relation by ε_q^n , where n denotes the band number.

We can see another intuitive argument for the restriction of \mathbf{q} the Brillouin zone here: Because the matrix is infinite, shifting the quasi-momentum \mathbf{q} by multiples of the lattice constant $\hbar G = \frac{\hbar}{a}$ will not affect the band structure or states. So quasi-momenta are only defined modulo $\hbar G$ and we can restrict wave numbers to the range $[-\frac{\pi}{a}, \frac{\pi}{a}]$, with $k = -\frac{\pi}{a}$ and $k = \frac{\pi}{a}$ describing the same state. The form of a few selected Bloch functions is depicted in figure 2.2.

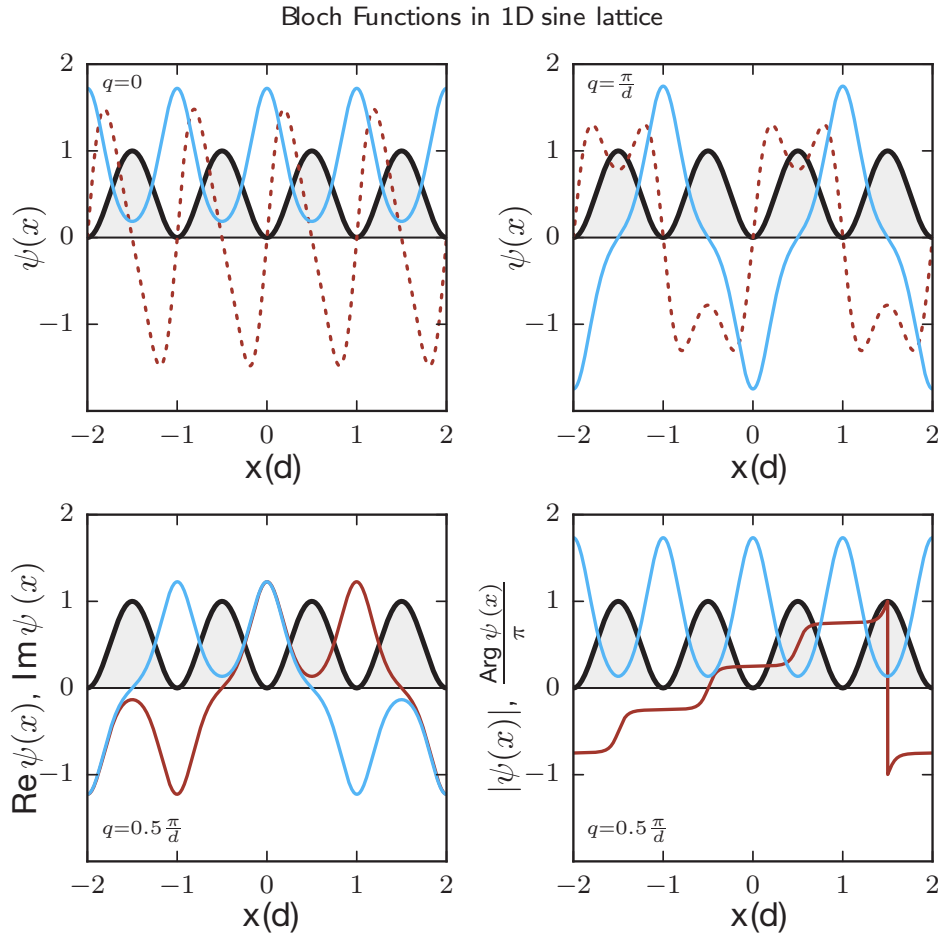


Figure 2.2: Bloch functions. The **top** panels show Bloch functions in a $V_0 = 11E_r$ 1D lattice of the lowest (**solid blue**) and first excited band (**dotted red**) for quasi-momentum $q = 0$ (**left**) and $q = \frac{\pi}{d}$ (**right**). They can be defined to be real in these cases.

The **bottom** panels show the case of $q = 0.5 \frac{\pi}{d}$ in the lowest band (also $V_0 = 11E_r$), where the complex phase is position dependent. The **left** panel shows real and imaginary part, the **right** panel displays absolute value and phase (modulo π). The lattice is sketched in the background for reference. The ordinate is somewhat arbitrary, as Bloch functions are not \mathcal{L}^2 -integrable.

2.2.3 Wannier Functions

If dealing with particles that are not in one defined momentum state and thus maximally delocalized over the whole lattice, Bloch functions are not the best choice of basis to describe them. A more suitable description can be made with the help of Wannier functions [159, 160]. These functions are defined in such a way that they are maximally localized at one lattice site (sacrificing a well defined associated energy, i.e. they are not an eigenstate of the Hamiltonian) [161]. The Wannier function $w_n(x)$ of the n -th band is an integral over all Bloch modes in that band within the BZ. For the Wannier function to be maximally localized at $x = 0$, the phases of the Bloch functions have to be chosen so

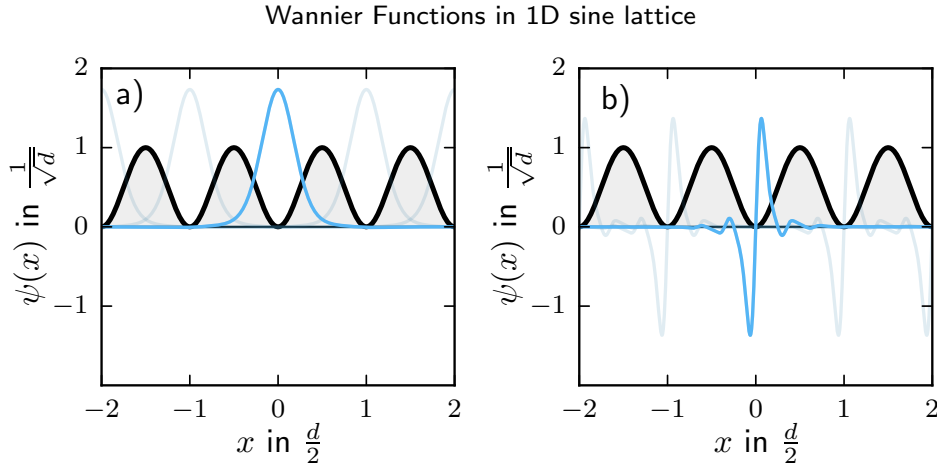


Figure 2.3: Wannier functions. The Wannier functions of the **a)** lowest and **b)** first excited band are shown. The transparent lines indicate neighboring Wannier functions.

they are all equal at that point. This ensures both that their sum has its maximum at $x=0$ and that they never interfere constructively at any other lattice site, as they don't have a common period.

$$w_n(x) = \frac{1}{\sqrt{\mathcal{N}_w}} \int_{k \in \text{BZ}} dk \psi_{n,k}(x), \quad (2.22)$$

again with a factor $\frac{1}{\sqrt{\mathcal{N}_w}}$ ensuring normalization. This Wannier function can be generalized to an orthonormal set of Wannier functions, localized at each one lattice site j :

$$w_{n,j}(x) = \frac{1}{\sqrt{\mathcal{N}_w}} \int_{k \in \text{BZ}} dk \psi_{n,k}(x-jd) \quad (2.23)$$

$$= \frac{1}{\sqrt{\mathcal{N}_w}} \int_{k \in \text{BZ}} dk u_{n,k}(x-jd) e^{ik(x-jd)} \quad (2.24)$$

$$= \frac{1}{\sqrt{\mathcal{N}_w}} \int_{k \in \text{BZ}} dk e^{-ikjd} u_{n,k}(x) e^{ikx} \quad (2.25)$$

$$= \frac{1}{\sqrt{\mathcal{N}_w}} \int_{k \in \text{BZ}} dk e^{-ikjd} \psi_{n,k}(x), \quad (2.26)$$

where in eq. 2.24 we used the periodicity of the Bloch modes $u_{n,k}(x)$. Wannier functions of different sites are orthogonal, see section A.4. Figure 2.3 shows the Wannier functions of the two lowest bands.

2.3 Gross-Pitaevskii Equation

Because the temperatures and densities in the BEC are very low, the collision energies involved are low enough so all interactions in the cloud are due to s-wave scattering [147]. This means that interactions can be described by only one parameter, the interaction parameter $U_0 = \frac{4\pi\hbar^2 a_s}{m}$ arising from s-wave scattering theory [147], with \hbar the reduced Planck's constant, a_s the scattering length and m the mass of the atomic species. So, a theory describing interactions in the cloud can easily be constructed by starting with the Hamiltonian of a non-interacting Bose gas and adding a term for contact interactions [147, 148]:

$$\hat{H} = \sum_{i=1}^{N_0} \left(\frac{\hat{\mathbf{p}}_i^2}{2m} + V(\mathbf{r}_i) \right) + U_0 \sum_{\langle i,j \rangle} \delta(\mathbf{r}_i - \mathbf{r}_j), \quad (2.27)$$

where $\hat{\mathbf{p}} = -i\hbar \partial_{\mathbf{r}}$ is the momentum operator and $\langle i, j \rangle$ indicates the sum running over all possible pairs of particles. It should be noted that this ansatz will cease to be valid if the particle density ρ becomes so big that three-body collisions start playing a role, which should happen around $\rho \approx \frac{1}{a_s^3}$.

The BEC will minimize the Hamiltonian, so we can simply write down the energy E of the N_0 -particle wave function and then minimize E .

All N_0 atoms in the condensate occupy the same single-particle state $\Phi(\mathbf{r})$, which is normalized, so

$$\int d\mathbf{r} |\Phi(\mathbf{r})|^2 \stackrel{!}{=} 1. \quad (2.28)$$

The N_0 -particle wave function can be written as:

$$\Psi(\mathbf{r}_1, \mathbf{r}_2, \dots, \mathbf{r}_{N_0}) = \prod_{i=1}^{N_0} \Phi(\mathbf{r}_i). \quad (2.29)$$

$$E = \langle \Psi | \hat{H} | \Psi \rangle \quad (2.30)$$

$$= \int \prod_{k=1}^{N_0} d\mathbf{r}_k \Psi(\mathbf{r}_1, \mathbf{r}_2, \dots, \mathbf{r}_{N_0}) \hat{H} \Psi(\mathbf{r}_1, \mathbf{r}_2, \dots, \mathbf{r}_{N_0}) \quad (2.31)$$

Eq. 2.31 can be evaluated to eq. 2.32, see appendix B:

$$E = \int d\mathbf{r} \sqrt{N_0} \Phi^*(\mathbf{r}) \left(\frac{\hat{\mathbf{p}}^2}{2m} + V(\mathbf{r}) + \frac{U_0}{2} N_0 \Phi^*(\mathbf{r}) \Phi(\mathbf{r}) \right) \sqrt{N_0} \Phi(\mathbf{r}) \quad (2.32)$$

We can now introduce the wave function of the condensate $\psi(\mathbf{r}) := \sqrt{N_0} \Phi(\mathbf{r})$, which will give us:

$$E = \int d\mathbf{r} \psi^*(\mathbf{r}) \left(\frac{\hat{\mathbf{p}}^2}{2m} + V(\mathbf{r}) + \frac{U_0}{2} \psi^*(\mathbf{r}) \psi(\mathbf{r}) \right) \psi(\mathbf{r}), \quad (2.33)$$

The correct ground state wave function $\psi(\mathbf{r})$ will now be the one that minimizes E , while still satisfying atom number conservation, as described by eq. 2.34. It can be found by independent variation of $\psi(\mathbf{r})$ and its complex conjugate $\psi^*(\mathbf{r})$, which is equivalent to an independent variation of its real and imaginary part. To minimize eq. 2.33 under the condition eq. 2.34 we use the method of Lagrange multipliers [147]:

$$N_0 = \int d\mathbf{r} \psi^*(\mathbf{r}) \psi(\mathbf{r}) \quad (2.34)$$

$$\delta E - \mu \delta N_0 = 0, \quad (2.35)$$

where the chemical potential μ takes the role of the Lagrange multiplier. Varying eq. 2.35 with respect to $\psi^*(\mathbf{r})$ results in the semi-classical time-independent Gross-Pitaevskii equation of the condensate:

$$\left(\frac{\hat{\mathbf{p}}^2}{2m} + V(\mathbf{r}) + U_0 |\psi(\mathbf{r})|^2 \right) \psi(\mathbf{r}) = \mu \psi(\mathbf{r}). \quad (2.36)$$

2.4 Bogoliubov Approximation

The Bogoliubov approximation can be used to obtain collective excitations of the atoms in the condensate to leading order in their creation/annihilation operators. This will be very helpful in the description of the instabilities of the driven condensate. We will bring the Gross-Pitaevskii equation (GPE, see chapter 2.3) in the form of a Hamiltonian and expand it with respect to the creation/annihilation operators of the $q = 0$ mode to get the Bogoliubov Hamiltonian. This Hamiltonian will then be transformed so its harmonic quasi-particle excitations, with a dispersion relation that depends on interactions, appear explicitly.

2.4.1 Bogoliubov Hamiltonian

If we recast the GPE (eq. 2.33) in the form of a Hamiltonian (i.e. applying second quantization), we get:

$$\hat{H} = \int_V d\mathbf{r} \hat{\psi}^\dagger(\mathbf{r}) \left(\frac{\hat{\mathbf{p}}^2}{2m} + V(\mathbf{r}) + \frac{U_0}{2} \hat{\psi}^\dagger(\mathbf{r}) \hat{\psi}(\mathbf{r}) \right) \hat{\psi}(\mathbf{r}) \quad (2.37)$$

$$\hat{H} = \int_V d\mathbf{r} \hat{\psi}^\dagger(\mathbf{r}) \frac{\hat{\mathbf{p}}^2}{2m} \hat{\psi}(\mathbf{r}) + V(\mathbf{r}) \hat{\psi}^\dagger(\mathbf{r}) \hat{\psi}(\mathbf{r}) + \frac{U_0}{2} \hat{\psi}^\dagger(\mathbf{r}) \hat{\psi}^\dagger(\mathbf{r}) \hat{\psi}(\mathbf{r}) \hat{\psi}(\mathbf{r}), \quad (2.38)$$

with $\hat{\psi}(\mathbf{r})$ the field operator of a particle in the condensate. Here, we explicitly include the volume V in the integral (which we can send to infinity, while keeping the density constant, in the end). This can now be transformed into momentum space (for detailed derivation see appendix C.1) with \hat{b}_p the annihilation operator in momentum space [147]:

$$\hat{b}_p = \frac{1}{\sqrt{V}} \int_V d\mathbf{r} e^{-i\frac{p\mathbf{r}}{\hbar}} \hat{\psi}(\mathbf{r}) \quad (2.39)$$

$$\hat{\psi}(\mathbf{r}) = \frac{1}{\sqrt{V}} \sum_p e^{i\frac{p\mathbf{r}}{\hbar}} \hat{b}_p \quad (2.40)$$

$$\hat{H} = \sum_p \varepsilon_p^0 \hat{b}_p^\dagger \hat{b}_p + \frac{U_0}{2V} \sum_{p,p',p''} \hat{b}_{p+p'}^\dagger \hat{b}_{p'-p''}^\dagger \hat{b}_{p'} \hat{b}_p, \quad (2.41)$$

where the sums run over all (equally spaced) allowed momentum modes and ε_p^0 is the single-particle dispersion that depends on the potential $V(\mathbf{r})$. Because we have a lattice potential, we will relabel the operators to indicate the transition from momentum p to quasi-momentum q :

$$\hat{H} = \sum_q \varepsilon_q^0 \hat{b}_q^\dagger \hat{b}_q + \frac{U_0}{2V} \sum_{q,q',q''} \hat{b}_{q+q''}^\dagger \hat{b}_{q'-q''}^\dagger \hat{b}_{q'} \hat{b}_q \quad (2.42)$$

To perform the Bogoliubov approximation, we can now draw all operators of the zero-momentum mode \hat{b}_0 outside the sum, replace them with their expectation value $\hat{b}_0 \approx \sqrt{N_0}$

and restrict to terms up to second order in annihilation operators of other momentum modes $\mathcal{O}(\hat{b}_{q \neq 0}^2)$. Appendix C.2 illustrates how this leads us to a Hamiltonian that describes the excitations atop the condensate:

$$\hat{H} = -\frac{g N_0}{2} + \sum_{q>0} \left((\varepsilon_q^0 + g) (\hat{b}_q^\dagger \hat{b}_q + \hat{b}_{-q}^\dagger \hat{b}_{-q}) + g (\hat{b}_q^\dagger \hat{b}_{-q}^\dagger + \hat{b}_q \hat{b}_{-q}) \right), \quad (2.43)$$

with the interaction parameter $g := n_0 U_0$, which is equal to the chemical potential μ .

2.4.2 Bogoliubov Transformation

Appendix C.3 shows how a Hamiltonian \hat{H} of the form:

$$\hat{H} = \varepsilon_0 (\hat{a}^\dagger \hat{a} + \hat{b}^\dagger \hat{b}) + \varepsilon_1 (\hat{a}^\dagger \hat{b}^\dagger + \hat{a} \hat{b}), \quad (2.44)$$

with the bosonic annihilation operators \hat{a} and \hat{b} can be transformed so it becomes explicit that it features two kinds of harmonic excitations, described by $\hat{\alpha}$ and $\hat{\beta}$ respectively.

$$\hat{\alpha} = u \hat{a} + v \hat{b}^\dagger \quad (2.45)$$

$$\hat{\beta} = u \hat{b} + v \hat{a}^\dagger \quad (2.46)$$

$$\Rightarrow \hat{H} = \varepsilon (\hat{\alpha}^\dagger \hat{\alpha} + \hat{\beta}^\dagger \hat{\beta}) + \varepsilon - \varepsilon_0 \quad (2.47)$$

$$\varepsilon := \sqrt{\varepsilon_0^2 - \varepsilon_1^2} \quad (2.48)$$

Applied to the Bogoliubov Hamiltonian 2.43, the transformation to be performed is:

$$\hat{b}_q = u_q \hat{\alpha}_q - v_q \hat{\alpha}_{-q}^\dagger \quad (2.49)$$

$$\hat{b}_{-q} = u_q \hat{\alpha}_{-q} - v_q \hat{\alpha}_q^\dagger \quad (2.50)$$

This results in:

$$\varepsilon_q = \sqrt{\varepsilon_q^0{}^2 + 2\varepsilon_q^0 n_0 U_0} \quad (2.51)$$

$$u_p^2 = \frac{1}{2} \left(\frac{\varepsilon_q^0 + n_0 U_0}{\varepsilon_q} + 1 \right) \quad (2.52)$$

$$v_p^2 = \frac{1}{2} \left(\frac{\varepsilon_q^0 + n_0 U_0}{\varepsilon_q} - 1 \right) \quad (2.53)$$

$$\hat{H} = -\frac{g N_0}{2} + \sum_{q>0} \left(\varepsilon_q (\hat{\alpha}_q^\dagger \hat{\alpha}_q + \hat{\alpha}_{-q}^\dagger \hat{\alpha}_{-q}) + \varepsilon_q - \varepsilon_q^0 - g \right) \quad (2.54)$$

To summarize, we now have a Hamiltonian (eq.2.55) that explicitly features harmonic quasi-particle excitations on top of the BEC with a dispersion relation according to eq.2.51:

$$\hat{H} = -\frac{g N_0}{2} + \sum_{q \neq 0} \left(\varepsilon_q \hat{a}_q^\dagger \hat{a}_q + \frac{1}{2} (\varepsilon_q - \varepsilon_q^0 - g) \right) \quad (2.55)$$

These excitations are observed as instabilities when driving a BEC in a one-dimensional optical lattice as observed in our experiment. The Bogoliubov dispersion ε_q is depicted in figure 2.4.

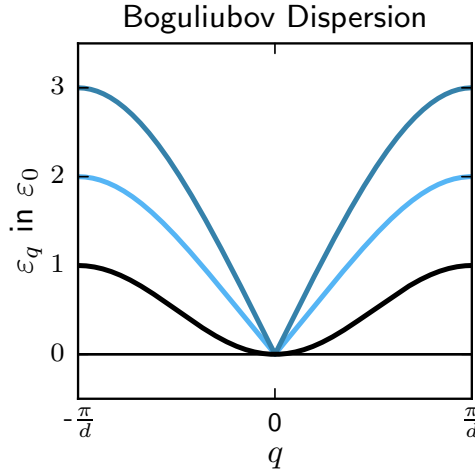


Figure 2.4: Bogoliubov Dispersion ε_q for a lattice dispersion (**black**) of cosine shape with a bandwidth of ε_0 . The dispersion of the excitations is shown for a value of $n_0 U_0 = g = 1.5 \varepsilon_0$ (**light blue**) and $g = 4 \varepsilon_0$ (**dark blue**).

2.4.3 Bose-Hubbard Hamiltonian

Our experiment is well described by a periodically-driven Bose-Hubbard model [162]. It can be derived from Hamiltonian 2.42 by a change of basis from momentum states q to Wannier states (see sec.2.2.3) located on site i with coordinates R_i according to:

$$\hat{H} = \sum_q \varepsilon_q \hat{b}_q^\dagger \hat{b}_q + \frac{U_0}{2V} \sum_{q, q', q''} \hat{b}_{q+q''}^\dagger \hat{b}_{q'-q''}^\dagger \hat{b}_{q'} \hat{b}_q$$

$$\hat{a}_i = \frac{1}{\sqrt{N_s}} \sum_q e^{i \frac{q}{\hbar} R_i} \hat{b}_q \quad (2.56)$$

$$\hat{b}_q = \frac{1}{\sqrt{N_s}} \sum_j e^{-i \frac{q}{\hbar} R_j} \hat{a}_j \quad (2.57)$$

Here N_s is the number of sites, which is equal to the number of momentum states.

If we insert eq. 2.57 in Hamiltonian 2.42, we arrive at (see appendix C.4):

$$\hat{H} = \sum_{j,l} \hat{a}_j^\dagger \hat{a}_l \frac{1}{N} \sum_q \varepsilon_q e^{i \frac{q}{\hbar} (R_j - R_l)} + \frac{U_0 N}{2V} \sum_j \hat{a}_j^\dagger \hat{a}_j^\dagger \hat{a}_j \hat{a}_j \quad (2.58)$$

The second term running only over one (site) index represents the interactions being contact-only, as designed. In the first term, physics is a bit richer. One can see that in the limit of a very deep lattice, when ε_q becomes effectively constant ($\varepsilon_q = \varepsilon$ independent of q), this kinetic term will contribute exactly ε per particle:

$$\sum_{j,l} \hat{a}_j^\dagger \hat{a}_l \frac{1}{N} \sum_q \varepsilon e^{i \frac{q}{\hbar} (R_j - R_l)} = \varepsilon \sum_{j,l} \hat{a}_j^\dagger \hat{a}_l \frac{1}{N} N \delta_{j,l} \quad (2.59)$$

$$= \varepsilon \sum_j \hat{a}_j^\dagger \hat{a}_j \quad (2.60)$$

$$= \varepsilon \sum_j \hat{n}_j \quad (2.61)$$

$$= \varepsilon N \quad (2.62)$$

If we start from this limit (of flat bands) and make ε_q increasingly dispersive, terms with differing positions R_j and R_l will start to play a role. Obviously, the more dispersive the band, the larger $R_j - R_l$ can be for the term to contribute. If we take just neighboring sites into account and neglect the on-site kinetic term (which doesn't give rise to any physics), we arrive at the Bose-Hubbard Hamiltonian [162, 163]:

$$\hat{H} = -J \sum_{\langle j,l \rangle} (\hat{a}_j^\dagger \hat{a}_l + \hat{a}_l^\dagger \hat{a}_j) + \frac{U}{2} \sum_j \hat{a}_j^\dagger \hat{a}_j^\dagger \hat{a}_j \hat{a}_j, \quad (2.63)$$

with the term $\langle j,l \rangle$ indicating the sum running over all pairs of neighboring sites, $J := -\frac{1}{N} \sum_q \varepsilon_q e^{i \frac{q}{\hbar} (R_j - R_l)}$ the tunnel element, for R_j a neighbor of R_l , and $U = \frac{U_0 N}{V}$.

We can now extend the the model to account for a a force applied to the particles. In the experiment (see part 4), we subject them to a periodic sinusoidal drive. A force constant in space implies a potential linear in space, i.e. $\propto \sum_j j \hat{n}_j$. To make that periodic in time, we introduce the term $K \cos(\omega t + \varphi) \sum_j j \hat{n}_j$ [164]:

$$\hat{H}(t) = -J \sum_{\langle j,l \rangle} (\hat{a}_j^\dagger \hat{a}_l + \hat{a}_l^\dagger \hat{a}_j) + K \cos(\omega t + \varphi) \sum_j j \hat{n}_j + \frac{U}{2} \sum_j \hat{n}_j (\hat{n}_j - 1), \quad (2.64)$$

with driving frequency ω , phase φ and amplitude K . In our experiment, we set $\varphi = 0$. Also, on the 1D lattice we can simplify $\langle j,l \rangle$:

$$\hat{H}(t) = -J \sum_j (\hat{a}_j^\dagger \hat{a}_{j+1} + \hat{a}_{j+1}^\dagger \hat{a}_j) + K \cos(\omega t) \sum_j j \hat{n}_j + \frac{U}{2} \sum_j \hat{n}_j (\hat{n}_j - 1). \quad (2.65)$$

2.5 Thomas-Fermi Approximation

If we take a closer look at the Gross-Pitaevskii equation, specifically its kinetic and interaction energy terms, we can easily see that as more particles are added, the interaction will dominate the kinetic part due to their scaling with the atom number N_0 : the kinetic energy scales $E_{\text{kin}} \propto N_0$, while the interaction energy scales $E_{\text{int}} \propto N_0^2$ [147]. We will now estimate their magnitude and check that this hierarchy is already fulfilled in the case of the harmonically trapped BEC in our experiment (see chapter 3.1). With the Thomas-Fermi approximation, we can explicitly formulate the dependence of the cloud radii R_i on atom number N_0 , which we use in the calibration of N_0 .

$$E_{\text{int}} \approx N_0 U_0 n = N_0 U_0 \frac{N_0}{R^3} = \frac{4\pi \hbar^2 a_s N_0^2}{m R^3}, \quad (2.66)$$

with $n = \frac{N_0}{R^3}$ the particle density as particle number per typical length scale, i.e. size, of the cloud R to the power of three and $U_0 = \frac{4\pi \hbar a_s}{m}$ the interaction parameter as obtained from s-wave scattering [147]. From the typical length scale of the cloud R , we can estimate the typical momentum $\frac{\hbar}{R}$ via Heisenberg's uncertainty principle and thus estimate the kinetic energy:

$$E_{\text{kin}} \approx N_0 \frac{1}{2m} \frac{\hbar^2}{R^2}. \quad (2.67)$$

With a typical scattering length used in the experiment of $a_s = 20a_0$, with the Bohr radius a_0 , and $R = 20\mu\text{m}$, which is the longest extent of the cloud (see chapter 3) the ratio of interaction and kinetic energy is:

$$\frac{E_{\text{int}}}{E_{\text{kin}}} \approx 8\pi \frac{a_s}{R} N_0 \approx \frac{N_0}{750}. \quad (2.68)$$

In the experiment we usually work with $N_0 \approx 10^5$ atoms, so $E_{\text{int}} \gg E_{\text{kin}}$, even in the compressed vertical direction, where the cloud is almost an order of magnitude smaller. This justifies neglecting the kinetic term in the Gross-Pitaevskii equation and we find the Thomas-Fermi approximation [147]:

$$(V(\mathbf{r}) + U_0 |\psi(\mathbf{r})|^2) \psi(\mathbf{r}) = \mu \psi(\mathbf{r}). \quad (2.69)$$

2.5.1 Thomas-Fermi Approximation in the Trap

It is trivial to solve eq. 2.69 for the density $n(\mathbf{r}) = |\psi(\mathbf{r})|^2$:

$$n(\mathbf{r}) = \begin{cases} \frac{\mu - V(\mathbf{r})}{U_0} & \text{where } V(\mathbf{r}) \leq \mu \\ 0 & \text{else,} \end{cases} \quad (2.70)$$

where the lower case is due to atom number conservation and the fact that $n(\mathbf{r})$ has to be non-negative. Figure 2.5 shows the resulting shape to the density distribution $n(\mathbf{r})$.

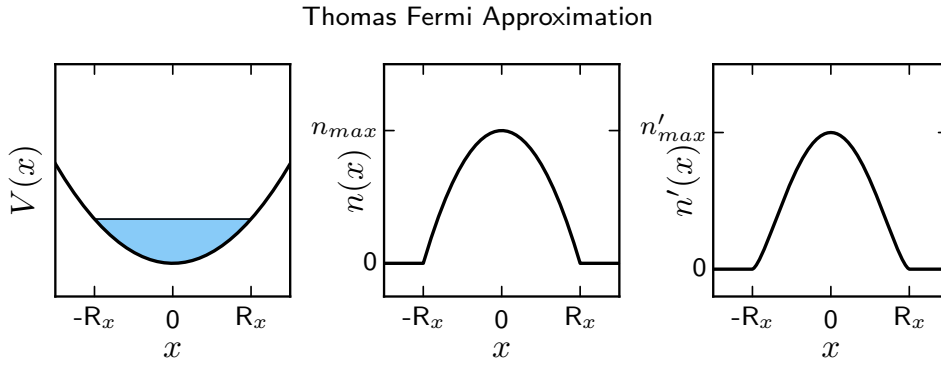


Figure 2.5: Left: Schematics of a condensate (blue) in a harmonic trap (black) as described by the Thomas-Fermi approximation.

Center: Thomas-Fermi density profile. R_x marks the Thomas-Fermi radius in the x -direction.

Right: Thomas-Fermi density profile integrated along one dimension as seen in imaging (see chapter 3.4).

For a BEC confined in an optical dipole trap that can be described by a potential of the form $V_{\text{trap}}(\mathbf{r}) = \frac{1}{2}m(\omega_x^2 x^2 + \omega_y^2 y^2 + \omega_z^2 z^2)$, with m the mass of the trapped atoms and ω_i the trapping frequency along direction i , the density takes the shape of a paraboloid, just like the potential. However, the density is high in the center and tends to zero at the border of the cloud, where a sharp edge is predicted. This means that the approximation is good in the center, but will fail in predicting the proper shape of the edges, where the interaction energy drops to zero and is dominated by the kinetic part. A failure of the approximation at the edges is obvious anyway from the fact that sharp edges are predicted.

We could now solve for the size of the cloud, the Thomas-Fermi radii, as a function of trapping frequencies, atom number and scattering length. However, as the case of a trapped cloud is contained in a description of a trapped cloud overlaid with a 1D lattice for vanishing lattice depth, we will not solve this easier case. All relevant formulas can be taken from sec. 2.5.2 for $\zeta = 1$. In the following section, the Thomas-Fermi approximation will be extended to include a periodic one-dimensional optical lattice.

2.5.2 Thomas-Fermi Approximation in the 1D lattice

If the trapped cloud is superimposed with a one-dimensional lattice along the x -direction, the BEC is cut in slices by the additional potential [146, 165]. These slices are usually referred to as "pancakes". In this case, the wave operators $\hat{\psi}(\mathbf{r})$ are expressed via the Wannier functions of the lowest band $w_0(x)$ along x and some \mathcal{L}^2 -integrable functions $\phi_{j,\perp}(\mathbf{r}_\perp)$ with j the site index and $\mathbf{r} = (x, \mathbf{r}_\perp)$ along y and z :

$$\hat{\psi}(\mathbf{r}) = \sum_j w_0(x-x_j) \phi_{j,\perp}(\mathbf{r}_\perp) \hat{a}_j, \quad (2.71)$$

where \hat{a}_j annihilates a particle on site j .

Now the interaction Hamiltonian takes the form:

$$\hat{H}_{\text{int}} = \sum_{i,j,k,l} \int d\mathbf{r} \frac{1}{2} U_0 w_0(x-x_i)^* w_0(x-x_j)^* w_0(x-x_k) w_0(x-x_l) \cdot \phi_{i,\perp}(\mathbf{r}_\perp)^* \phi_{j,\perp}(\mathbf{r}_\perp)^* \phi_{k,\perp}(\mathbf{r}_\perp) \phi_{l,\perp}(\mathbf{r}_\perp) \hat{a}_i^\dagger \hat{a}_j^\dagger \hat{a}_k \hat{a}_l. \quad (2.72)$$

Due to the localization of the Wannier functions at their respective sites, terms where $i=j=k=l$ is not fulfilled are suppressed by at least $\approx U/J$ with the (Bose-Hubbard) tunneling element J and the (Bose-Hubbard) on site interaction U . As we have no 3D lattice but pancakes, the on site interaction is quite small and we can neglect these terms. For the remaining terms, we define the Wannier integral of the lowest band $w_{0I} := \int dx |w_0(x)|^4$ that only depends on the lattice depth.

We are looking for the density distribution that describes the ground state of this Hamiltonian. However, this result would only be of limited help for us, as it will yield an array of 2D densities $n_{j,\perp}(\mathbf{r}_\perp)$, one for each lattice site j where the density modulation along the lattice direction would be described by Wannier functions. Because the optical resolution in the experiment is not high enough to observe this site-to-site modulation, it would be desirable to have instead a full 3D density $n(\mathbf{r})$ that resembles an envelope of the cloud without modulations. Appendix D details the way to consistently derive this 3D density. The result is a modified effective interaction characterized by the effective interaction parameter $U_0\zeta$, with $\zeta := w_{0I}d$ the zeta parameter which is the only thing reminiscent of the lattice in our energy term. We can now add the effective trap potential $V_{\text{trap}}(\mathbf{r})$:

$$V_{\text{trap}}(\mathbf{r}) = \frac{1}{2} m_K \left(\omega_x^2 x^2 + \omega_y^2 y^2 + \omega_z^2 z^2 \right), \quad (2.73)$$

to get the total potential energy of the particles in the trap E_{trap} . Note that the effective trap potential holds all confining and deconfining effects of lattice and dipole beams, but no lattice features:

$$E_{\text{pot}} := \langle \psi | \hat{H}_{\text{int}} + V(\mathbf{r}) | \psi \rangle \quad (2.74)$$

$$= \int d\mathbf{r} \left(\frac{1}{2} U_0 \zeta n^2(\mathbf{r}) + V(\mathbf{r}) n(\mathbf{r}) \right) \quad (2.75)$$

The proper density distribution $n(\mathbf{r})$ will minimize this energy while conserving atom number N_0 and satisfying non-negativity $n(\mathbf{r}) \geq 0 \forall \mathbf{r}$.

The method of Lagrange multipliers with the chemical potential μ as Lagrange multiplier yields (see appendix D):

$$\delta E_{\text{pot}} - \mu \delta N_0 \stackrel{!}{=} 0 \quad (2.76)$$

$$n(\mathbf{r}) = \begin{cases} \frac{\mu - V_{\text{trap}}(\mathbf{r})}{U_0 \zeta} & \text{where } V_{\text{trap}}(\mathbf{r}) \leq \mu \\ 0 & \text{else,} \end{cases} \quad (2.77)$$

with the chemical potential μ fixed by the total atom number N_0 :

$$N_0 = \int d\mathbf{r} n(\mathbf{r}) \quad (2.78)$$

We can now define the Thomas-Fermi radii R_i as the point on each axis where the density $n(\mathbf{r})$ goes to zero:

$$0 \stackrel{!}{=} n(r_i = R_i, r_{i \neq j} = 0) \quad (2.79)$$

$$\Rightarrow \mu = V_{\text{trap}}(r_i = R_i, r_{i \neq j} = 0) \quad (2.80)$$

This can be solved for μ and R_i as functions of atom number N_0 , trapping frequencies ω_i , scattering length a_s and lattice depth (implicitly contained in ζ), see appendix D:

$$\mu = \left(\frac{15 \hbar^2 a_s}{2 m_K} N_0 \zeta \omega_x \omega_y \omega_z \left(\frac{m_K}{2} \right)^{\frac{3}{2}} \right)^{\frac{2}{5}} \quad (2.81)$$

$$R_i = \left(\frac{15 \hbar^2}{m_K^2} \frac{\omega_x \omega_y \omega_z}{\omega_i^5} N_0 \zeta a_s \right)^{\frac{1}{5}} \quad (2.82)$$

The values for a system without lattice are reproduced for $\zeta = 1$.

It should be noted at this point, that we will end up with a profile that is not quite an envelope, but rather a scaled envelope. The reason for this is that the integral over the envelope does of course not yield the atom number, but is larger. However, the density we get with this value of the chemical potential μ is scaled so its integral yields exactly the number of atoms in the condensate.

2.6 Floquet Theory

Analogously to the case of Hamiltonians periodic in real space, Hamiltonians can be periodic in time, as in the present case of periodically-driven systems. Periodically-driven band structures like the one we are concerned with in this work are sometimes referred to as spacio-temporal crystals [166]. In this chapter, we outline how Floquet's theorem can be used to theoretically describe periodically-driven systems.

2.6.1 Floquet's Theorem

Floquet's theorem [156, 167, 168] concerns itself with ordinary differential equations and states the following: Each equation of the form of eq. 2.83, with the operator $\hat{A}(t)$ periodic in t , i.e. $\hat{A}(t) = \hat{A}(t+T)$, has solutions of the form eq. 2.84, with $|y(t)\rangle = |y(t+T)\rangle$ having the same periodicity T as $\hat{A}(t)$

$$\partial_t |x(t)\rangle = \hat{A}(t) |x(t)\rangle \quad (2.83)$$

$$\Rightarrow |x(t)\rangle = e^{-i\omega t} |y(t)\rangle. \quad (2.84)$$

This can be understood intuitively, if we think back to the proof of Bloch's theorem (which is one special case of Floquet's theorem) - if we think about the Fourier transform of the problem, it makes sense that the solution only has Fourier components that show up in the problem. Thus, if we consider a periodic Hamiltonian:

$$\hat{H}(t) \stackrel{!}{=} \hat{H}(t+T) \quad (2.85)$$

$$\Rightarrow \hat{H}(t) = \sum_{m=-\infty}^{\infty} e^{im\omega t} \hat{H}^{(m)} \quad (2.86)$$

$$\hat{H}^{(m)} := \frac{1}{T} \int_0^T dt e^{-im\omega t} \hat{H}(t), \quad (2.87)$$

with period $T = \frac{2\pi}{\omega}$, it has solutions called Floquet states of the form [169]:

$$\psi(t) = e^{-i\frac{\varepsilon}{\hbar} t} \Phi(t), \quad (2.88)$$

with periodic Floquet modes $\Phi(t) \stackrel{!}{=} \Phi(t+T)$. The Schrödinger equation can be rearranged to get the quasi-energy ε :

$$\hat{H}(t) \psi(t) = i\hbar \partial_t \psi(t) \quad (2.89)$$

$$\hat{H}(t) \left(e^{-i\frac{\varepsilon}{\hbar} t} \Phi(t) \right) = i\hbar \partial_t \left(e^{-i\frac{\varepsilon}{\hbar} t} \Phi(t) \right) \quad (2.90)$$

$$e^{-i\frac{\varepsilon}{\hbar} t} \hat{H}(t) \Phi(t) = \varepsilon e^{-i\frac{\varepsilon}{\hbar} t} \Phi(t) + e^{-i\frac{\varepsilon}{\hbar} t} i\hbar \partial_t \Phi(t) \quad (2.91)$$

$$\varepsilon \Phi(t) = \left(\hat{H}(t) - i\hbar \partial_t \right) \Phi(t) \quad (2.92)$$

$$\hat{Q}(t) := \hat{H}(t) - i\hbar \partial_t \quad (2.93)$$

with the quasi-energy operator $\hat{Q}(t)$ [169], also called Floquet Hamiltonian. The quasi-energy takes the place of energy in this system with a broken continuous translational symmetry in time, just like the quasi-momentum replaces momentum in a system with a broken continuous translational symmetry in space. As $\Phi(t)$ is periodic in time, we can write down its Fourier series:

$$\Phi(t) = \sum_{m=-\infty}^{\infty} e^{im\omega t} \Phi^{(m)} \quad (2.94)$$

Inserting eq. 2.94 and eq. 2.86 into eq. 2.92, leads to an equation defining the Fourier coefficients $\Phi^{(m)}$ (see appendix E.1):

$$(m\hbar\omega - \varepsilon) \Phi^{(m)} + \sum_{m'=-\infty}^{\infty} \hat{H}^{(m-m')} \Phi^{(m')} = 0 \quad (2.95)$$

Just as in the case of Bloch functions, this can be seen as an eigenvalue/eigenvector problem:

$$\begin{pmatrix} \ddots & \vdots & \vdots & \vdots & \vdots & \vdots & \ddots \\ \dots & -(2\hbar\omega + \varepsilon)\mathbb{1} + \hat{H}^{(0)} & \hat{H}^{(-1)} & \hat{H}^{(-2)} & \hat{H}^{(-3)} & \hat{H}^{(-4)} & \dots \\ \dots & \hat{H}^{(1)} & -(\hbar\omega + \varepsilon)\mathbb{1} + \hat{H}^{(0)} & \hat{H}^{(-1)} & \hat{H}^{(-2)} & \hat{H}^{(-3)} & \dots \\ \dots & \hat{H}^{(2)} & \hat{H}^{(1)} & -\varepsilon\mathbb{1} + \hat{H}^{(0)} & \hat{H}^{(-1)} & \hat{H}^{(-2)} & \dots \\ \dots & \hat{H}^{(3)} & \hat{H}^{(2)} & \hat{H}^{(1)} & (\hbar\omega - \varepsilon)\mathbb{1} + \hat{H}^{(0)} & \hat{H}^{(-1)} & \dots \\ \dots & \hat{H}^{(4)} & \hat{H}^{(3)} & \hat{H}^{(2)} & \hat{H}^{(1)} & (2\hbar\omega - \varepsilon)\mathbb{1} + \hat{H}^{(0)} & \dots \\ \ddots & \vdots & \vdots & \vdots & \vdots & \vdots & \ddots \end{pmatrix} \begin{pmatrix} \vdots \\ \Phi^{(-2)} \\ \Phi^{(-1)} \\ \Phi^{(0)} \\ \Phi^{(1)} \\ \Phi^{(2)} \\ \vdots \end{pmatrix} = \mathbf{0}. \quad (2.96)$$

This matrix shows close resemblance to the case of a quantum system driven by coherent radiation described by the dressed-state picture [170]. A bit of insight can be gained by looking at the matrix this way: The diagonal blocks are the time-average of the Hamiltonian, offset by integer multiples of the driving energy quantum. The off-diagonal blocks mediate the coupling of the diagonal blocks and are the harmonics of the Hamiltonian. This means that in the case of harmonic (i.e. sinusoidal) driving, just as in the case of a sinusoidal lattice, only the terms $\hat{H}^{(-1)}$, and $\hat{H}^{(1)}$ will differ from zero. Higher order transitions can only be mediated by absorbing/emitting many photons at once from/into the drive. Like in the case of Bloch functions, this problem can be approached by truncating the determinant to a finite number of blocks. There is however another approach: If the kick operator \hat{K}_F , the micro motion operator \hat{M}_F and the effective Hamiltonian \hat{H}_F are known, the dynamics can be computed numerically (all these operators will be introduced in the next section).

If we take a look at eq. 2.88, we can see that energies are only defined modulo $\hbar\omega$:

$$\psi(t) = e^{-i\frac{\varepsilon_1}{\hbar}t} \Phi_1(t) \quad (2.97)$$

$$= e^{-i\frac{\varepsilon_1 + \hbar\omega}{\hbar}t} e^{i\omega t} \Phi_1(t) \quad (2.98)$$

$$:= e^{-i\frac{\varepsilon_2}{\hbar}t} \Phi_2(t) \quad (2.99)$$

This means that we can identify states with energies that differ by multiples of $\hbar\omega$ and restrict ourselves to a Brillouin zone [169] of e.g. $\varepsilon \in [0, \hbar\omega]$, like in the case of a Hamiltonian that is periodic in space.

2.6.2 Transformation to the Floquet Frame

We will now show how the dynamics of the driven system can be described more elegantly by transforming the system into another frame using the unitary micro-motion operator $\hat{M}_F(t)$ ¹. In this frame, the dynamics will be described by the time-independent effective Hamiltonian \hat{H}_F .

Because we are concerned with finite time scales, we can restrict ourselves to a finite Hilbert space [169, 171] and we can construct a periodic operator $\hat{M}_{F'}(t) \stackrel{!}{=} \hat{M}_{F'}(t+T)$, called micro-motion operator that transforms the Floquet states $\psi(t)$ in such a way that the transformed state $\psi_{F'}(t)$ evolves according to a time-independent effective Hamiltonian $\hat{H}_{F'}$ (the frame labeled F' will help us get to a nicer frame F where the micro-motion operator $\hat{M}_F(t_0) = \mathbb{1}$ for an arbitrary t_0) [169]:

$$\psi(t) := \hat{M}_{F'}(t) \psi_{F'}(t) \quad (2.100)$$

$$\Rightarrow \hat{H}_{F'} = \hat{M}_{F'}^\dagger(t) \hat{H}(t) \hat{M}_{F'}(t) - i\hbar \hat{M}_{F'}^\dagger(t) \dot{\hat{M}}_{F'}(t), \quad (2.101)$$

with the effective Hamiltonian $\hat{H}_{F'}$ (a derivation of $\hat{H}_{F'}$ can be found in appendix E.2). We denote this frame of reference as F' because we will now change to a more convenient one labeled F . We now define the time-evolution operator $\hat{U}(t, t_0)$ [169]:

$$\hat{U}(t, t_0) := \mathcal{T}_t e^{-\frac{i}{\hbar} \int_{t_0}^t dt' \hat{H}(t')}, \quad (2.102)$$

with the time-ordering operator \mathcal{T}_t . Appendix E.3 shows how the effective Hamiltonian $\hat{H}_{F'}$ can be used to simplify $\hat{U}(t, t_0)$ by transforming to the Floquet frame and back [169]:

$$\hat{U}(t, t_0) = \hat{M}_{F'}(t) e^{-\frac{i}{\hbar} (t-t_0) \hat{H}_{F'}} \hat{M}_{F'}^\dagger(t_0). \quad (2.103)$$

As a final simplification, we can now invoke a second, time-independent unitary transformation. This will leave the resulting Hamiltonian time-independent, but can simplify the stroboscopic dynamics. As the unitary operator, we choose $\hat{M}_{F'}(t_0)$ and define a new micro-motion operator $\hat{M}_F(t)$:

$$\hat{M}_F(t) := \hat{M}_{F'}(t) \hat{M}_{F'}^\dagger(t_0), \quad (2.104)$$

So for an arbitrary t_0 , we can set $\hat{M}_F(t_0) = \mathbb{1}$.

$$\hat{H}_F = \hat{M}_{F'}(t_0) \hat{H}_{F'} \hat{M}_{F'}^\dagger(t_0) \quad (2.105)$$

¹Micro-motion operators are canonically usually labeled $\hat{U}_F(t)$, but we choose $\hat{M}_F(t)$ to avoid a mix up with the time-evolution operators $\hat{U}(t, t_0)$ and $\hat{U}_F(t, t_0)$

With this Hamiltonian, the time-evolution operator $\hat{U}(t, t_0)$ (eq. 2.103) becomes [169]:

$$\hat{U}(t, t_0) = \hat{M}_{F'}(t) \hat{M}_{F'}^\dagger(t_0) e^{-\frac{i}{\hbar}(t-t_0)\hat{H}_F} \quad (2.106)$$

For evolution over full cycles, we can use the periodicity of $\hat{M}_{F'}(t)$ to get the stroboscopic time-evolution operator $\hat{U}(t_0+nT, t_0)$:

$$\hat{U}(t_0+nT, t_0) = e^{-\frac{i}{\hbar}nT\hat{H}_F}, \quad (2.107)$$

The time-evolution operator $\hat{U}(t_1, t_2)$ has the following interesting properties [172] (a derivation can be found in appendix E.3):

$$\hat{U}(nT+t_0+t, nT+t_0) = \hat{U}(t_0+t, t_0) \quad (2.108)$$

$$\hat{U}(nT+t, 0) = \hat{U}(t, 0) \hat{U}(nT, 0) \quad (2.109)$$

$$\hat{U}(nT, 0) = \hat{U}(T, 0)^n \quad (2.110)$$

The first equation (eq. 2.108) represents periodicity of $\hat{U}(t_1, t_2)$ with respect to a shift by multiples of the driving period T . Eq. 2.109 shows how the time-evolution over an integer number of cycles can be split from $\hat{U}(t_1, t_2)$. Finally, we can see how repeated time-evolution over one cycle mediates evolution over many cycles from eq. 2.110.

We can also define the periodic kick operator $\hat{K}_F(t)$ which describes the effect of instantly switching on the drive [104]:

$$\hat{M}_F(t) := e^{-i\hat{K}_F(t)} \quad (2.111)$$

2.6.3 Properties

For completeness, we should mention a few properties of Floquet systems. It makes sense to define a new extended Floquet Hilbert space $\mathcal{F} = \mathcal{H} \otimes \mathcal{T}$ for the Floquet modes $\Phi(t)$, where \mathcal{H} is the original Hilbert space of \mathcal{L}^2 -integrable functions, with a scalar product of [169]:

$$\langle v(\mathbf{r}) | w(\mathbf{r}) \rangle = \int d\mathbf{r} v^*(\mathbf{r}) w(\mathbf{r}), \quad (2.112)$$

and \mathcal{T} is the Hilbert space of functions that are periodic with period T and have a scalar product according to:

$$\langle v(t) | w(t) \rangle = \frac{1}{T} \int_0^T dt v^*(t) w(t). \quad (2.113)$$

The new scalar product of \mathcal{F} is then denoted by $\langle\langle v(\mathbf{r}, t) | w(\mathbf{r}, t) \rangle\rangle$ and defined according to:

$$\langle\langle v(\mathbf{r}, t) | w(\mathbf{r}, t) \rangle\rangle = \frac{1}{T} \int_0^T dt \int d\mathbf{r} v^*(\mathbf{r}, t) w(\mathbf{r}, t). \quad (2.114)$$

If the driving frequency ω is large compared to the inverse of characteristic time scales, i.e. elements of the Hamiltonian, an inverse frequency expansion [104, 169, 173–175] can be used to approximate the problem. Due to the driving frequency determining the largest energy scale in this case, this is called a high-frequency expansion:

$$\hat{H}_F \approx \sum_{m=1}^{m_{\max}} \hat{H}_F^{(m)} \quad (2.115)$$

$$\hat{H}_F^{(1)} = \hat{H}^{(0)} \quad (2.116)$$

$$\hat{H}_F^{(2)} = \sum_{m \neq 0} \frac{\hat{H}^{(m)} \hat{H}^{(-m)}}{m \hbar \omega} \quad (2.117)$$

$$\hat{H}_F^{(3)} = \sum_{m \neq 0} \left(\frac{[\hat{H}^{(-m)}, [\hat{H}^{(0)}, \hat{H}^{(m)}]]}{2(m \hbar \omega)^2} + \sum_{m' \neq \{0, m\}} \frac{[\hat{H}^{(-m')}, [\hat{H}^{(m'-m)}, \hat{H}^{(m)}]]}{3mm' (\hbar \omega)^2} \right), \quad (2.118)$$

with $\hat{H}^{(m)}$ the Fourier component according to eq. 2.87. Variants include the Floquet-Magnus expansion [176–178].

2.6.4 Transformation to the Rotating Frame

While we do now have the necessary tools to compute the time-evolution of a Floquet system, it is still a bit cumbersome to do in the present reference frame. However, the Hamiltonian can be simplified by a transformation to the rotating frame. We will now show how this transformation can be performed.

A Hamiltonian that is periodic in time can always be put in the following form:

$$\hat{H}(t) = \hat{H}_0 + \lambda(t) \hat{H}_1, \quad (2.119)$$

A transformation $\hat{V}^\dagger(t)$ that removes \hat{H}_1 from the Hamiltonian is called a transformation to the rotating frame [179] (by convention $\hat{V}(t)$ describes the transformation from the rotating frame to the lab frame). The transformed Hamiltonian \hat{H}^{rot} is equal to (see appendix E.4):

$$|\psi^{\text{rot}}\rangle = \hat{V}^\dagger(t) |\psi\rangle \quad (2.120)$$

$$\hat{H}^{\text{rot}}(t) \stackrel{!}{=} \hat{V}^\dagger(t) \hat{H}_0 \hat{V}(t) \quad (2.121)$$

$$\Rightarrow \hat{V}(t) = e^{-\frac{i}{\hbar} \hat{H}_1 \int_{t_0}^t dt' \lambda(t')} \quad (2.122)$$

From eq. 2.121 we see that there is a transformation $\hat{V}(t)$ to a frame, that yields a Hamiltonian that is void of the original time-dependent part $\lambda(t)$, at the cost of potentially introducing a time-dependence in the original Hamiltonian \hat{H}_0 (unless \hat{H}_0 and $\hat{V}(t)$ commute). In our experiment, the Hamiltonian belongs to the Dunlap-Kenkre class as it features periodic coupling to the single particle potential and to the Kapitza class as it is quadratic in momentum [179]. Applied to our time-periodic extension of the Bose-Hubbard Hamiltonian (eq. 2.65), we make the following transformation (see appendix E.4):

$$\hat{H}(t) = -J \sum_j (\hat{a}_j^\dagger \hat{a}_{j+1} + \hat{a}_{j+1}^\dagger \hat{a}_j) + K \cos(\omega t) \sum_j j \hat{n}_j + \frac{U}{2} \sum_j \hat{n}_j (\hat{n}_j - 1) \quad (2.123)$$

$$\Rightarrow \hat{V}(t) = e^{-i \frac{K}{\hbar} \sum_j j \hat{n}_j \int_{t_0}^t dt' \cos(\omega t')}, \quad (2.124)$$

with J the tunneling, K the driving amplitude and U the on-site interaction energy. For $t_0=0$ and $\alpha = \frac{K}{\hbar\omega}$ the driving strength, $\hat{V}(t)$ evaluates to:

$$\hat{V}(t) = e^{-i\alpha \sin(\omega t) \sum_j j \hat{n}_j} \quad (2.125)$$

Appendix E.4 shows how this transformation leads to the rotating Hamiltonian $\hat{H}^{\text{rot}}(t)$ [164]:

$$\hat{H}^{\text{rot}}(t) = -J \sum_{(i,j)} \left(e^{-i\alpha \sin(\omega t)} \hat{a}_i^\dagger \hat{a}_j + e^{i\alpha \sin(\omega t)} \hat{a}_j^\dagger \hat{a}_i \right) + \frac{U}{2} \sum_j \hat{n}_j (\hat{n}_j - 1) \quad (2.126)$$

Effectively, we created a Hamiltonian $\hat{H}^{\text{rot}}(t)$ that is stripped of the former driving part and instead features a periodically modulated hopping element.

2.6.5 Renormalized Tunneling

Eq. 2.126 tells us that the Hamiltonian of the driven system can be seen (in the rotating frame) as a Hamiltonian with unchanged interactions, but a hopping that is modulated over a full cycle. As a final simplification, we will now get rid of this time-dependence in the hopping by averaging over a full cycle. This makes sense from an experimental point of view because we will probe the driven system stroboscopically after an integer number of cycles. A mathematically rigorous derivation of this renormalization of the tunneling can be found in appendix B of [104].

$\hat{H}^{\text{rot}}(t)$ can now be averaged over a full driving cycle using:

$$\frac{1}{T} \int_0^T dt e^{\pm i\alpha \sin(\omega t)} = \mathcal{J}_0(\alpha), \quad (2.127)$$

with \mathcal{J}_0 the zeroth Bessel function of the first kind.

$$\hat{H}_{\text{eff}} := \frac{1}{T} \int_0^T dt \hat{H}^{\text{rot}}(t) \quad (2.128)$$

$$= -J \mathcal{J}_0(\alpha) \sum_j (\hat{a}_j^\dagger \hat{a}_{j+1} + \hat{a}_{j+1}^\dagger \hat{a}_j) + \frac{U}{2} \sum_j \hat{n}_j (\hat{n}_j - 1) \quad (2.129)$$

$$\hat{H}_{\text{eff}} = -J_{\text{eff}} \sum_j (\hat{a}_j^\dagger \hat{a}_{j+1} + \hat{a}_{j+1}^\dagger \hat{a}_j) + \frac{U}{2} \sum_j \hat{n}_j (\hat{n}_j - 1) \quad (2.130)$$

Here, we introduced the renormalized tunneling [130] $J_{\text{eff}} := J \mathcal{J}_0(\alpha)$. We can see from eq. 2.130 that for integer cycles the driven system to first order in a high-frequency expansion effectively behaves as though its hopping element had been changed. Because $\mathcal{J}_0(\alpha)$ can also go to zero or even assume negative values, periodic driving allows for the realization of interesting effects, namely dynamical localization for $J_{\text{eff}}=0$ or an inverted band that is adiabatically connected to the lowest band in the un-driven case with its maximum at $q=0$ and minimum at the BZ edge for $J_{\text{eff}}<0$ [124].

In figure 2.6, we see the renormalized tunneling elements used in the experiment.

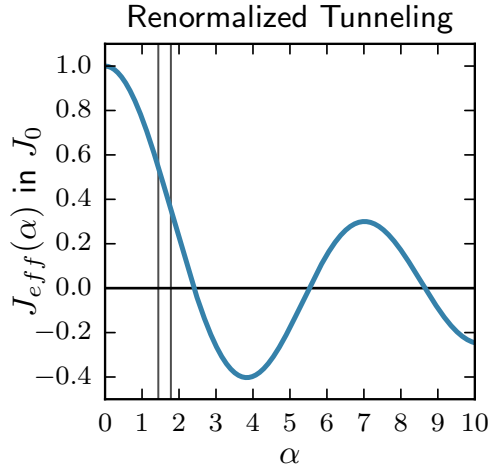


Figure 2.6: The **effective tunneling** J_{eff} is shown as a function of driving strength α . The **vertical lines** indicate the position of $\alpha_1 = 1.44$ and $\alpha_2 = 1.78$, the driving strengths used in the experiments.

2.6.6 Floquet Fermi's Golden Rule

Fermi's golden rule (FGR) [180, 181] can be used to calculate transition rates in various quantum mechanical system. In the case of a periodically driven system, it is usually referred to as Floquet Fermi's golden rule (FFGR). However, there are two limits linked to this method. The transition has to go into a continuum of states, which means that transition times have to be small compared to level spacing, so individual levels can't be resolved. This is usually true in the case of a periodic lattice structure. The other limit is, however, that transition times have to be large compared to inverse driving frequencies,

which means that the FFGR ansatz only yields meaningful results after multiple driving cycles. That means that since in this work we want to measure the onset of excitations over the first few driving cycles, we expect the FFGR ansatz to be invalid. However, for comparison, we will briefly give an overview of the relevant formulas and use them to show the difference in timescales between FFGR decay rates and the growth rate of excitations in the experiment. In general, FFGR results in a differential equation for the atom number in the BEC N_0 of the form:

$$\dot{N}_0(t) = -\Gamma_{\text{FFGR}} N_0(t), \quad (2.131)$$

which means there's an exponential decay of the BEC with rate Γ_{FFGR} . In the case of a BEC confined in a harmonic trap (see chapter 3.1), the rate Γ_{FFGR} depends on the atom number N_0 , because density changes with atom number, as described by the Thomas-Fermi model (see chapter 2.5). This changes the form of the decay slightly from being exponential, see figure 2.7. These transition rates were studied by our team and theoretically explained in [146]. However, as we are only interested in the low depletion limit, we can assume N_0 to be constant for our estimates. In the case of a driving frequency that lies below the band gap between the two lowest bands (as is the case in the experiments performed for this work), loss rates can be computed according to the intra-band heating rates for harmonically trapped condensates[146]:

$$\dot{N}_0(t) = -\Gamma_{\text{FFGR}} N_0(t) \quad (2.132)$$

$$\Gamma_{\text{FFGR}} = \frac{24\pi}{7d} 15^{2/5} \frac{m_K}{\hbar}^{1/5} \omega_H^{6/5} \zeta^{7/5} \left(\frac{J}{\hbar\omega}\right)^2 a^{7/5} \mathcal{J}_2(\alpha)^2 \cdot \left(k_{\text{max}} - \frac{8 \sin(dk_{\text{max}})}{3d} + \frac{\sin(dk_{\text{max}})}{3d}\right) \quad (2.133)$$

$$k_{\text{max}} = \begin{cases} \frac{\arccos\left(1 - 2\frac{\omega}{\omega_{BW}}\right)}{d} & \omega \leq \omega_{BW} \\ \frac{\pi}{d} & \omega > \omega_{BW} \end{cases} \quad (2.134)$$

$$\omega_{BW} = \frac{4J \mathcal{J}_0(\alpha)}{\hbar}, \quad (2.135)$$

with ω_{BW} the effective bandwidth, J the tunnel element of the still lattice, $\mathcal{J}_n(\cdot)$ the n -th Bessel function of the first kind, \hbar the reduced Planck's constant, k_{max} indicating the highest mode available for scattering, m_K the mass of a potassium atom, $\omega_H = \sqrt[3]{\omega_x \omega_y \omega_z}$, $\zeta = w_{0l} d$ the zeta parameter as defined in sec. 2.5.2, ω the (angular) driving frequency and a the scattering length.

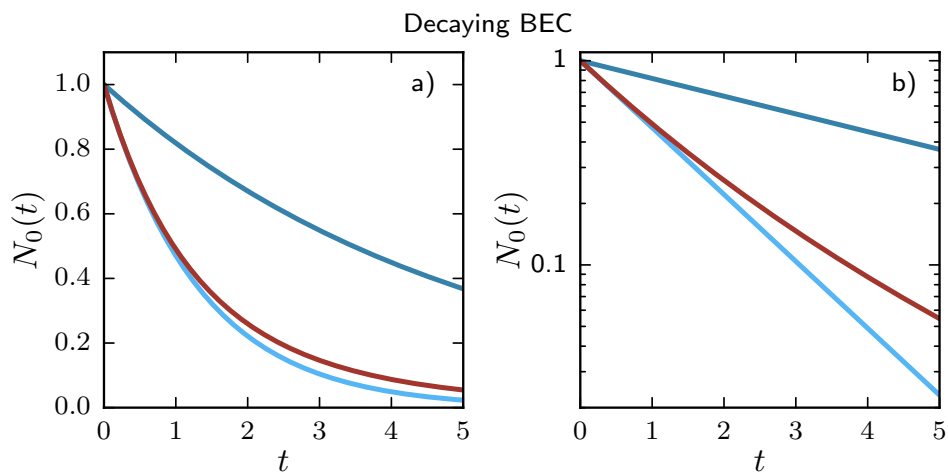


Figure 2.7: Decay of the condensate (normalized to $N_0 = 1$, arbitrary time axis). The **red** line obeys the differential equation $\dot{N}_0(t) = -\kappa_{bg} N_0(t) - \kappa N_0^{\frac{7}{5}}(t)$ that combines the exponential decay due to collisions with particles from the background gas in the chamber with rate κ_{bg} with the decay predicted by a Floquet Fermi's Golden rule approach. The blue lines show exponential decays for reference. **Dark blue:** decay according to $\dot{N}_0(t) = -\kappa_{bg} N_0(t)$, **light blue:** decay according to $\dot{N}_0(t) = -\kappa'_{bg} N_0(t)$, with $\kappa'_{bg} = \kappa_{bg} + \kappa N_0^{\frac{2}{5}}(t=0)$ chosen so its initial rate equals the red line. Left and right panel show the same curves on **a)** linear and **b)** logarithmic scale.

2.7 Parametric Oscillator

The instabilities observed in our experiment on ultra-cold atoms can be mapped on the quantum mechanical version of a parametric oscillator. In this chapter, we explain what a parametric oscillator is in the classical case and show how its dynamics can be solved. We then reveal the connections to the excitations in the Bogoliubov Hamiltonian.

2.7.1 Classical Parametric Oscillator

Any system whose dynamics can be described by a homogeneous differential equation of second order:

$$\ddot{x}(t) + \beta(t) \dot{x}(t) + \omega^2(t) x(t) = 0, \quad (2.136)$$

with $\beta(t)$ and $\omega^2(t)$ having a common period (i.e. their periods are commensurable) can be mapped onto the Hill differential equation (for derivation see appendix F.1) [182, 183]:

$$\ddot{q}(t) + \omega'^2(t) q(t) = 0 \quad (2.137)$$

$$x(t) := q(t) e^{-\frac{1}{2} \int_0^t dt' \beta(t')} \quad (2.138)$$

$$\omega'^2(t) := \omega^2(t) - \frac{1}{4} \beta^2(t) - \frac{1}{2} \dot{\beta}(t), \quad (2.139)$$

which G. W. Hill introduced when investigating the movement of the lunar perigee (closest point to earth) [184]. Performing a Fourier series expansion of ω'^2 , keeping just the two lowest order terms we end up with the differential equation of the parametric oscillator:

$$0 = \ddot{q}(t) + \omega_0^2 (1 + A \cos(\Omega t)) q(t) \quad (2.140)$$

$$\omega_0^2 := \frac{1}{T} \int_0^T dt \omega'^2(t). \quad (2.141)$$

Here, ω_0^2 is the temporal average of ω'^2 , Ω the largest common frequency of $\beta(t)$ and $\omega^2(t)$, and $\omega_0^2 A$ the series coefficient. A system described by this equation is called a parametric oscillator. The name stems from the fact that it resembles a harmonic oscillator with its eigen-frequency as a modulated parameter.

The most famous case of a parametric oscillator is the vertically forced pendulum, also called Kapitza pendulum [185, 186]. The eigen-frequency of a pendulum is $\omega_0 = \sqrt{\frac{g}{L}}$ with g the gravitational acceleration and L the length of the pendulum. This eigen-frequency can be modulated by varying L as in the case of a pendulum consisting of a thread and a mass particle with periodic pulling on the thread and a fixed suspension point (see figure 2.8) or by varying g as in the case of a mass particle attached to a solid rod with

a suspension point that is moved up and down periodically. In both cases, the instability of the parametric oscillator will lead to a rapid growth of the oscillation amplitude until losses, that are not included in this model, damp out further intake of energy.

Parametric Oscillator

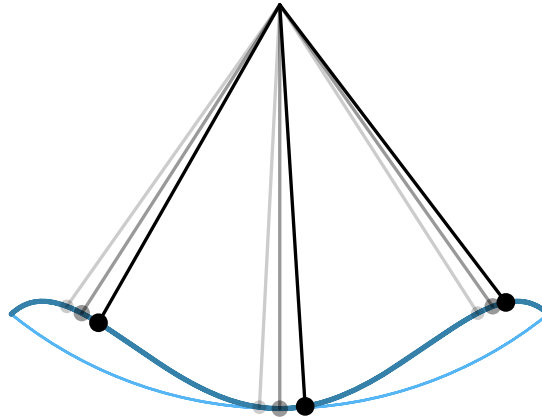


Figure 2.8: Parametric Oscillator: A string attached to a mass particle (**black**) is pulled periodically so it reaches its maximum length whenever the particle goes through the center or a turnaround point. Its motion follows the **dark blue** curve. The **light blue** curve shows the motion of a harmonic oscillator for reference.

In the case of a thread being pulled periodically over a fixed suspension point, it is intuitively understandable that a resonance will occur if the thread is pulled whenever the pendulum crosses its lowest point. Because there are two crossings in every period, the driving frequency has to be equal to twice the eigen-frequency. This can be tested easily on a playground with a sturdy swing: While from a sitting position it is commonly driven harmonically [187], it can be driven parametrically from a standing position by raising and lowering one's center of mass [188]. In the first case the period of one's movement will be equal to the swing's period, while it will be halved in the second case.

This motivates a transformation of parameters to $\Omega := 2\omega_0 + \varepsilon$, so we can analyze the system for small deviations $|\varepsilon| \ll \omega_0$ from the expected resonance $2\omega_0$.

While the driven harmonic oscillator always oscillates with the driving frequency, the parametric oscillator's dynamics is governed by the current eigen-frequency $\omega_0^2(1 + A\cos(\Omega t))$ on short timescales $\Delta t \ll \frac{1}{\Omega}$. Its equation of motion can be retrieved with the ansatz:

$$q(t) = c_1(t) \cos\left(\frac{\Omega}{2} t\right) + c_2(t) \sin\left(\frac{\Omega}{2} t\right) \quad (2.142)$$

Ansatz 2.142 leads to the following differential equations for the time-evolution of the parameters $c_1(t)$ and $c_2(t)$, see appendix F.2 [186]:

$$\ddot{c}_1(t) = \frac{1}{16} c_1(t) (\omega_0^2 A^2 - \varepsilon^2) \quad (2.143)$$

$$\ddot{c}_2(t) = \frac{1}{16} c_2(t) (\omega_0^2 A^2 - \varepsilon^2) \quad (2.144)$$

We can see from eqs. 2.143 and 2.144 that $c_1(t)$ and $c_2(t)$ obey the same differential equation and will differ only by their initial conditions. We can thus limit our analysis on $c_1(t)$ (eq. 2.143) and choose the ansatz:

$$c_1(t) = c e^{\gamma t}, \quad (2.145)$$

which trivially results in:

$$\gamma = \pm \frac{1}{4} \sqrt{\omega_0^2 A^2 - \varepsilon^2}. \quad (2.146)$$

Because a negative sign results in an exponentially decreasing term, we can neglect its contribution on long timescales, as long as the square root retains a real value, which it will do for $|\varepsilon| < \omega_0 A$, which is the width of the resonance.

To summarize, in contrast to the harmonic oscillator that can be driven at any frequency, the parametric oscillator has a resonance with a finite width $2\omega_0 A$. For small detunings within the resonance $|\varepsilon| < \omega_0 A$, the parametric oscillator is unstable and its amplitude grows exponentially, with the instability rate $\gamma = \pm \frac{1}{4} \sqrt{\omega_0^2 A^2 - \varepsilon^2}$:

$$q(t) = c_1 e^{\gamma t} \cos\left(\frac{\Omega}{2} t\right) + c_2 e^{\gamma t} \sin\left(\frac{\Omega}{2} t\right), \quad (2.147)$$

In contrast to the driven harmonic oscillator, there will be an oscillating amplitude and no net intake of energy from the drive for large detunings $|\varepsilon| \geq \omega_0 A$.

2.7.2 Mapping to Bogoliubov Hamiltonian

The quantum mechanical version of the parametric oscillator can be mapped onto the Bogoliubov Hamiltonian [164]. We will show this by mapping onto Hamiltonian eq. 2.43. We start by writing down the quantum mechanical version of the parametric oscillator:

$$\hat{H} = \frac{\hat{p}^2}{2m} + \frac{1}{2} m \omega_0^2 (1 + \alpha \cos(\Omega t)) \hat{x}^2 \quad (2.148)$$

Standard annihilation operators $\hat{\gamma}$ are used like for the harmonic oscillator:

$$\hat{\gamma} := \sqrt{\frac{m \omega_0}{2}} \left(\hat{x} + i \frac{\hat{p}}{m \omega_0} \right) \quad (2.149)$$

Appendix F.3 shows how inserting this annihilation operator in the Hamiltonian and then shifting by a trivial time-dependent energy offset, results in:

$$\hat{H}_{\text{para}} = \omega_0 \left(1 + \frac{\alpha}{2} \cos(\Omega t) \right) \hat{\gamma}^\dagger \hat{\gamma} + \frac{\alpha \omega_0}{4} \cos(\Omega t) \left(\hat{\gamma}^\dagger \hat{\gamma}^\dagger + \hat{\gamma} \hat{\gamma} \right) \quad (2.150)$$

At this point, we can see the correspondence with Hamiltonian 2.43 if we identify the modes \mathbf{q} and $-\mathbf{q}$. This step is justified because these modes will always be excited together.

2.8 Bogoliubov-de Gennes Formalism

The Bogoliubov-de Gennes formalism can be used to study the time-evolution of the condensate excitations [189]. We change to the Heisenberg formalism, i.e. we put the time-dependence in the operators, derive Heisenberg's equations of motion (EOM) for the annihilation operator \hat{b}_q and then perform the Bogoliubov transformation.

2.8.1 Bogoliubov-de Gennes Equations of Motion

We use a Bogoliubov Hamiltonian in the Heisenberg's EOM and for $q \neq 0$ we get (see appendix G):

$$\hat{H} = -\frac{g N_0}{2} + \sum_{q>0} \left((\varepsilon_q^0 + g) (\hat{b}_q^\dagger \hat{b}_q + \hat{b}_{-q}^\dagger \hat{b}_{-q}) + g (\hat{b}_q^\dagger \hat{b}_{-q}^\dagger + \hat{b}_q \hat{b}_{-q}) \right)$$

$$i \hbar \partial_t \hat{b}_q(t) = [\hat{b}_q(t), \hat{H}(t)] \quad (2.151)$$

$$= (\varepsilon_q^0 + g) \hat{b}_q(t) + g \hat{b}_{-q}^\dagger(t) \quad (2.152)$$

At this point, we perform the Bogoliubov transformation (eqs. 2.49 and 2.50) and put the time dependence into the factors u_q and v_q [164]:

$$\hat{b}_q(t) = u_q(t) \hat{\alpha}_q - v_q(t) \hat{\alpha}_{-q}^\dagger \quad (2.153)$$

$$\hat{b}_{-q}(t) = u_q(t) \hat{\alpha}_{-q} - v_q(t) \hat{\alpha}_q^\dagger \quad (2.154)$$

Appendix G shows how to get two equivalent forms of the time-derivative of \hat{b}_q from eqs. 2.152 and 2.153. By comparison of coefficients of $\hat{\alpha}_q$, we arrive at the coupled equations of motion for u_q and v_q , the Bogoliubov-de Gennes (BdG) equations:

$$i \hbar \partial_t \begin{pmatrix} u_q(t) \\ v_q(t) \end{pmatrix} = \begin{pmatrix} \varepsilon_q^0 + g & -g \\ g & -\varepsilon_q^0 - g \end{pmatrix} \begin{pmatrix} u_q(t) \\ v_q(t) \end{pmatrix} \quad (2.155)$$

The stroboscopic propagator matrix $\Phi(T)$ is obtained by evolving eq. 2.155 over a complete driving cycle. Its eigenvalues ε_q with a positive imaginary part indicate unstable modes of the system. They grow with the rate $s_q = \frac{1}{\hbar} \text{Im}(\varepsilon_q)$. Since this growth is exponential, the most unstable mode quickly dominates all others and the instability rate of the system can be defined as $\Gamma = \max_q s_q$. The position of the most unstable mode is $q_{\text{mum}} = \text{argmax}_q s_q$ [164].

2.8.2 Parametric Oscillator Mapping

The BdG equations of motion (eqs. 2.155) can be mapped to a parametric oscillator [190, 191].

For the case present in our experiments, this corresponds to assigning a parametric oscillator $\ddot{q}(t) + \omega_0^2(1 + A \cos(\Omega t))q(t) = 0$ (see equation 2.140) to each momentum mode [164]. The following substitutions have to be made [192]:

- The driving frequency Ω is substituted with 2ω , with ω the driving frequency in the experiment. The factor of 2 emerges from the fact that absorption of a single photon is not possible due to conservation of momentum [164]. Instead, two atoms absorb two photons and are excited to opposing momentum states.
- The natural frequency ω_0 is substituted with the effective Bogoliubov dispersion $E_{\text{eff}}^B(\mathbf{q})/\hbar$ (which corresponds to the dispersion term $\varepsilon_q^0 + g$ in the previous section).
- The amplitude A is substituted with A_q , an amplitude that depends on momentum.

In our experiment, the tunneling element in the still lattice is $J/\hbar = (108 \pm 7)$ Hz and the interaction parameter $g/\hbar = (870 \pm 100)$ Hz, so for the driving amplitudes $\alpha_1 = 1.44$ and $\alpha_1 = 1.78$ used in the experiment, we get $J_{\text{eff},1} = (59 \pm 4)$ Hz and $J_{\text{eff},1} = (38 \pm 2)$ Hz, see figure 2.9.

With a change of basis and dropping all terms that are irrelevant to the emergence of parametric instabilities, eqs. 2.155 become (this can in detail be seen in the supplementary material of [190] - to make the notation equivalent, we set $\hbar = d = 1$ for the rest of this section) [192]:

$$i\hbar \partial_t \begin{pmatrix} \bar{u}_q \\ \bar{v}_q \end{pmatrix} = \begin{pmatrix} E_{\text{eff}}^B(\mathbf{q}) & \frac{A_q}{2} E_{\text{eff}}^B(\mathbf{q}) \cos(2\omega t) e^{-2iE_{\text{eff}}^B(\mathbf{q})t} \\ -\frac{A_q}{2} E_{\text{eff}}^B(\mathbf{q}) \cos(2\omega t) e^{-2iE_{\text{eff}}^B(\mathbf{q})t} & E_{\text{eff}}^B(\mathbf{q}) \end{pmatrix} \begin{pmatrix} \bar{u}_q \\ \bar{v}_q \end{pmatrix} \quad (2.156)$$

with the effective, i.e. time-averaged Bogoliubov dispersion $E_{\text{eff}}^B(\mathbf{q})$ and the amplitude A_q [192]:

$$E_{\text{eff}}^B(\mathbf{q}) = \sqrt{\left(4 |J_{\text{eff}}| \sin^2\left(\frac{q_x}{2}\right) + \frac{q_{\perp}^2}{2m}\right) \left(4 |J_{\text{eff}}| \sin^2\left(\frac{q_x}{2}\right) + \frac{q_{\perp}^2}{2m} + 2g\right)} \quad (2.157)$$

$$A_q = 16J \mathcal{J}_2(\alpha) \sin^2\left(\frac{q_x}{2}\right) \frac{g}{E_{\text{eff}}^B(\mathbf{q})^2}, \quad (2.158)$$

where \mathcal{J}_2 denotes the second Bessel function of the first kind. We can now extract the instability properties of the system [189] and find that the system features resonances whenever the condition $\omega = E_{\text{eff}}^B(\mathbf{q})$ is met.

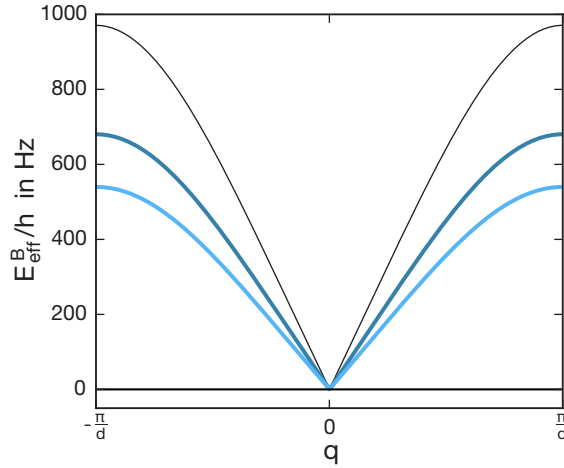


Figure 2.9: Effective Bogoliubov dispersion for driving amplitudes $\alpha_1 = 1.44$ (**dark blue**) and $\alpha_1 = 1.78$ (**dark blue**). The Bogoliubov dispersion of the still lattice is shown for reference (**black**). The respective bandwidths are $W_{\text{eff},1} = (680 \pm 30)$ Hz and $W_{\text{eff},2} = (540 \pm 30)$ Hz for the driven cases and $W_{\text{eff}} = (970 \pm 40)$ Hz in the still lattice.

The instability arises in a finite momentum range around this point and on resonance has the maximum instability rate Γ_q [192]:

$$\Gamma_q = \frac{1}{4\hbar} A_q E_{\text{eff}}^B(q_{\text{res}}) \quad (2.159)$$

$$= 4J \mathcal{J}_2(\alpha) \sin^2\left(\frac{q_{x,\text{res}}}{2}\right) \frac{g}{\hbar E_{\text{eff}}^B(q_{\text{res}})} \quad (2.160)$$

The resonance condition is usually met by a continuum of momenta (with different values for q_x and q_\perp), of which the maximally unstable mode always maximizes q_x [164].

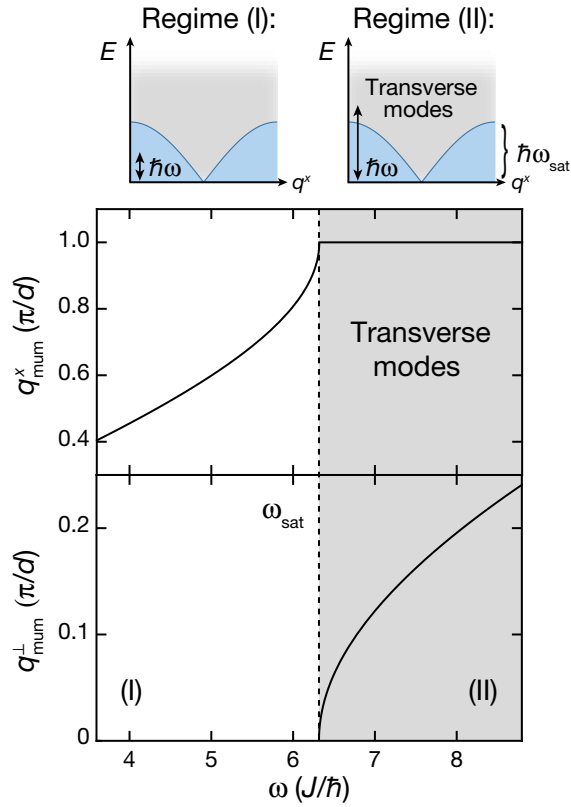


Figure 2.10: Top: Schematics of the Bogoliubov dispersion in the lattice direction (**blue**) with finite bandwidth $W_{\text{eff}} = \hbar\omega_{\text{sat}}$. The **gray area** illustrates the continuous unbounded spectrum of the transverse degrees of freedom.

Bottom: Momentum of the most unstable mode $q_{\text{mum}} = (q_{\text{mum}}^x, q_{\text{mum}}^\perp)$ as predicted by Bogoliubov theory for $\alpha_1 = 1.44$ and $g = 8.1 J$, which shows a clear separation between lattice (I) and transverse degrees of freedom (II) at $\omega = \omega_{\text{sat}}(\alpha_1) = 6.3 \frac{J}{\hbar}$. In 1D, regime (II) is stable. Figure adapted from [192].

We can distinguish two cases, which are depicted in figure 2.10:

(I) The driving frequency ω lies within the effective bandwidth $\omega < \sqrt{4|J_{\text{eff}}|(4|J_{\text{eff}}| + 2g)}$, the most unstable mode $\mathbf{q}_{\text{mum}} = (q_x, \mathbf{q}_\perp)$ and the instability rate Γ are [164]:

$$q_x = \frac{2\hbar}{d} \arcsin\left(\sqrt{\frac{\sqrt{g^2 + (\hbar\omega)^2} - g}{4|J_{\text{eff}}|}}\right) \quad (2.161)$$

$$\mathbf{q}_\perp = 0 \quad (2.162)$$

$$\Gamma = \frac{\sqrt{g^2 + (\hbar\omega)^2} - g}{\hbar} \left| \frac{\mathcal{J}_2(\alpha)}{\mathcal{J}_0(\alpha)} \right| \frac{g}{\hbar\omega} \quad (2.163)$$

(II) For larger driving frequencies ω , which lie above the effective bandwidth $\omega > \sqrt{4|J_{\text{eff}}|(4|J_{\text{eff}}| + 2g)}$, we have [164]:

$$q_x = \frac{\pi}{d} \quad (2.164)$$

$$|\mathbf{q}_\perp| = \sqrt{2m \sqrt{g^2 + (\hbar\omega)^2} - g - 4|J_{\text{eff}}|} \quad (2.165)$$

$$\Gamma = 4 \frac{J}{\hbar} \mathcal{J}_2(\alpha) \frac{g}{\hbar\omega} \quad (2.166)$$

2.8.3 Limitations of the Bogoliubov-de Gennes Description

The Bogoliubov approximation only holds if certain conditions are met. The first one is that interactions are small ($U \ll J$), so collisions between quasi-particles, which are not captured by the model, are rare. Also, the approximation starts from a constant condensate with a constant chemical potential. As the model does not conserve particle number, this condition is not met if there is distinct depletion from the BEC, as will be the case for heating at long time scales. Finally, it should be noted that extracting Lyapunov exponents to quantify the instability of a system can always just describe the instantaneous instability rate of the system in the initial state. If the system changes due to evolution in time, so can/will the rates.

Experimental Setup

All experiments were performed on a Bose-Einstein condensate (BEC) in an ultra-high vacuum. During the imaging, the condensate is destroyed by the energy intake from absorbing resonant light. So after every image, a new BEC has to be formed by cooling down vapor of $\approx 300\text{K}$ to a few tens of nK. This takes up most of the time in the preparation of each shot, $\approx 40\text{s}$ compared to the actual experiment with only $\approx 10\text{ms}$. The whole setup used to produce a BEC has been described in the PhD thesis of Lucia Duca [193]. In this part of this thesis, we shall give a brief summary of the setup and describe the most important principles.

In chapter 3.1 we give an overview of the experimental setup and the procedure for the production of the BEC.

We then move on to a more detailed description of the most important physical effects and experimental concepts for cooling of the atoms in chapter 3.2. These include the magneto-optical trap and optical molasses as a means for pre-cooling atoms, trapping and evaporative cooling in the quadrupole and dipole trap, and finally Feshbach resonances as a means of controlling interactions in a cloud of ultra-cold atoms.

The optical lattice is described in chapter 3.3, including the production of the lattice potential at the intersection of two blue detuned beams of light, the generation of inertial forces via acceleration of the lattice, and the band-mapping method to measure the band-resolved population of momentum-states.

Finally, the imaging procedure is explained in chapter 3.4, focusing on the challenges arising from the need to use high imaging intensities due to the high optical density of the cloud.

3.1 Setup

The first step in the production of a BEC of ^{39}K is to get a dilute gas of ^{39}K and ^{87}Rb in an ultra-high vacuum. A schematic of the setup can be seen in figure 3.1. ^{87}Rb is used to cool down ^{39}K more efficiently than it is possible with ^{39}K alone. This is done by attaching two ovens, one for each species, to the vacuum system and evaporating ^{39}K and ^{87}Rb from bulk material¹.

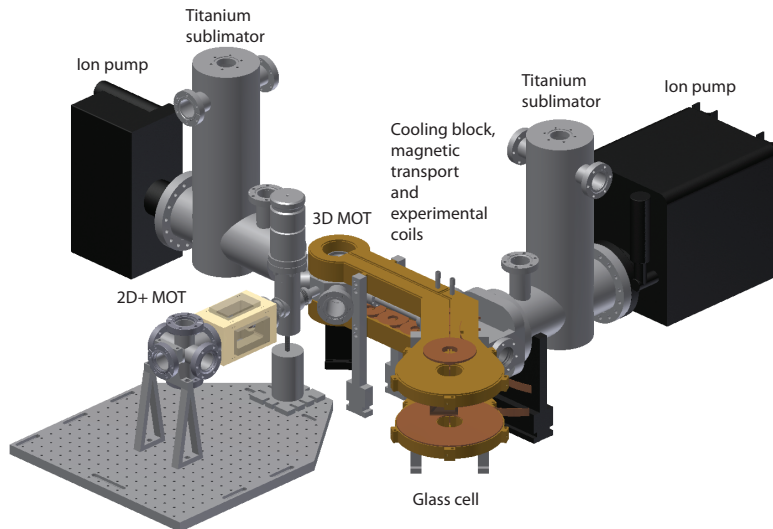


Figure 3.1: Experimental Setup. Schematic of the experimental setup without optics and the two ovens. The sequence begins in the 2D+ MOT (**beige**). From there, a beam of pre-cooled atoms is guided through a differential pumping section into the 3D MOT. After further cooling and spin polarizing, the atoms are magnetically transported through another differential pumping section into the science chamber by an array of anti-Helmholtz coil pairs (**brown**). The bend grants better optical access. In the science chamber, the atoms are finally cooled down to quantum degeneracy and experiments are performed. Image taken from [194].

A 2D+ magneto-optical trap (MOT) [195–199], which is a combination of magneto-optical Doppler cooling along two (transverse) dimensions and assisting molasses (see sec. 3.2.2) along the third dimension², is loaded from the background gas for initial pre-cooling of the atoms. A near resonant beam of light assists in the production of a beam of relatively cool atoms by pushing them with radiation pressure. The beam is pointed through a differential pumping section at the subsequent 3D MOT chamber. This makes it possible to have a relatively high pressure and thus a big reservoir of atoms in the 2D+ MOT and a lower pressure and thus longer lifetimes in the 3D MOT. In the center of the 3D MOT is a dark spot [200] ($\approx 9\text{mm}$ in diameter) that blocks the repumping beam so light-

¹After the MOT chamber has been flooded in the early stages of the experiment, the valves of the ovens now have been closed for years.

²The additional molasses cooling beam (labeled "axial cooling") is used for ^{39}K but not ^{87}Rb

assisted ^{39}K - $^{39}\text{K}^*$ collisions which can release a lot of kinetic energy can be suppressed at the point of highest density.

Here, the atoms are cooled from all three directions while a constant influx from the 2D+ MOT increases the atom number in the trap over time (this takes about 6.5s for ^{87}Rb and 0.5s for ^{39}K). The center of mass positions are slightly shifted against each other by a few mm via beam alignment, so losses from interspecies collisions are minimized.

At the end of the loading sequence, we increase the magnetic field by a factor of ≈ 1.3 , decrease the cooling power by a factor of ≈ 0.5 and adjust the detunings to go into the compressed MOT (cMOT) [201] phase, which lasts 10ms. This increases the density of the cloud. The parameters are chosen to yield a maximum number of atoms at minimum temperature after this phase. This phase results in a temperature of a few $100\mu\text{K}$.

Afterwards, the beam parameters are changed once more for the optical molasses (polarization gradient cooling) phase which takes 4.15ms and cools down the atoms below the Doppler temperature. The hyperfine splitting is very small for ^{39}K ($\approx 35\text{MHz}$ compared to a detuning of $\approx 40\text{MHz}$), so this step is not very effective there [202, 203].

Next, the atoms are subjected to a spin polarizing pulse that pumps them into the $|F=2, m_F=2\rangle$ state. Atoms that fail to reach this state are not captured by the following weaker quadrupole trapping phase.

From this quadrupole trap, there is a magnetic transport [204] performed by partially overlapped pairs of coils that brings the cloud through another differential pumping section into the science chamber, a glass cell with even lower pressure and no parallel surfaces to allow for optical access without Fabry-Pérot resonances.

Here, forced microwave evaporation is performed on ^{87}Rb in the quadrupole field of the last pair of coils for $\approx 10\text{s}$. To avoid Majorana losses in the center of the trap [205–207], where the sign of the field abruptly changes at the zero crossing so the spin of passing atoms can't adiabatically follow, a blue detuned optical "plug" beam (wavelength $\lambda = 760\text{nm}$, $30\mu\text{m}$ waist) projects a repulsive potential in the trap center [9, 208]. The microwave evaporation sweep transfers ^{87}Rb atoms at some distance from the trap center defined by the instantaneous frequency and thus a given minimum energy from the magnetically trapped $|F=2, m_F=2\rangle$ to the un-trapped $|F=2, m_F=0\rangle$ state. The frequency of this sweep is lowered over time to successively evaporate the hottest ^{87}Rb atoms, thus decreasing the overall temperature of the cloud. The duration of the sweep is set by the condition that the cloud needs keep to re-thermalizing for this step to be efficient. Meanwhile, ^{39}K is sympathetically cooled by ^{87}Rb - ^{39}K collisions [209].

To cool down the cloud even further, it is finally loaded into an optical dipole trap [210, 211] formed by two perpendicular high power beams of $\lambda = 1064\text{nm}$ light and all atoms are transferred to the $|F=1, m_F=1\rangle$ state with an RF-sweep. Any atoms remaining in the $|F=2, m_F=2\rangle$ state are blown away with a pulse of resonant light. Again, the most energetic particles are evaporated by slowly ramping down the trap confinement. Rapid thermalization is assured by controlling the scattering rate of ^{87}Rb - ^{39}K collisions with a Feshbach resonance [25, 212–214]. Near the end of the evaporation, the remaining much heavier ^{87}Rb atoms fall out of the trap as its confinement along the vertical direction

becomes too low to counteract gravity, leaving only ^{39}K behind. At that point, the Feshbach field is adjusted to mediate ^{39}K - ^{39}K collisions and allow for further cooling by evaporation of ^{39}K [214, 215] until quantum degeneracy is reached and the ^{39}K atoms form an almost pure BEC at the trap center. In the end, we arrive at a BEC that is so pure that the fraction of thermal atoms is below the detection limit.

At this point, a 1D optical lattice is ramped up linearly to 11 recoil energies (E_r) in 100ms. This is slow enough so we don't see any excitations to higher bands even if we go to the deepest lattice potential possible in the setup. The potential is formed by two beams intersecting at 120° at a wavelength of 736.8nm (i.e. blue detuned). The reason for this angle is that the system was built to produce a 2D honeycomb potential, which is generated by interfering three beams intersection at 120° , but only a 1D lattice was used for all the work covered by this thesis, so one beam is always switched off.

The lattice potential's position is modulated periodically in time over an integer number of cycles by modulating the phase of one lattice beam with an AOM³. Finally, after the modulation is over, band-mapping is performed by linearly ramping down the lattice in 0.1ms and absorption imaging is performed by shining a $40\mu\text{s}$ pulse of resonant light on the atoms and comparing the transmission to the case of the same pulse running through the chamber with no atoms.

³Both lattice beams go through AOMs for regulation purposes

3.2 Physical Principles

In this chapter, we briefly describe the most important parts of the experimental setup. We start with the magneto-optical trap, where the atoms are captured in the first place, in section 3.2.1. The principle of optical molasses, the last non-evaporative step of cooling is explained in section 3.2.1. From there we move on to trapping principles, namely the magnetic quadrupole trap and the optical dipole trap in sections 3.2.3 and 3.2.4. Finally, we explain Feshbach resonances in section 3.2.5, a means to control the interactions of the ultra-cold atoms.

3.2.1 Magneto-Optical Trap

The magneto-optical trap (MOT) is the first step in the production of the BEC. Here, atoms are first cooled down and captured. The main idea behind the MOT [7, 211, 216] is Doppler-cooling, where red-detuned light is irradiated along both the positive and negative direction for each dimension onto an atom (though other geometries, e.g. tetrahedral are also possible [217]). This detuning has the effect that absorption increases if the atom moves towards the incident light, Doppler-shifting the light closer to resonance. Combined with isotropic decay back into the lower state, this effectively slows down the atom over many cycles. The fundamental limit for temperatures achievable with this method is defined by the photon scattering rate Γ . Equating the slowing rate with the scattering rate, one finds that the minimum temperature achievable in this way, the so called Doppler-temperature is $T_D = \frac{\hbar\Gamma}{2k_B}$, with k_B the Boltzmann constant, is reached for a detuning $\delta = -\frac{\Gamma}{2}$. For the D2-line of ^{87}Rb , this temperature is $T_D = 146\mu\text{K}$ [218], for the D2-line of ^{39}K it is $T_D = 145\mu\text{K}$ [219].

To keep the atoms from drifting out of the cooling region, a coil pair in anti-Helmholtz configuration produces a magnetic quadrupole field. This quadrupole field has the feature of varying linearly in every dimension at its center. This is used to selectively shift different m_F sub-levels in and out of resonance with the irradiated light via the Zeeman effect [220]. By using opposing circular polarizations (σ^+ and σ^-) for opposing beams of light, the atoms can effectively be pushed into the zero-field center of the coils (see figure 3.2).

3.2.2 Optical Molasses

The next step in the cool down of captured atoms are optical molasses. The polarization-gradient cooling in an optical molasses is a way to cool atoms below the Doppler limit [203, 221]. In this scheme (see figure 3.3), red detuned opposing beams of perpendicular polarization are irradiated onto the cloud of atoms. They interfere to form a pattern where the polarization of the resulting standing wave changes from P to σ^+ to S to σ^+ to P within half a wavelength. As the polarization affects the effective potential of the atoms according to their hyperfine state, see section 3.2.4, a situation can be realized in which atoms have to climb up a potential hill, losing kinetic energy in the process, from

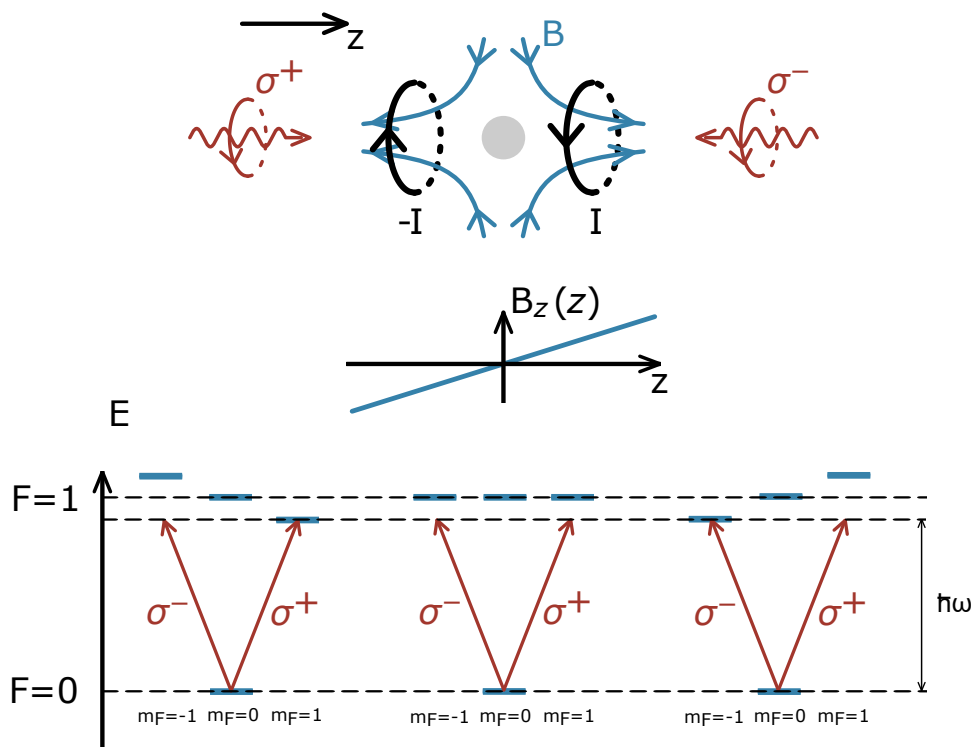


Figure 3.2: Magneto-optical trapping. Top: Simplified scheme of magneto-optical trapping (MOT): A pair of anti-Helmholtz coils (**black**) produces a magnetic quadrupole field (**blue**). Circularly polarized light (**red**) with opposing polarizations shines on the cloud of atoms (**gray**) from opposite directions.

Center: The magnetic field vanishes in the center of the MOT and varies linearly along each coordinate.

Bottom: Depending on an atoms position, its m_F sub-levels are shifted in and out of resonance so the atom always preferably absorbs light pushing it towards the center of the MOT.

where they can be optically pumped into an internal state with lower potential energy. Afterwards, the atom can climb up the next hill and the procedure can be repeated, as long as the atom has enough kinetic energy.

The natural limit for this cooling scheme is the temperature associated with the recoil energy $E_r = \frac{\hbar^2 k^2}{2m} = k_B T_r$, so $T_r = 362\text{nK}$ for ^{87}Rb [218] and $T_r = 418\text{nK}$ for ^{39}K [219].

3.2.3 Magnetic Quadrupole Trap

Magnetic confinement in quadrupole traps is used at many points in the experiment, but they can be summarized in three groups. The first trap is formed by the 3D MOT coils and is switched on as the atoms are spin polarized right after the optical molasses sequence. The second group consists of many pairs of coils in the magnetic transport section. These coils produce a quadrupole field that moves with time, keeping the cloud in its center and moving them from the MOT chamber into the experimental chamber. Here, the last

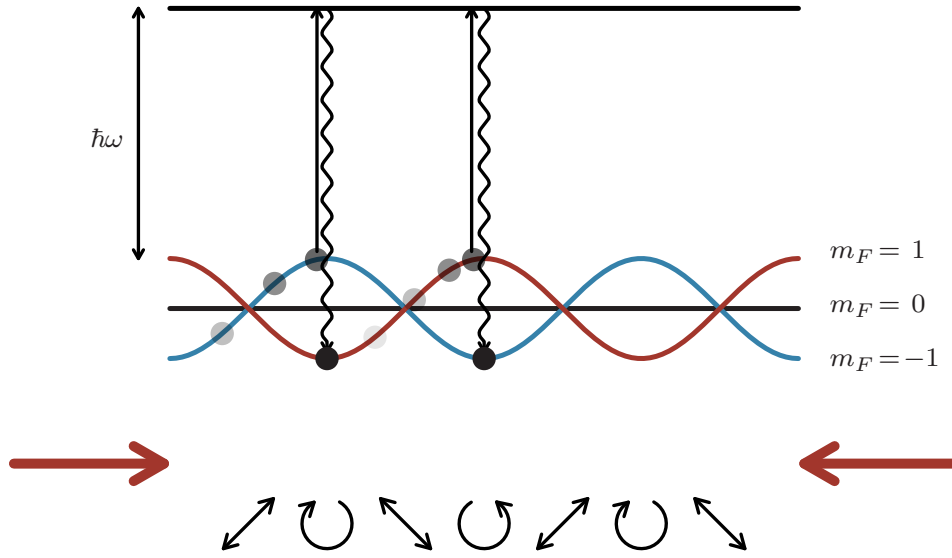


Figure 3.3: Polarization-gradient cooling. Two beams of red detuned light from opposing directions and of perpendicular polarization interfere (**big red arrows**), forming a pattern of alternating (opposing) linear and circular polarized standing waves (**black arrows**). This imposes a light shift on the hyperfine levels of an atom (**red, blue and black line**) with a period of $\frac{\lambda}{2}$. The irradiated light optically pumps the atom from the high-energy state to the low-energy state via an excited state. If the atom still has enough kinetic energy left, it can move over $\frac{\lambda}{4}$ to reach a point where the states are inverted and the process can be repeated.

quadrupole trap confines the atoms while forced evaporative cooling is performed on them.

The principle behind the magnetic quadrupole trap is the Zeeman effect, an energy shift E_Z of atomic hyperfine levels depending on their magnetic quantum number m_F due to a magnetic field with magnetic field $\mathbf{B}(\mathbf{r})$ [220]:

$$E_Z(\mathbf{r}) = \mu_B g_F m_F |\mathbf{B}(\mathbf{r})|, \quad (3.1)$$

with μ_B the Bohr magneton and g_F the Landé factor. This means that for a positive Landé factor, atoms in a hyperfine state with $g_F m_F > 0$ ("weak-field seekers") can be trapped at local minima of magnetic fields, e.g. in the center of magnetic quadrupole fields.

3.2.4 Optical Dipole Trap

After the forced evaporation sequence in the quadrupole trap, the atoms are loaded into an optical dipole trap. Here they are held via the AC-Stark shift [222], where an optical intensity distribution $I(\mathbf{r})$ imposes a dipole potential $U_{\text{dip}}(\mathbf{r})$. For large detunings Δ_{D1} and Δ_{D2} from the D1 and D2 line, i.e. much larger than the hyperfine splitting $\Delta_{D1}, \Delta_{D2} \gg \Delta_{\text{HF}}$, the potential imposed on an alkali-atom can be calculated according to [222]:

$$U_{\text{dip}}(\mathbf{r}) = \frac{\pi c^2}{2} \left(\frac{\Gamma_{D2}}{\omega_{D2}^3} \frac{2 + \mathcal{P} g_F m_F}{\Delta_{D2}} + \frac{\Gamma_{D1}}{\omega_{D1}^3} \frac{1 - \mathcal{P} g_F m_F}{\Delta_{D1}} \right) I(\mathbf{r}), \quad (3.2)$$

with the natural line width Γ , transition frequency ω of the respective line, polarization \mathcal{P} (0 for π - and ± 1 for σ^\pm -polarized light), Landé factor g_F and the magnetic quantum number m_F (of the current ground state). The spatial profile of the light intensity results in an optical potential due to the AC-Stark shift [151, 223]. Because the photon scattering rate scales as $\frac{1}{\Delta^2}$ [222], it is desirable to make the detuning as large as possible, countering a linear decrease in potential depth due to the detuning Δ by an increased beam intensity. In our experiment, we use red-detuned light ($\Delta < 0$) at $\lambda = 1064\text{nm}$ in the dipole trap to create an attractive potential and blue-detuned light ($\Delta > 0$) at $\lambda = 736.8\text{nm}$ in the lattice to obtain a repulsive potential.

The dipole trap is formed by two perpendicular Gaussian beams in the horizontal plane. The intensity profile $I(\mathbf{r})$ of a Gaussian beam along the x -direction can be described by [224]:

$$I(\mathbf{r}) = \frac{2P}{\pi w_y(x) w_z(x)} e^{-2\left(\frac{y^2}{w_y^2(x)} + \frac{z^2}{w_z^2(x)}\right)} \quad (3.3)$$

$$w_i(x) = w_{0,i} \sqrt{1 + \left(\frac{x}{x_{R,i}}\right)^2} \quad (3.4)$$

$$x_{R,i} = \frac{\pi w_{0,i}^2}{\lambda}, \quad (3.5)$$

with P the beam power, $w_y(x)$ and $w_z(x)$ the beam radius in the y - and z -directions where the intensity falls off to $\frac{1}{e^2}$, $w_{0,y}(x)$ and $w_{0,z}(x)$ the smallest beam waist radius in the y - and z -directions and $x_{R,y}$ and $x_{R,z}$ the Rayleigh length in the y - and z -directions. To avoid any unwanted interference between the beams, their polarizations are chosen to be orthogonal and their frequencies are set $\approx 160\text{MHz}$ apart by the AOMs used to regulate their intensity. Their waists are chosen to be $w_{0,x/y} \approx 300\mu\text{m}$ in the horizontal plane and $w_{0,z} \approx 35\mu\text{m}$ in the vertical direction, resulting in a horizontally disk shaped cloud of atoms. Additionally, after the formation of the BEC is completed, we use a third beam along the z -direction called the dimple that is used to increase the horizontal confinement.

3.2.5 Feshbach Resonance

To control the scattering rate of the atoms in the dipole trap, we use a magnetic Feshbach resonance [212], see figure 3.4. It enables us to ensure thermalization in the evaporation sequence and tune the interactions when the experiment is performed.

A Feshbach resonance occurs, when a magnetic field shifts the energies of an open and a closed (bound state) scattering channel into resonance [212, 225]. Tuning an external magnetic field close to a Feshbach resonance, one can adjust the scattering rate a_s in an ultra-cold gas [226–229]:

$$a_s(B) = a_{BG} \left(1 - \frac{\Delta_B}{B - B_0} \right), \quad (3.6)$$

with a_{BG} the background scattering rate, B the magnetic field, Δ_B the width of the resonance, and B_0 the position of the resonance.

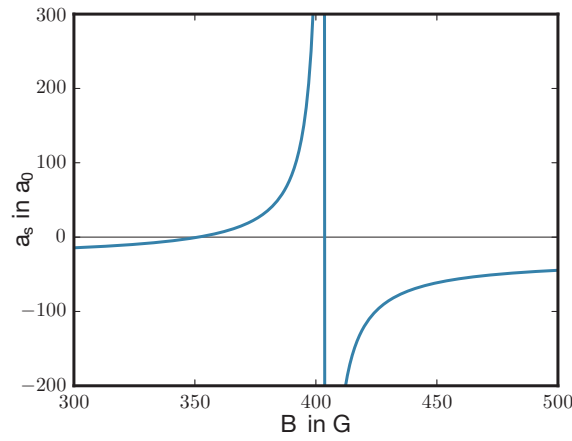


Figure 3.4: Feshbach resonance The Feshbach resonance of ^{39}K - ^{39}K collisions in the ground state is shown. It is described by the equation $a_s = -29a_0 \left(1 + \frac{52\text{G}}{B - 403.4\text{G}} \right)$, with a_0 the Bohr radius [219]. We use this resonance in the experiment, to control the interactions in the BEC.

3.3 1D Lattice

The final step in the preparation of the BEC for the experiment is loading it into an optical 1D lattice. The lattice potential is produced via the AC-Stark effect, just like in the dipole trap. However, the lattice is blue detuned and thus has a deconfining effect on the atoms. In this chapter, we describe how the 1D lattice is formed by two intersecting beams of light in section 3.3.1. We then show how the periodic drive can be implemented via acceleration of the lattice itself in section 3.3.2. Finally, we explain how the population of different momentum-states can be measured with the band-mapping technique in section 3.3.3.

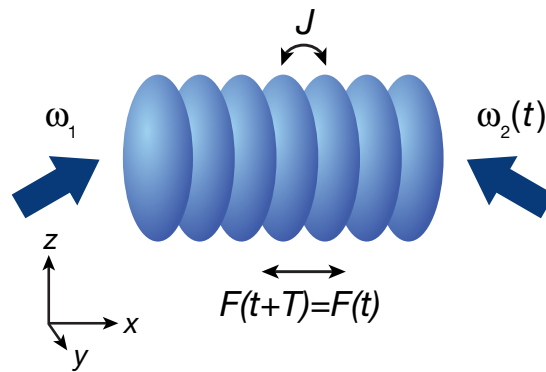


Figure 3.5: Schematic of the driven 1D lattice. Two beams of blue detuned light interfere at an angle of 120° (**blue arrows**). They form a 1D lattice of "pancakes" (**blue ovals**), that are coupled by a tunneling constant J . By periodically varying the frequency $\omega_2(t)$ of one of the beams, an effective periodic force $F(t)$ is applied to the atoms. This figure is adapted from [192].

3.3.1 Lattice Potential

The experiment was originally built to produce a honeycomb lattice [53], so it features three coplanar beams of lattice light at the same frequency and out-of-plane polarization, intersecting each other at 120° . They are produced by splitting the beam of a titanium-sapphire laser (TiSa). To produce the 1D lattice that we used in this work, we switch off one of these beams and end up with a lattice formed by two beams intersecting at 120° with a lattice constant $d = \frac{\pi}{k_L} = \frac{\lambda}{2 \sin(60^\circ)} \approx 425 \text{ nm}$, $\lambda = 736.8 \text{ nm}$ being the laser wavelength. Their waists are $w_{0,z} \approx 100 \mu\text{m}$ in the vertical direction and $w_{0,x/y} \approx 400 \mu\text{m}$ in the horizontal direction which is much larger than the respective extent of the BEC, so they can be modeled as two interfering plane waves:

$$E_1(x, y) = \frac{E_0}{2} \left(e^{i(\omega_1 t - k_x x - k_y y)} + e^{-i(\omega_1 t - k_x x - k_y y)} \right) \quad (3.7)$$

$$E_2(x, y) = \frac{E_0}{2} \left(e^{i(\omega_1 t - \Delta\omega t + k_x x - k_y y)} + e^{-i(\omega_1 t - \Delta\omega t + k_x x - k_y y)} \right) \quad (3.8)$$

$$E(x, y) = E_1(x, y) + E_2(x, y) \quad (3.9)$$

$$I(x, y) = \frac{1}{2} \varepsilon_0 E^2(x, y) \quad (3.10)$$

$$\begin{aligned} &= \frac{E_0^2}{8} \left(e^{i(\omega_1 t - k_x x - k_y y)} + e^{-i(\omega_1 t - k_x x - k_y y)} \right. \\ &\quad \left. + e^{i(\omega_1 t - \Delta\omega t + k_x x - k_y y)} + e^{-i(\omega_1 t - \Delta\omega t + k_x x - k_y y)} \right)^2 \end{aligned} \quad (3.11)$$

$$\begin{aligned} &\stackrel{\text{RWA}}{\approx} \frac{E_0^2}{8} \left(1 + e^{i(-2k_x x + \Delta\omega t)} + 1 + e^{i(2k_x x - \Delta\omega t)} \right. \\ &\quad \left. + e^{i(2k_x x - \Delta\omega t)} + 1 + e^{i(-2k_x x + \Delta\omega t)} + 1 \right) \end{aligned} \quad (3.12)$$

$$= \frac{E_0^2}{2} \left(1 + \frac{e^{i(2k_x x - \Delta\omega t)} + e^{i(-2k_x x + \Delta\omega t)}}{2} \right) \quad (3.13)$$

$$= \frac{E_0^2}{2} \left(1 + \cos(2k_x x - \Delta\omega t) \right) \quad (3.14)$$

$$= \frac{E_0^2}{2} \left(1 + \cos\left(2k_L \cos\left(\frac{\theta}{2}\right) x - \Delta\omega t \right) \right) \quad (3.15)$$

$$I(x, y) = \frac{E_0^2}{2} \left(1 + \cos(k_L x - \Delta\omega t) \right), \quad (3.16)$$

with $E_{1/2}(x, y)$ the electrical field of the two plane waves, ω_1 the frequency of the first beam, $\Delta\omega$ the frequency detuning of the second beam with respect to the first, $(k_x, k_y)^t = (k_L \cos(\frac{\theta}{2}), k_L \sin(\frac{\theta}{2}))^t$ the wave vector (where we neglect the detuning from the beginning, because it will never become significant here) satisfying $\sqrt{k_x^2 + k_y^2} = k_L = \frac{2\pi}{\lambda}$, $I(x, y)$ the overall intensity, ε_0 the vacuum permittivity, "RWA" indicating the rotating wave approximation, and $\theta = 120^\circ$ the angle between the two beams.

3.3.2 Lattice Acceleration

Since the phase velocity of the sinusoidal wave is given by $c_L = \frac{\Delta\omega}{k_L}$, we can produce a standing ($\Delta\omega=0$) or running ($\Delta\omega\neq 0$) wave. We use this feature to periodically drive the BEC. The inertial force $F=ma$, which atoms of mass m will feel in a dragged lattice under acceleration $a=\partial_t c_L$, is:

$$F = m a \quad (3.17)$$

$$= m \partial_t c_L \quad (3.18)$$

$$= m \partial_t \frac{\Delta\omega}{k_L} \quad (3.19)$$

$$= \frac{m}{k_L} \partial_t \Delta\omega \quad (3.20)$$

$$F = m d \partial_t \Delta\nu, \quad (3.21)$$

with the lattice spacing $d = \frac{2\pi}{k_L}$ and $\Delta\nu = \frac{\Delta\omega}{2\pi}$ the frequency offset of the second beam. For a periodic drive of the form $\Delta\nu = \nu_0 \sin(\omega t)$, this evaluates to:

$$F = m d \nu_0 \omega \cos(\omega t) \quad (3.22)$$

$$= F_0 \cos(\omega t) \quad (3.23)$$

$$F_0 = m d \nu_0 \omega \quad (3.24)$$

This force can be used to compute the so called driving amplitude K and the driving strength α :

$$K = F_0 d \quad (3.25)$$

$$= m d^2 \nu_0 \omega \quad (3.26)$$

$$\alpha = \frac{K}{\hbar\omega} \quad (3.27)$$

$$= \frac{m d^2 \nu_0}{\hbar} \quad (3.28)$$

$$= \frac{\hbar \pi^2 \nu_0}{2 E_r}, \quad (3.29)$$

with $E_r = \frac{\hbar^2 k_L^2}{8m}$ the recoil energy. Note that we use the definition of recoil energy derived from the effective lattice constant $\frac{k_L}{2}$ for easy comparison with theoretical models instead of the photonic recoil energy based on the photon wave number k .

3.3.3 Band-Mapping

In order to obtain information about the population of different bands and quasi-momenta, we perform a technique called band-mapping. Here, the atoms are adiabatically transferred to a specific real space momentum state depending on their band and momentum state in the lattice by slowly ramping down the lattice beam power [230, 231]. In order to achieve this, two fundamental limits have to be considered. On one hand, the band-mapping duration has to be long compared to the band gap so populations are adiabatically transferred and no mapping on other free space states takes place. On the other hand, the duration has to be short compared to the tunneling time so no considerable dynamics can take place in the cloud, which might change the population already while still in the lattice⁴. In our setup, the energy gap is 42kHz for $q = 0$ in the $11E_r$ lattice we use in the experiment, corresponding to a timescale of $24\mu\text{s}$ and shrinks to 28kHz, respectively $35\mu\text{s}$ in the limit of $0E_r$. The tunneling rate is 108Hz, corresponding to 9.3ms, so the ramp down duration of the lattice t_{rd} has to satisfy $35\mu\text{s} < t_{\text{rd}} < 9.3\text{ms}$. In our experiment, this ramp down duration was optimized to $t_{\text{rd}} = 100\mu\text{s}$.

⁴This is of course a problem because during the ramp down, the tunneling time goes to zero. However, it still makes sense to think about this limit.

3.4 Imaging

To evaluate the atoms positions, we use absorption imaging [11]. To this means, a beam of resonant light is targeted at the atoms and directed onto a charge-coupled device (CCD), where an image focused on the cloud is taken. By comparing images of the beam with atoms present, casting a shadow on the CCD camera, and without atoms present, it is possible to evaluate the number of atoms projected on each pixel by their scattered light.

We take four images in total: One of the atoms illuminated by the imaging beam, one of the imaging beam without atoms and two dark images that are subtracted from them. The two resulting subtracted images are then used in eq.3.31 to get the column density of atoms.

While for low imaging intensities far below the saturation intensity, the Beer–Lambert law could be used to evaluate the optical column density, due to the high column densities involved, we have to use high saturation imaging and thus need to use a more complex approach [232]:

$$n_{\text{col}}(x, y) = \alpha' \ln \frac{I_i(x, y)}{I_f(x, y)} + \frac{I_i(x, y) - I_f(x, y)}{I_S}, \quad (3.30)$$

for imaging along the z -axis with $n_{\text{col}}(x, y) = \int dz n(x, y, z)$ the column density, α' a dimensionless parameter that usually has to be gauged, $I_i(x, y)$ the intensity without atoms, $I_f(x, y)$ the intensity with atoms and I_S the saturation intensity. While it is tempting to use this equation as it is written down, experimental imperfections block this route. Instead, we use an expression with another degree of freedom in place of the saturation intensity I_S and with $\mathcal{C}(x, y)$ the counts per pixel on the CCD:

$$n_{\text{col}}(x, y) = \alpha \ln \frac{\mathcal{C}_i(x, y)}{\mathcal{C}_f(x, y)} + \beta (\mathcal{C}_i(x, y) - \mathcal{C}_f(x, y)). \quad (3.31)$$

We calibrate the factors α and β on a set of images of BECs with the same atom number taken at different imaging intensities. We then fit the ratio $\gamma = \frac{\alpha}{\beta}$ to minimize the normalized variation of the atom number $N = \int dx \int dy n_{\text{col}}(x, y)$ over the sample with N the average atom number and ΔN^2 its variance: $\gamma = \underset{\gamma}{\text{argmin}} \frac{\Delta N^2}{N}$. The absolute atom number is afterwards calibrated independently (see section 4.2.3).

Measurements

4.1 Dynamical Instabilities

The central part of this work is the measurement and characterization of parametric instabilities. While quantifying loss rates in the BEC directly has proven very fruitful in previous experiments [146], where incoherent processes that lead to a decay of the BEC, described by Fermi's golden rule, were investigated, the depletion is not a good observable for the investigation of these instabilities. On the relevant time scale for the observation of the coherent dynamics in the first few driving cycles, it is too small to directly quantify rates in the same manner as in [146]. The loss rates turn out to be masked by imaging artifacts that arise from the high densities in the BEC. Specifically, we found a breathing mode of the condensate, i.e. a collective mode excitation that modulates density and extension [233, 234]. Because the imaging signal depends on density in a nonlinear way (see chapter 3.4), this leads to a modulation of the integrated pixel counts and in turn appears as atom number fluctuation.

To get past this obstacle, we do not measure the particle loss in the BEC but instead the population of the excited modes directly in momentum space via band-mapping and time of flight (TOF) measurements. While this approach is experimentally more challenging, it provides a lot of additional information compared to the time traces of particle number in the BEC from previous measurements. First of all, as there is no quantitative agreement between theory and observation in the instability rates, a direct measurement is better suited than indirect determination via loss rates in the condensate. Second, our approach allows for the assessment of both the parallel and the perpendicular (with respect to the lattice) component of the instabilities' momentum. This, in turn, allows to directly observe the transition between two regimes, distinguished by a driving frequency above or below the effective Bogoliubov bandwidth.

While it would in principle be desirable to perform the measurement at long TOF to maximally disentangle insitu size and momentum distribution, the diminutive nature of the signal limits the realizable TOF in our case to about 6ms as the number of relevant pixels on the CCD (and thus noise) increases quadratically with TOF. For longer TOF the density in the instability peaks becomes too low.

We cannot quantify the number of atoms per pixel in the excited modes because the calibration is only valid in the very dense condensate. However, because the density is very low in the excited modes, we can assume that the pixel counts there are proportional to the atom number. This means that while we cannot determine the population of each mode, we can determine their exponential growth rates.

We have a clear prediction of what the population the most unstable mode should look like [164], see eqs. 2.161-2.166 in section 2.8.2. In short, we expect the most populated mode to be the one that puts as much energy as possible in the q^x -momentum component. This means that as the driving frequency is increased, all energy that goes from the absorption of two quanta from the drive to into the excitation of two atoms is used to maximize the momentum along the lattice. Only after the BZ edge is reached and there cannot be any more energy stored in momentum along the lattice, perpendicular momenta are

excited. We distinguish regime (I) with a driving frequency below the effective Bogoliubov bandwidth and regime (II) with a driving frequency above the effective Bogoliubov bandwidth, see figure 2.10.

4.1.1 Experimental Sequence

To begin our measurement, we start with a BEC of $(37 \pm 4) \cdot 10^4$ ^{39}K atoms in the dipole trap. We then linearly ramp up the 1D lattice to $11E_r$ in 100ms. Afterwards, we turn on the drive instantly (quench), drive for an integer number of cycles and instantly turn off the drive. The reason we do this is that it is more simple to simulate the dynamics that way and it is not possible to well define the onset of the drive with ramp up. This is not a problem if the BEC depletion is measured for many driving cycles $\gg 1$, but in our case with a ramp up over just 5 cycles, the interesting coherent dynamics would already be over as decoherence/dephasing takes over after a few driving cycles due to interactions between the excitations and the condensate. After turning off the drive we linearly ramp down the lattice in $100\mu\text{s}$ (band-mapping, see chapter 3.4) and image after 6ms of TOF.

We take data sets for two driving amplitudes $\alpha_1 = 1.44$ and $\alpha_2 = 1.78$, with driving frequencies in the range $\omega \in [500\text{Hz}, 900\text{Hz}] \cdot 2\pi$. For each pair of parameters, we vary the driving duration in integer cycles from ≈ 3 to ≈ 13 .

4.1.2 Evaluation of the q_x -Component of the Most Unstable Mode

We select a region of interest (ROI) that is large compared to the first Brillouin zone (BZ) in the x -direction and captures all atoms well in the y -direction, see figure 4.1. This ROI is the same for all images. The resulting set of cut out images is then integrated along the y -direction to get a 1D profile in the x -direction, as shown in figure 4.2. Each integrated profile is convolved with a Gaussian of width $\sigma = 0.04 \frac{\pi}{d}$ (for calibration of the q_x -axis see section 4.2.5). This step is necessary to get rid of the detection noise still present in the profiles so local maxima can be properly determined, which has turned out to work much better than fitting due to the asymmetric shape of the peaks. In the next step, we subtract an inhomogeneous background from the images, that is due to fluctuations in the imaging beam. To first order, these fluctuations imprint a linearly varying offset. It is corrected by averaging the outermost 100 pixels on both the negative and positive momentum side (which is still well outside the first BZ) and defining a linear function through them. This line is subtracted from the whole profile. The last correction performed on the profiles is a shift to center. The position of the BEC varies from shot to shot, mostly due to fluctuations in the pointing of the dipole beams. To properly average over many profiles, we perform a Gaussian fit on the central BEC peak in all profiles for each parameter set and shift them to perfectly coincide in position along the q_x -axis. For each set of parameters, we take ≈ 10 measurements. Taking more data points turned out to be counterproductive due to atom number drifts in the setup on long time scales that limit the total duration of a measurement series.

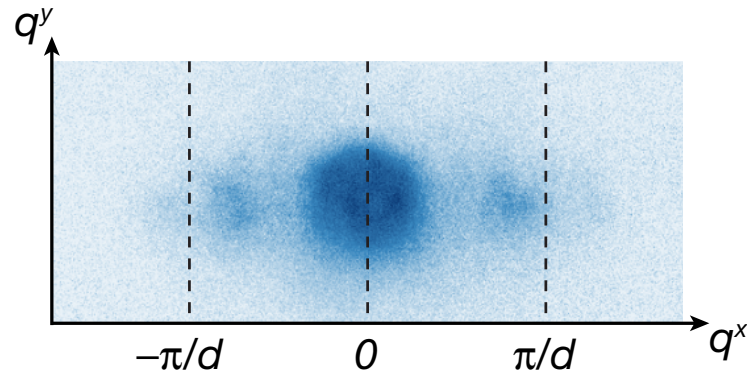


Figure 4.1: Camera Image. The image shows a BEC centered at $q^x = 0$ and instability peaks close to the BZ edge. The cloud was driven for 6 cycles with an amplitude of $\alpha = 1.44$ at a frequency of $\omega = 2\pi \cdot 750\text{Hz}$.

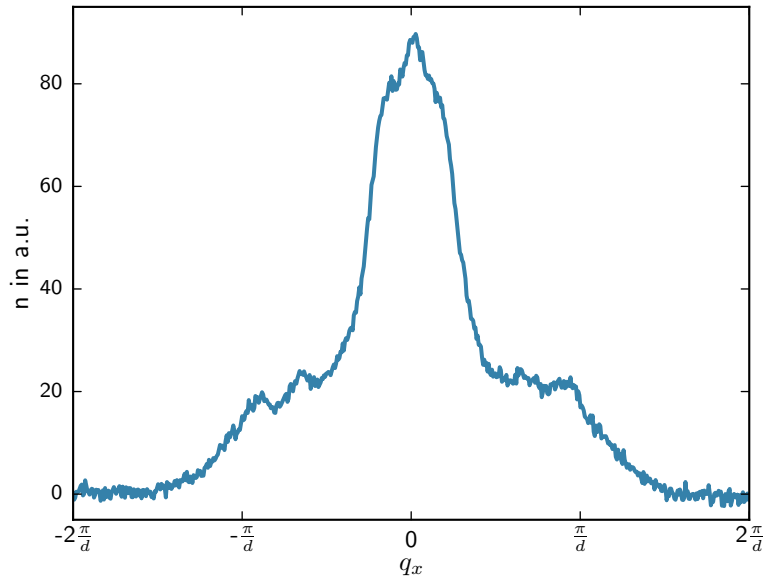


Figure 4.2: Raw q_x -profile. Image of cloud integrated along the y -direction. The cloud was driven for 6 cycles with an amplitude of $\alpha = 1.44$ at a frequency of $\omega = 2\pi \cdot 750\text{Hz}$.

The averaged profile for the initial BEC (shaking duration $t = 0$) $n_0(q)$ is taken as a reference to extract the very small signal of excitations from the background at each shaking duration $t > 0$. Because the depletion of the condensate is $\lesssim 10\%$ on the time scales probed in the experiments, the profile of the BEC does not change very much and can well be approximated to zeroth order as an overall scaling. So, for each profile i in each shaking duration $t > 0$ we scale the initial profile $n_0(q)$ to the same maximum value as $n_{t,i}(q)$ and subtract the two. This leaves the excited side peaks as dominant features of the remaining profiles, see figure 4.3.

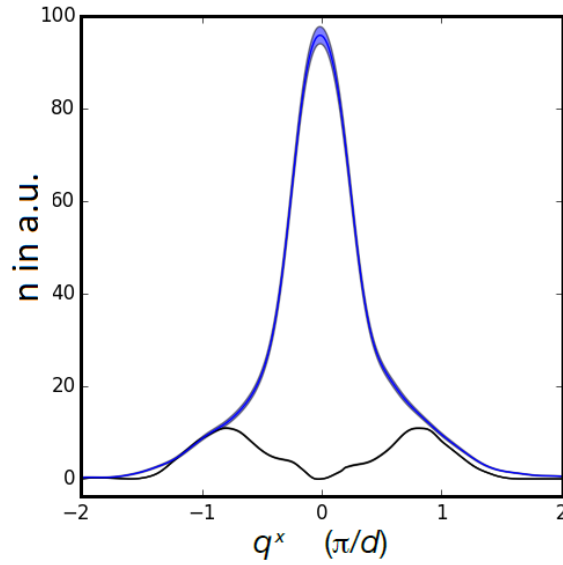


Figure 4.3: Processed q_x -profile. The image of cloud is integrated along the y -direction, averaged over 10 realizations, convolved with a Gaussian and a scaled initial profile for zero shaking duration is subtracted (**black**). The initial profile is shown in **blue** for reference. The cloud was driven for 6 cycles with an amplitude of $\alpha = 1.44$ at a frequency of $\omega = 2\pi \cdot 750\text{Hz}$.

While we could well extract the position of the maximum and average the 10 profiles for each set of parameters, to estimate the error we need to use a bootstrapping approach. This is due to the fact that the peaks do not have a nice Gaussian or similar shape and retain small distortions even after smoothing. From the set of 10 profiles for each set of parameters, we randomly draw 10-combinations with repetition, i.e. we end up with a set of 10 profiles in which a single profile might be repeated arbitrarily often. These 10 sets are then averaged to a single profile $n_{t,j}(q)$ of which we extract the position of the maximum $q_{\max,t,j,\pm}$ on both the negative and the positive momentum side (denoted by \pm) independently. This process is repeated 100 times, so we end up with a set of 100 instances of $q_{\max,t,j,\pm}$. On this set, we compute the average $\bar{q}_{\max,t,\pm}$ and the standard error $\Delta q_{\max,t,\pm}$ as width of the distribution of $q_{\max,t,\pm}$. The average of these effectively 1000 profiles is very close to the average of the original 10, so we do not introduce a relevant error there. The error might be just an estimate, however, it should be close to the correct value.

It should be noted, that due to confinement and interactions, the condensate does have a spread in momentum space. This spread can be modeled with a Gaussian of $\sigma_q = 0.25 \pm 0.05 \frac{\pi}{d}$ in both directions. This is important for two reasons: Firstly, due to its far greater population this means that the condensate still dominates the population of modes at some distance from the BZ center (see figure 4.3) and it is experimentally challenging to investigate low-momentum excitations. Secondly, the finite width of the condensate

masks the width of the resonance even at infinite TOF, so the observed momentum peaks will be wider than the resonance itself.

For driving durations $t \lesssim 9T$, $q_{\max,t,\pm}$ is fairly constant, but for longer durations thermalization processes start to become relevant: Additional momentum components start to be populated and the mode with the largest occupation tends to move towards the center of the BZ. To exclude these data points from our evaluation of the most unstable mode q_{mum} , we define a cutoff criterion as maximum deviation between consecutive maximum positions $q_{\max,t,\pm}$ as $|q_{\max,t,\pm} - q_{\max,t+T,\pm}| < 0.05 \frac{\pi}{d}$. Also, because data points at very short driving durations tend to have very large error bars due to the very low signal to noise ratio at these durations, we define another cutoff criterion for single data points as a maximum error bar of $\Delta q_{\max,t,\pm} < 0.12 \frac{\pi}{d}$. All remaining positions $q_{\max,t,\pm}$ are averaged (taking into account different signs) and finally we arrive at a value for the most unstable mode q_{mum} . Their respective driving durations are considered to make up the "short time regime", in which the position of the maximally populated momentum mode stays constant, see figure 4.4.

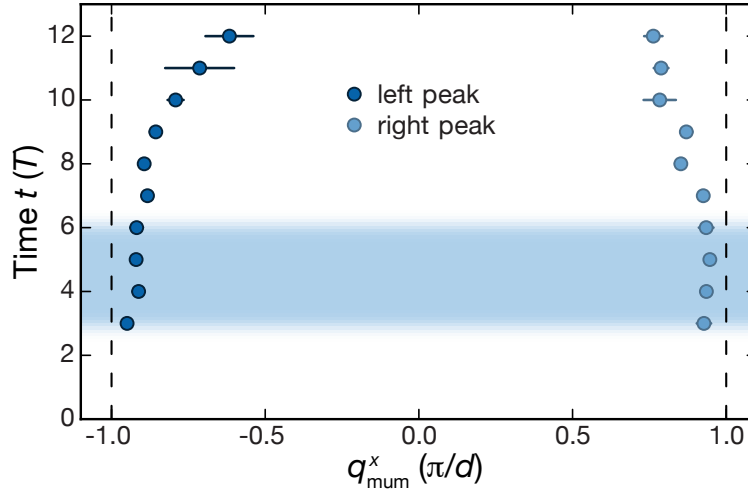


Figure 4.4: Position of most unstable mode q_x^{mum} as a function of modulation duration t for the negative (**dark blue**) and positive (**light blue**) momentum side for $\alpha = 1.78$ and $\omega = 720\text{Hz} \cdot 2\pi$. The **shaded region** indicates the short time regime for this parameter set, that is used in the determination of the properties of the most unstable mode. The **dashed black lines** mark the BZ edges. This figure is adapted from [192].

We evaluate the q_x -profiles at q_{mum} to get the height of the instability peak for all driving durations within the short time regime. Because an exponential growth of the unstable modes is expected, a least squares linear fit is performed through these heights on a logarithmic scale. The slope of this fit is equal to twice the instability rate Γ . The factor of 2 comes from the fact that the instability rate Γ describes the growth of the wave function, but we measure densities which are proportional to the squared absolute value of the wave function.

4.1.3 Evaluation of the q_y -Component of the Most Unstable Mode

As the confinement in the z -direction is approximately an order of magnitude larger than along the other two directions, the dynamics in the xy -plane are expected to be well decoupled from the z -direction and an evaluation of these two momentum components, disregarding the q_z -component seems appropriate. It is expected that the most unstable mode has zero momentum perpendicular to the lattice up to the point where q_x reaches the band edge (see section 2.7.2). From that point on, all additional energy is put into perpendicular momentum. While we cannot resolve distinct peaks for finite momentum in the y -direction, we can still analyze the profiles for signatures of such an effect. To this end, we take the same images of atom column density as for the evaluation of the q_x -component (see section 4.1.2) and choose two ROIs, around the positive and negative momentum peak respectively, excluding the central BEC. We integrate both regions along the x -direction to end up with a profile for q_y . Just like in the case for q_x , we convolve this profile with a Gaussian of width $\sigma = 0.04 \frac{\pi}{d}$ to reduce noise. Again, we take the outermost 100 pixels and use them to construct a linear function to correct for an inhomogeneous background to first order and fit a Gaussian to the profiles that we use to center them. Finally, we average the 10 profiles for each set of parameters and use their standard deviation on each pixel as an error bar. This error bar is then used to construct an outer and inner error profile, which we use to estimate the error of the widths δq_y . The width is evaluated at 80% maximum of the peak. We choose this value as a trade-off between different high noise effects at the top and at the bottom of the peak. At the top, there is a small slope transforming small deviations in height into big deviations in position of the maximum. The closer to the bottom of the peak we get, the bigger the effect of background noise becomes, lowering the signal to noise ratio. Finally, the relative signal is larger at the top, where the overall width is smallest, which elevates the optimum evaluation height above the common 50% level.

4.2 Calibration

Because of little changes in the setup due to drifts and realignment, there are a few parameters that need regular calibration. To make the measurements as precise as possible, we calibrated all relevant parameters at the time the data was taken. The only exception is the magnification factor of the imaging system, which is so stable that it only needs recalibration after changes in the imaging system. The calibration of the Brillouin zone width is necessary to quantitatively evaluate the momentum of all excitations. The measurement of trapping frequencies is used in the determination of atom number, which is in turn used to estimate the interaction parameter g in the cloud.

4.2.1 Magnification Factor

To calibrate the magnification of the imaging systems, we start with a BEC of ^{39}K in the dipole trap and monitor its free fall in the yz -plane (we label all imaging directions via the axis of their imaging beams and call this x -imaging) after switching off the trap. We fit a Gaussian model to the image of the BEC and extract its center of mass position in (y', z') . From the array of position tuples we fit the direction of gravity z (the perpendicular direction is labeled y accordingly) and fix the origin $(0, 0)$ with the position of the BEC at the time of release. Finally, we fit a model of the form:

$$\alpha_x z = \frac{1}{2} g_a t^2, \quad (4.1)$$

with $\alpha_x = (1.699 \pm 0.003) \frac{\mu\text{m}}{\text{px}}$ the magnification (μm per pixel) in x -imaging and $g_a = 9.81 \frac{\text{m}}{\text{s}^2}$ the gravitational acceleration. The same calibration is done in the (x, z) -plane, where the value is $\alpha_y = (1.797 \pm 0.003) \frac{\mu\text{m}}{\text{px}}$.

In the (x, y) -plane, we have to use a different approach, however, since gravity is perpendicular to that plane. Instead, we load the BEC in a 1D lattice and instantly switch off lattice and dipole trap simultaneously, exciting Bragg peaks in the lattice direction at $q = \frac{2\pi\hbar}{d}$, with d the lattice constant. We image the free falling cloud after 3.5ms and extract the Bragg peaks position (x', y') from a Gaussian fit. We use the two positions of the Bragg peaks to find the rotation angle that the camera is turned with respect to the lattice and define the x -direction to be along the lattice (and y to the perpendicular direction) and fix the origin to $(0, 0)$. Finally, we fit the x -position of the Bragg peaks to a model of the form:

$$\alpha_z x = \frac{q}{m_K} t \quad (4.2)$$

$$= \frac{2\pi\hbar}{dm_K} t, \quad (4.3)$$

with α_z the magnification (μm per pixel) in z -imaging fitted to $\alpha_z = (0.466 \pm 0.001) \frac{\mu\text{m}}{\text{px}}$ and m_K the mass of a ^{39}K atom.

4.2.2 Dipole Trapping Frequencies

To calibrate the trapping frequencies, we force harmonic oscillations of the ^{39}K BEC in the dipole trap. This calibration is done right after taking the actual data to ensure that the dipole trap has the same parameters as it had during the experiments. We hold the BEC in the trap and then increase the power of one of the dipole trap beams¹ by a factor 1.5 in 500ms, which adiabatically brings the BEC to a new, slightly different equilibrium position. We then instantly switch it back to the normal value, which leaves the BEC in an excited position in the trap, forcing it into oscillations. A time trace of this oscillation is recorded by imaging the position of the BEC after 10ms TOF. This TOF gives a much better signal than direct imaging of the small insitu oscillations. We fit a damped sinusoidal to the time trace in both directions to get the dipole trapping frequencies $\omega_{\tilde{x}} = (26.5 \pm 0.7) \cdot 2\pi \text{ Hz}$ and $\omega_{\tilde{y}} = (27.0 \pm 0.8) \cdot 2\pi \text{ Hz}$.

To get the trapping frequency $\omega_z = (189 \pm 3) \cdot 2\pi \text{ Hz}$, we perform the same measurement, but image along the x -axis with 15ms TOF.

4.2.3 Atom Number

We can extract the atom number N in the BEC from a Thomas Fermi model. To this end, we need the calibrated trapping frequencies ω_i , at least one Thomas Fermi radius R_i and the scattering length a_s (see eq. 2.82).

To make use of this, we take insitu images of the BEC in z -imaging in the dipole trap for different scattering lengths $a_s = 5 - 160a_0$, with a_0 the Bohr radius, tuning the scattering length with the Feshbach resonance depicted in figure 3.4. We fit a Thomas Fermi profile for each scattering length and extract the Thomas Fermi radii R_x and R_y . Finally, we fit the atom number to both sets of Thomas Fermi radii versus scattering length, see figure 4.5.

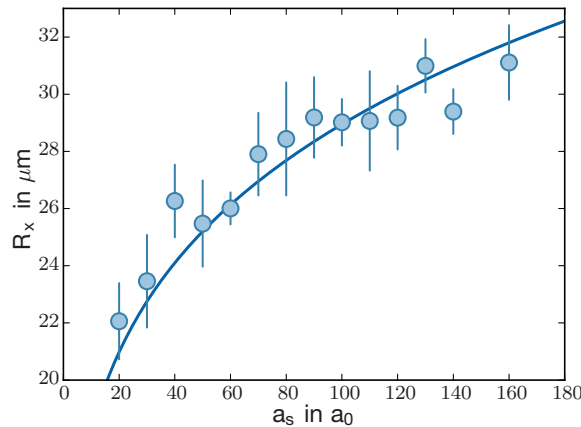


Figure 4.5: Atom number calibration. The Thomas-Fermi radius R_x of the cloud is measured for different scattering lengths a_s . An atom number N_0 is fitted according to a Thomas-Fermi model. The figure shows the Thomas-Fermi radius along the x -direction for $N_0 = 223000 \pm 8000$.

¹The Dipole-X and dipole-Y beams are actually rotated by 38° with respect to the lab frame (x,y,z) .

Because the atom number is not constant in the experiment, but shows variations on both long and short time scales, we calibrate the atom number at the maximum ($N_0 = 506000 \pm 9000$) and minimum ($N_0 = 223000 \pm 8000$) count value measured for the BEC during the time the data was taken. This is necessary because the clouds are very dense and we are imaging in the high saturation regime. This makes the integrated pixel counts on the camera a nonlinear function of atom number. This nonlinearity also means that we can not tell how many atoms we have in the excitations outside the BEC as the density there is very different from the density during calibration. We can however measure the BEC depletion.

4.2.4 Trapping Frequencies in the Presence of the Lattice

Obtaining the trapping frequencies in the presence of the lattice proves to be highly non-trivial because firstly, instead of free space oscillations there are Bloch oscillations along the lattice direction, with their frequency depending on the local potential gradient. Secondly, the oscillations along perpendicular directions turn out to be damped very fast in the presence of the lattice. This means that we can only measure the trapping frequency $\omega_z = (156 \pm 5) \cdot 2\pi$ Hz in the z -direction directly as explained above (section 4.2.2) as it is large enough for us to observe a few complete cycles before all motion is completely damped out. In the (x, y) -plane, however, we can still measure the Thomas Fermi radii very well, just as in the case without a lattice. We then use the calibrated atom number, the trapping frequency in the z -direction and the Thomas Fermi radii in the x - and y -directions to fit a Thomas Fermi model. That way we end up with trapping frequencies $\omega_x = (24.2 \pm 0.8) \cdot 2\pi$ Hz, $\omega_y = (27.6 \pm 0.9) \cdot 2\pi$ Hz and $\omega_z = (156 \pm 5) \cdot 2\pi$ Hz.

4.2.5 Brillouin Zone Width

The width of the Brillouin zone (BZ) is calibrated by adiabatically loading a BEC in the lattice and then instantly switching it off. This excites Bragg peaks in momentum space that we image after 6ms time of flight (same time of flight as used in the characterization of the dynamical instabilities, see chapter 4.1). The peaks are located at the outer edge of the second BZ at $q = \pm \frac{2\pi}{d}$, so their distance is twice the width of the first BZ ($q \in [-\frac{\pi}{d}, \frac{\pi}{d}]$).

Results

5.1 q_x -Component of the Most Unstable Mode

We first take a look at the q_x -component of the most unstable mode, see upper panel in figure 5.1. As expected from a theoretical point of view, q_x increases with increasing driving frequency ω until it matches the bandwidth of the effective Bogoliubov dispersion. At that point no more energy can be deposited into q_x and a further increase of ω will not change the momentum along x .

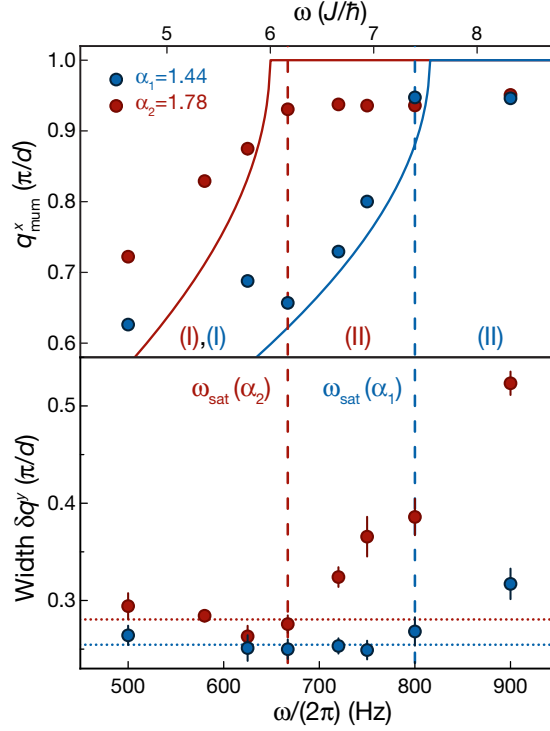


Figure 5.1: Upper panel: Experimental values of the position of the most unstable mode q_{mum}^x for two modulation amplitudes $\alpha_1 = 1.44$ (blue) and $\alpha_2 = 1.78$ (red) with effective hopping $J_{\text{eff},1} = 59 \text{ Hz } \frac{1}{\hbar}$ and $J_{\text{eff},2} = 38 \text{ Hz } \frac{1}{\hbar}$. The **dashed lines** are guides to the eye, indicating the transition between the two regimes at $\omega_{\text{sat}}(\alpha)$. The solid lines display the analytic result based on eq. 2.157 for $g/h = 1300 \text{ Hz}$. Each data point is an average of ≈ 10 independent measurements. The error bars were evaluated based on a bootstrapping approach (see section 4.1.2). **Lower panel:** Full width of the momentum distribution of the excitations δq^y along the y -axis, which was evaluated at 80% of the peak amplitude (see section 4.1.3). The offset $\delta q^y \approx 0.27 \frac{\pi}{d}$ for low frequencies is determined by the width of the condensate both in real and momentum space and the width of the parametric resonance. The **dotted lines** are guides to the eye. Each data point is an average of ≈ 10 independent measurements and the error bars display the corresponding standard deviation. This figure is adapted from [192].

The experimentally determined values of $q_{\text{mum},x}$ saturate considerably before reaching the BZ edge. This can be explained by the combined effect of band-mapping and time of flight imaging. Band-mapping imposes a sharp cut on the momentum distribution at

$q_x = \pm \frac{\pi}{d}$. While $q_x = \pm \frac{\pi}{d}$ can clearly be identified as labeling the same state in the lattice, in free space these two momenta obviously label different states. A momentum peak at $q_x = \pm \frac{\pi}{d}$ has wings on both the positive and negative momentum side of the BZ. These get band-mapped to significantly differing real space momenta. They become two separable momentum distributions, one with a (relatively) sharp edge on the negative side of $q_x = -\frac{\pi}{d}$ and the other with a (relatively) sharp edge on the positive side of $q_x = \frac{\pi}{d}$. The word "relatively" is inserted in brackets here, because during band-mapping the band gap to the next band closes at the BZ edge. This means that the transition to free space dispersion can never be adiabatic here and there will always be excitations into the next band.

These excitations will be band-mapped right next to the BZ edge on the other side, i.e. $\frac{2\pi}{d}$ will be added on the negative momentum side and $\frac{2\pi}{d}$ will be subtracted on the positive momentum side. The result is schematically shown in figure 5.2. It models the number of atoms in the next band in the simplest possible way: Adiabaticity is maximally broken at the band edge, where the bands eventually touch. Here, half of all atoms should be excited because firstly, the difference between the $q = \pm \frac{\pi}{d}$ states in both bands vanishes, and secondly, this is the only way to continuously model the distribution at $q = \pm \frac{\pi}{d}$. From $|q| = \frac{\pi}{d}$ to lower momentum values, the amount of atoms excited to the next band is modeled to decay linearly, down to zero at some finite momentum. Because for a vanishing lattice the gap between the two bands increases linearly with distance from the Brillouin zone edge, this seems like a good approximation in the vicinity of $|q| = \frac{\pi}{d}$. This effect will move the center of both momentum peaks towards zero, keeping the mean of zero $\bar{q}_x = 0$ untouched but shifting the mean of the absolute momentum $|\bar{q}_x| < \frac{\pi}{d}$.

Furthermore, time of flight imaging imposes a transformation on the cloud that closely resembles a convolution of in situ distribution and momentum distribution (multiplied by $\frac{t}{m_k}$), which is also shown in figure 5.2. This has a broadening effect on the measured peaks, but has little impact on the position of the peaks.

It should be noted that there is a significant discrepancy between the interaction parameter $g/h = (870 \pm 30)$ Hz, that is estimated from our Thomas-Fermi model, and the interaction parameter $g/h = 1300$ Hz used to produce the guides to the eye in figure 5.1. These interaction parameters lead to a discrepancy of about 20% between the expected and measured saturation frequencies. This offset might in principle be explained by a systematic error of about 30% in our calibrated atom number. However, we expect this error to be below 20%. Moreover, we believe that there might additional effects induced by the 3D trap that are not properly captured by the 1D simulations.

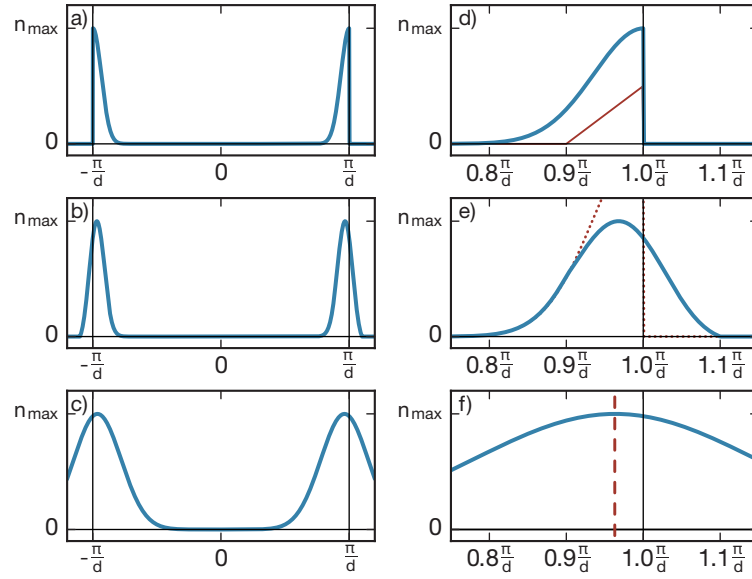


Figure 5.2: Band-mapping and finite time of flight. The effect of band-mapping and finite time of flight on the position of the momentum distribution's maximum is shown schematically. Panel **a)** shows the initial momentum distribution of the excitations in the lattice. **b)** During band-mapping, modes in the next band are populated. Because closer to the BZ edge more atoms are excited, the maximum of the distribution is shifted to lower momenta. **c)** After the short time of flight used in the experiment, the momentum distribution is effectively convolved with the insitu size of the cloud. Panels **d)**, **e)** and **f)** show the same distributions as **a)**, **b)** and **c)**, respectively.

The simple model used for this scheme is indicated in panel **d)**: Because the band gap is closed at $q = \frac{\pi}{d}$ and in order to avoid discontinuity, 50% of atoms at the band edge have to be excited to the next band. As the gap between the two bands now increases linearly with distance from the BZ edge, the most simple model possible is to assume the amount of atoms excited to the higher band decreases linearly down to 0 at some arbitrary momentum q . The **thin red line** indicates the fraction of atoms excited to the higher band. The **dotted red line** in panel **e)** indicates the momentum distribution without excitations and the **dashed red line** in panel **f)** marks the maximum of the momentum distribution after convolution with the insitu shape of the cloud.

5.2 q_y -Component of the Most Unstable Mode

The behavior of the q_y -component of the most unstable mode is also consistent with theoretical expectations (see section 2.8.2 and figure 2.10), see lower panel in figure 5.1. We cannot experimentally resolve a splitting into two distinct peaks in q_y , so we have to settle for evaluating the width of the peak δq_y (see figure 5.3). We can see that this width stays constant with increasing frequency until the q_x -component saturates. At that point, excess energy is transferred into q_y and the peak supposedly splits into two still overlapping peaks

at a finite momentum $|q_y| > 0$. This is reflected in the data as an increase in the measured width of the single visible peak, as shown exemplary in figure 5.3.

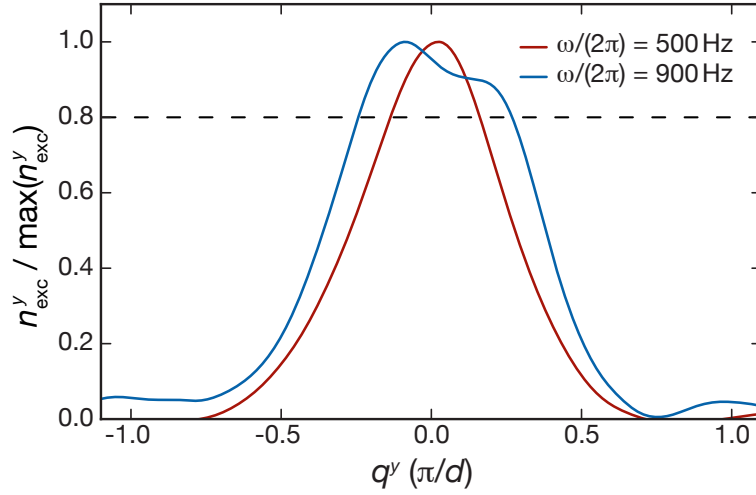


Figure 5.3: Mean integrated momentum distribution of the atoms **perpendicular** to the lattice for one driving frequency (500Hz, **red**) within regime (I) and one driving frequency (900Hz, **blue**) within regime (II). The **dashed black line** indicates the evaluation height (see figure 5.1). This figure is adapted from [192].

5.3 Instability Rate

We also evaluate the growth of the most unstable mode q_{mum} over time. To this end, we track the amplitude of the density profile along q_x at q_{mum} as described above. We confine the evaluation to the short time regime as determined in section 4.1.2.

Comparing the extracted instability rates to the rates produced by a Floquet Fermi's Golden rule (FFGR) and a Bogoliubov-de Gennes (BdG) calculation (see figure 5.4), we find that our results are almost two orders of magnitude larger than expected from FFGR. We interpret this as a clear sign that the dynamics is different from an FFGR description, which well describes the long term decay of the condensate as an incoherent process. At the same time, our results are almost an order of magnitude below the coherent BdG rates. This is hard to justify quantitatively without further theoretical modeling, but might be a hint that we are not probing the system on time scales short enough to extract the pure initial instability rate before terms neglected in the theoretical models become relevant, even though coherent processes are still playing the dominant role.

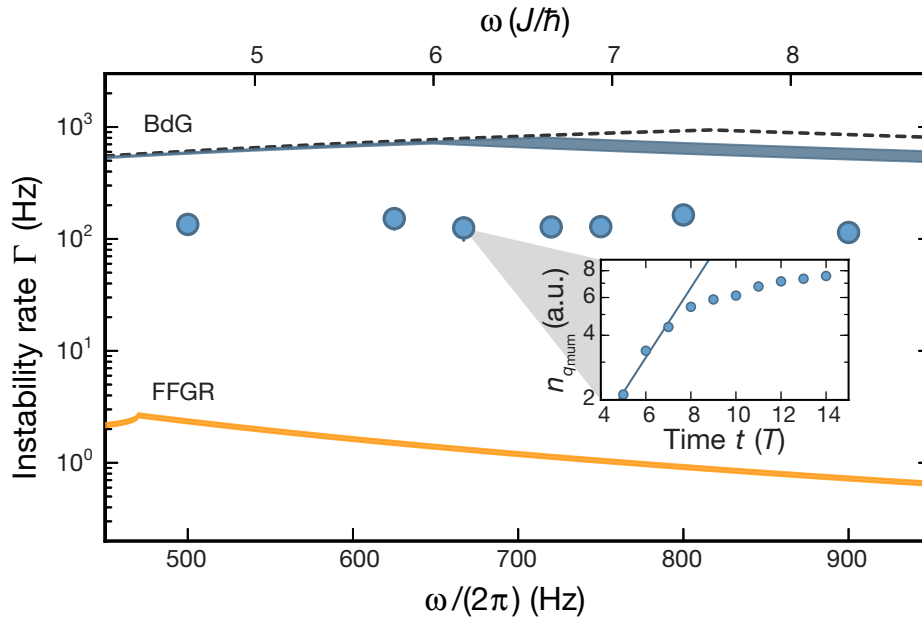


Figure 5.4: Instability rates extracted from the measured populations $n_{q_{\text{mum}}}$ of the most unstable mode for $\alpha = 1.44$ as displayed in figure 5.1. Each data point is obtained from ≈ 10 individual data sets. The error bars are evaluated based on a bootstrapping approach (see section 4.1.2) and are generally smaller than the data points. The **black dashed line** shows the result obtained from the BdG equations for $g/h = 1300$ Hz and the **blue shaded area** the ones obtained for $g/h = (870 \pm 30)$ (see eqs. 2.163 and 2.166), where the width reflects the uncertainty in the atom number calibration. **Orange shaded area**: rates expected from an FFGR approach (see section 2.6.6) for the same parameters. Its width is also determined by the experimental error in the atom number calibration. **Inset**: Measured populations for $\omega = 667 \text{ Hz} \cdot 2\pi$ and exponential fit used to extract the instability rate (**solid line**). This figure is adapted from [192].

5.4 Benchmarking the Bogoliubov-de Gennes Model

To investigate how well the BdG model is suited for the quantitative prediction of growth rates in our system, we compare the predicted time-evolution of the most unstable mode to the prediction of two other models, the weak coupling conserving approximation (WCCA) and the truncated Wigner approximation (TWA). Both models restore the $U(1)$ -symmetry associated with particle number conservation and are thus well suited for an estimation of the point where the BdG description ceases to be exact. A description of these two models can be found in appendix H and I respectively. As shown in figure 5.5, the BdG description coincides well with the other models in the short time regime, where we evaluate the growth rates. The coincidence increases for larger values of g (not shown). The simulations were performed by Marin Bukov at the University of California.

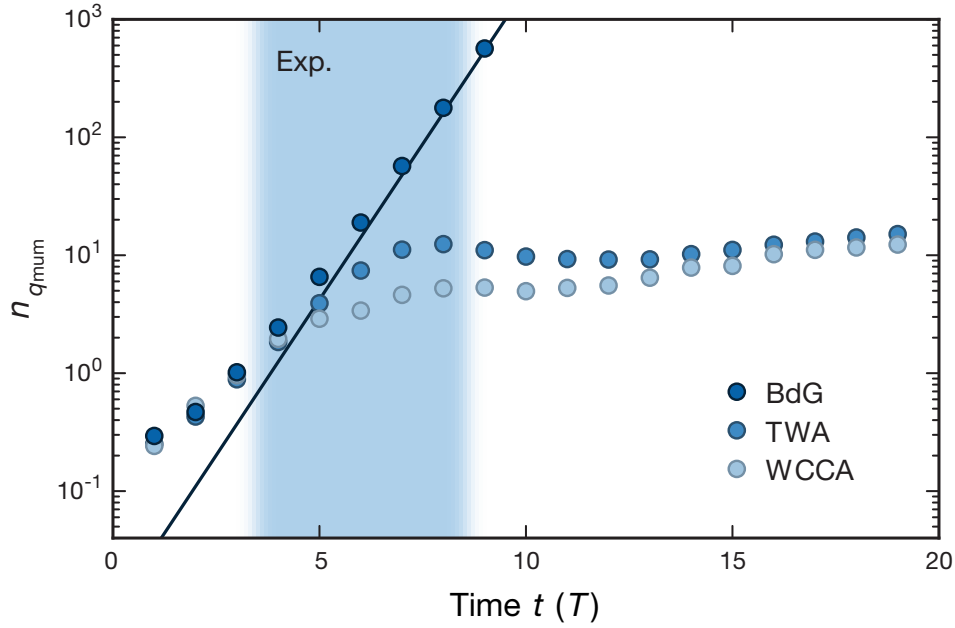


Figure 5.5: Numerical simulations of the occupation of the most unstable mode $n_{q_{\text{mum}}}$ for a homogeneous 2D system (1D lattice and one continuous direction) for $g = 9.52 J$, $\omega = 9.25 \frac{J}{\hbar}$ and $\alpha = 1.44$. The **solid line** displays the rate obtained from the analytic formulas (eqs. H.3-H.5), which is in agreement with the BdG simulations (**dark blue**) for $t \gtrsim 5T$. The TWA (**blue**) and WCCA (**light blue**) partially capture additional non-linear effects and thermalization dynamics, which result in a time-dependent instability rate. **Blue shaded area**: Experimentally accessible time window. This figure is adapted from [192].

5.5 Effect of Harmonic Confinement

If we take a closer look at the saturation point and the dependency of the q_x -component of the most unstable mode on driving frequency, we can clearly see that it does not reflect the effective driven band structure for an interaction parameter g as we would calculate it from the determined Thomas Fermi profiles. We attribute this effect to the harmonic confinement. Due to the confinement, the interaction parameter g becomes position dependent, varying from zero at the edge of the cloud to g_{max} in the center. While it seems reasonable to use the average \bar{g} to calculate the effective bandwidth, we find g_{max} to better reflect the experimental results (see section 5.6.2 for the calculation of \bar{g}). We believe the reason for this behavior lies in the exponential nature of the parametric resonance. While there are many atoms sitting at an effective $g < g_{\text{max}}$, the highest instability rate is found in the center for $g = g_{\text{max}}$ and the excitations arising there quickly dominate other modes growing with smaller rates.

A second effect induced by the harmonic confinement is the absence of a stable regime. While in a 1D system, there are no modes located in regime (II) as it is per definition in the band gap, this is not the case in a trapped system. The presence of the trap breaks

discrete translational symmetry and gives rise to Tamm surface states (modes located at both sides of the trap) [235, 236], see figure 5.6. These modes render the system unstable even above the band edge (see figure 5.7). This means that if one desires to suppress the growth of parasitic modes to increase the lifetime of a driven BEC by constricting its density of states with a 3D lattice in a way so the driving frequency falls within the band gap, instabilities will still arise if the system is harmonically trapped. Because the overlap of these Tamm states with the BEC decreases with energy, instability rate also decreases with driving frequency. Thus, there might still be a regime, where the system is stable for the duration of an experiment. The simulations were performed by Marin Bukov at the University of California.

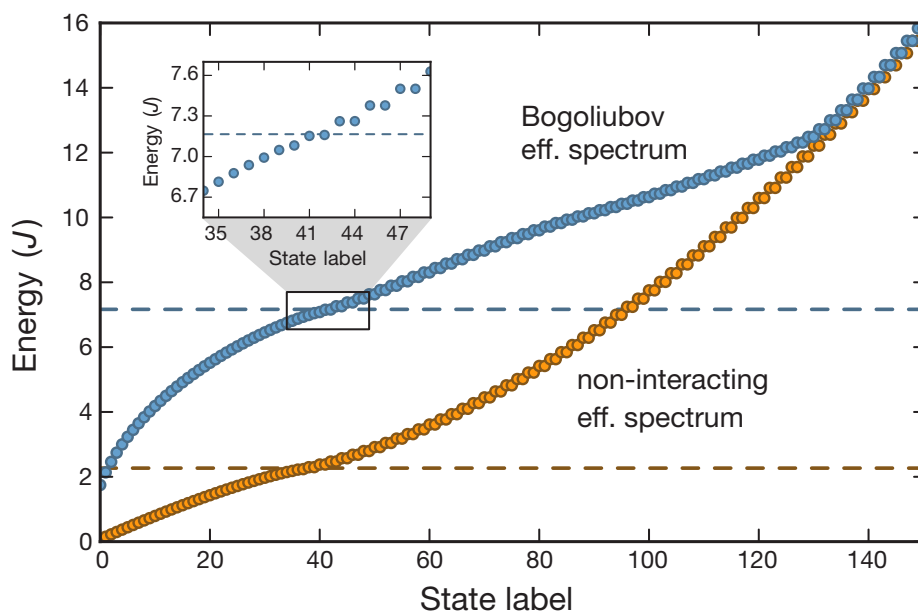


Figure 5.6: Energy spectrum of the non-interacting time-averaged Hamiltonian (**orange dots**) and corresponding effective Bogoliubov dispersion (**blue dots**) in a harmonic trap with $\omega_x = 0.26 \frac{J}{\hbar}$. The **dashed lines** indicate the respective bandwidths in the homogeneous case. **Inset:** As the energy reaches the homogeneous bandwidth, the spectrum becomes quasi-degenerate. The simulations were performed by Marin Bukov at the University of California. This figure is adapted from [192].

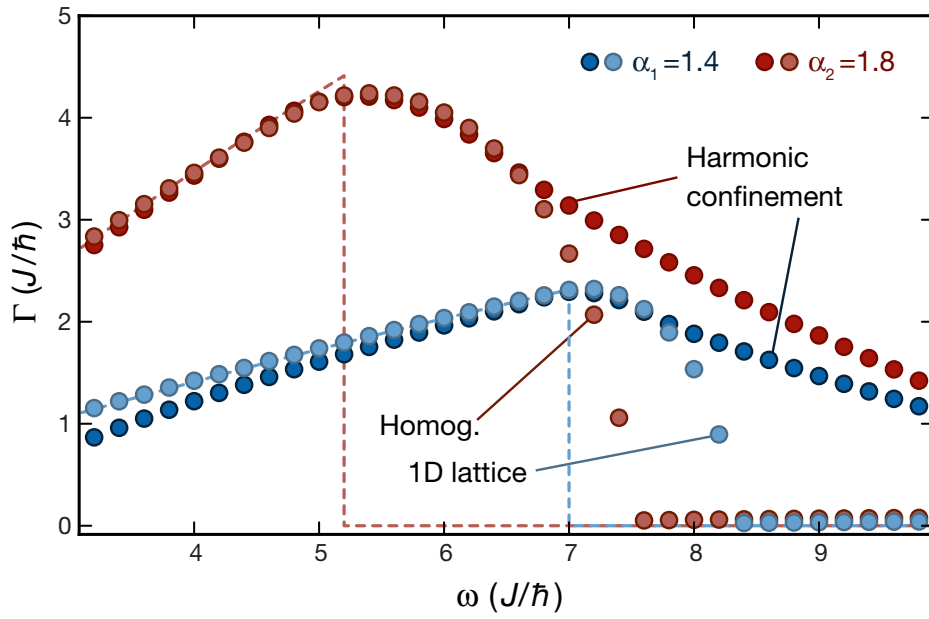


Figure 5.7: Numerical simulations of the instability rate in a homogeneous 1D lattice (**light red** and **light blue**, $g = 10.2 J$) in comparison with the rates in 1D lattices with harmonic confinement (**dark red** and **dark blue**, $\omega_x = 0.26 \frac{J}{\hbar}$ and $g_{\max} = 10.2 J$) for two different driving parameters $\alpha_1 = 1.44$ (**blue**) and $\alpha_2 = 1.78$ (**red**). The system parameters are the same as for the simulations in figure 5.8, i.e. $L_x = 201 d$ and $N_0 = 1000$. The instability rate was extracted from an exponential fit to the numerical data from the last five out of twenty-four driving cycles of evolution. **The dashed lines** show the BdG predictions according to eqs. 2.163 and 2.166 for $g = 10.2 J$. The simulations were performed by Marin Bukov at the University of California. This figure is adapted from [192].

5.6 Interaction Parameter g

A very important part of the main project was understanding that a mapping of the simulated 1D and 2D systems' Hamiltonian onto the experimental 3D system cannot be done in a way that allows for quantitative predictions regarding e.g. lifetimes. The considerations leading to this observation are presented in this chapter.

5.6.1 Definition of g

We recall the interaction part \hat{H}_{int} of Hamiltonian 2.38:

$$\hat{H}_{\text{int}} = \frac{1}{2} U_0 \int d\mathbf{r} \hat{\psi}^\dagger(\mathbf{r}) \hat{\psi}^\dagger(\mathbf{r}) \hat{\psi}(\mathbf{r}) \hat{\psi}(\mathbf{r}),$$

where the interaction parameter U_0 depends only on the dimensionality of the system (e.g. $U_{0,3D} = \frac{4\pi\hbar^2 a_s}{m_K}$) and can be calculated from s-wave scattering theory [147]. Decomposing $\hat{\psi}(\mathbf{r}) := \psi(\mathbf{r}) \hat{a}$ into the wave-function $\psi(\mathbf{r})$ and the annihilation operator \hat{a} , this yields:

$$\hat{H}_{\text{int}} = \frac{1}{2} U_0 \hat{a}^\dagger \hat{a}^\dagger \hat{a} \hat{a} \int d\mathbf{r} |\psi(\mathbf{r})|^4 \quad (5.1)$$

$$= \frac{1}{2} U_0 (\hat{n}^2 - \hat{n}) \int d\mathbf{r} |\psi(\mathbf{r})|^4 \quad (5.2)$$

$$\approx \frac{1}{2} U_0 \hat{n}^2 \int d\mathbf{r} |\psi(\mathbf{r})|^4 \quad (5.3)$$

$$\approx \frac{1}{2} \int d\mathbf{r} \int d\mathbf{r} U_0 \langle \hat{n} \rangle^2 |\psi(\mathbf{r})|^4 \quad (5.4)$$

$$\approx \frac{1}{2} \int d\mathbf{r} U_0 n(\mathbf{r})^2 \quad (5.5)$$

$$\hat{H}_{\text{int}} \approx \frac{1}{2} \int d\mathbf{r} g(\mathbf{r}) n(\mathbf{r}), \quad (5.6)$$

with the particle density density $n(\mathbf{r}) := \langle \hat{n} \rangle |\psi(\mathbf{r})|^2$, the expectation value $\langle \cdot \rangle$ and the interaction parameter $g(\mathbf{r}) := U_0 n(\mathbf{r})$. Note the particle number $\langle \hat{n} \rangle \equiv N_0$.

5.6.2 \bar{g} vs. g_{\max}

The average \bar{y} of a variable $y(\mathbf{r})$ over any distribution $x(\mathbf{r})$ is:

$$\bar{y} := \frac{\int d\mathbf{r} y(\mathbf{r}) x(\mathbf{r})}{\int d\mathbf{r} x(\mathbf{r})}, \quad (5.7)$$

so it is reasonable to assume that a proper simplification of the Hamiltonian is produced by the extension:

$$\hat{H}_{\text{int}} \approx \frac{1}{2} \int d\mathbf{r} g(\mathbf{r}) n(\mathbf{r}) \quad (5.8)$$

$$\approx \frac{1}{2} \left(\int d\mathbf{r} g(\mathbf{r}) n(\mathbf{r}) \right) \frac{\int d\mathbf{r} n(\mathbf{r})}{\int d\mathbf{r} n(\mathbf{r})} \quad (5.9)$$

$$\approx \frac{1}{2} \frac{\int d\mathbf{r} g(\mathbf{r}) n(\mathbf{r})}{\int d\mathbf{r} n(\mathbf{r})} \int d\mathbf{r} n(\mathbf{r}) \quad (5.10)$$

$$\hat{H}_{\text{int}} \approx \frac{1}{2} \bar{g} N. \quad (5.11)$$

However, we find that in the case of the parametric resonance the system is better described by the maximum value $g_{\max} := \max_{\mathbf{r}} g(\mathbf{r})$, see figure 5.8. We attribute this to the fact that the parametric instability gives rise to exponential growth in the observed modes. Because the associated growth rate is bigger for bigger values of g , modes excited at the center of the cloud where $g(\mathbf{r}) = g_{\max}$ quickly dominate the dynamics.

5.6.3 Difference 2D - 3D

The big problem in converting from a true 2D system to a true 3D system is the scattering parameter U . While it is sensible to write:

$$U_{\perp} = U_{3D} w_{0I}, \quad (5.12)$$

which gives U_{\perp} the same dimension as U_{2D} , the two cannot be treated as equal. An insightful way to look at this problem is by taking a look at a diverging lattice depth, which effectively compresses the atoms on site to a true 2D system. This also makes w_{0I} diverge and thus also U_{\perp} . This contradiction can only be resolved by taking into account the dynamics in the third dimension, which is still there for any true 3D system, even if it is trivial and does not explicitly show up in the Hamiltonian.

This means that 2D simulations cannot make a quantitative prediction of the instability rates in the experiment.

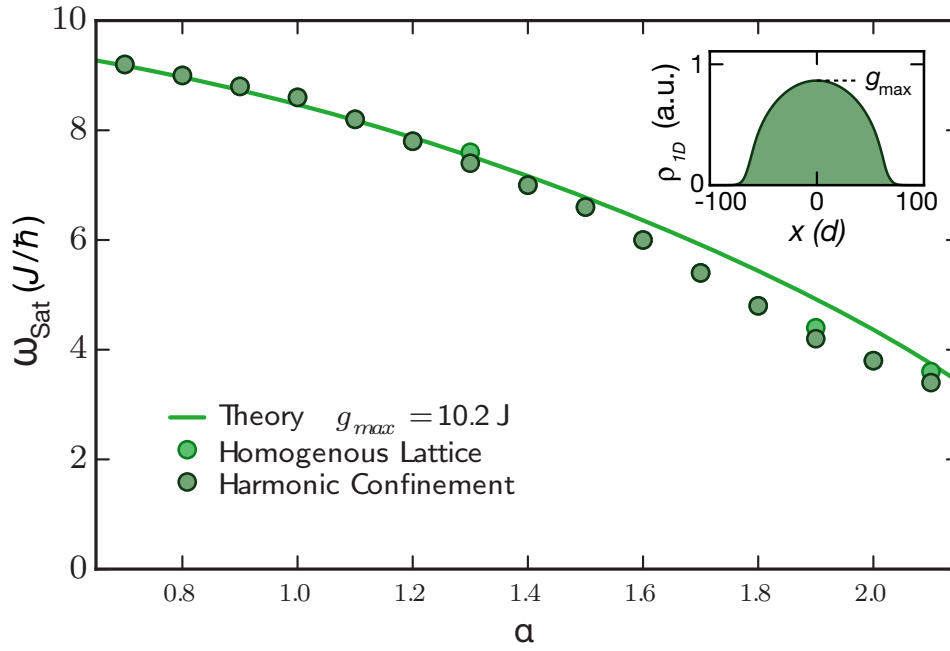


Figure 5.8: Numerical simulations of the saturation frequency ω_{sat} for a homogeneous 1D system (light green, $g = 10.2 J$) and for a harmonically trapped one (dark green, trap frequency $\omega_x = 0.26 \frac{J}{\hbar}$, $g_{\text{max}} = 10.2 J$). The system size is $L_x = 201d$ and the atom number is $N_0 = 1000$. The **solid line is the analytic prediction of the saturation frequency as $\hbar\omega_{\text{sat}} = W_{\text{eff}}$ with the effective bandwidth W_{eff} for a homogeneous 1D lattice with interaction energies g and g_{max} based on eq. 2.157. **Inset:** Initial density distribution $\rho_{1D}(x)$ in the harmonically trapped 1D lattice, which is well described by a Thomas-Fermi profile. It induces a position dependence in the interaction parameter g , where the maximum value g_{max} is determined by the central density. This figure is adapted from [192]. The simulations were performed by Marin Bukov at the University of California.**

Conclusion and Outlook

In conclusion, we have found strong evidence for the appearance of parametric instabilities after few driving cycles in periodically-driven BECs in a 1D optical lattice. These parametric instabilities are responsible for the depletion at the early stage of the driving. We have investigated both the q_x - and q_y -component of the instabilities' momentum in time-of-flight measurements and found that the dynamics is dominated by the most unstable mode, as predicted [164]. In the evaluation of the q_x -component, we found that it increases with driving frequency, until it reaches the band edge. At that point, excess energy is transferred to the q_y -component, which manifests in a broadening of the momentum distribution in that direction. That way, we unveiled the destructive role of the transverse degrees of freedom for the lifetime of the BEC, as it is reasonable to assume that the coherent exponential growth of instabilities at the early stages of the driving is linked to heating at later stages. Also, numerical simulations revealed that a broken discrete translational symmetry, as in our case mediated by harmonic confinement, leads to unstable modes in energy ranges, where the density of states vanishes in the homogeneous lattice. This leads to a depletion of the BEC in naively stable frequency ranges. This has large implications for experiments, as harmonically confined atomic clouds are used in many setups. Parametric resonances are expected to occur whenever the BdG equations of motion feature time-periodic driving, indicating that full-lattice systems without harmonic confinement are necessary to find true stable parameter regimes for periodically-driven systems, such as super-fluids and superconductors [237] and photonic devices [238, 239]. The growth rates of the maximum unstable mode lies more than an order of magnitude above the depletion rates predicted by a Floquet Fermi's Golden rule estimation, which also hints at different mechanisms being at work. We attribute the overestimation of the growth rate by Bogoliubov theory to a rapid saturation happening in the experimentally not accessible time period of the very first < 5 driving cycles, leading to non-linear corrections. This effect can be described by more evolved theories, like the truncated Wigner approximation or the weak-coupling conserving approximation, which take into account the coupling of the excitations to the condensate and are in principle capable of capturing the dynamics beyond the low depletion limit, as they conserve particle number.

The logical next step at our setup would be to investigate heating in the hexagonal lattice and look for possibilities to suppress heating even in the harmonically trapped periodically-driven gas. A possible route to this goal might be the utilization of the additional vertical lattice that has already been built into the setup. If lifetimes of more than a few ms can be achieved, it might be possible to realize an interaction-driven transition into a Mott insulating phase in the honeycomb lattice [94]. Also, producing artificial gauge fields in the p-bands of the honeycomb lattice, it might be possible to realize fractional quantum Hall states [240] that feature anyonic excitations [241]. The exotic properties of anyons are considered for the realization of a topological quantum computer that is resistant to external perturbations [242].

A different experimental route that can be taken is the realization of the optical flux lattice, which yields narrow energy bands with non-zero Chern number without Floquet-engineering [243, 244]. In these bands, strong correlation phenomena related to the fractional quantum Hall effect might be studied.

Finally, another way towards the generation of artificial gauge fields is strained graphene [245–248], which emulates magnetic fields and can be realized by non-isotropic tunneling in a static honeycomb lattice [249]. These magnetic fields can be probed using Bragg-spectroscopy [250] to identify Landau levels in band gaps opening at the Dirac points.

Appendix

Band Structure

A.1 Proof of Bloch's Theorem

Bloch's theorem can be easily proven by choosing a Fourier series ansatz for the eigenfunctions $\psi(x)$, with the normalization factor $\frac{1}{\sqrt{\mathcal{N}}}$ [154]:

$$\psi(x) = \frac{1}{\sqrt{\mathcal{N}}} \sum_k c_k e^{ikx} \quad (\text{A.1})$$

$$\hat{H} \psi(x) = \varepsilon \psi(x) \quad (\text{A.2})$$

$$\frac{1}{\sqrt{\mathcal{N}}} \left(\frac{-\hbar^2}{2m} \partial_x^2 + \sum_j V_j e^{i(jG)x} \right) \sum_k c_k e^{ikx} = \varepsilon \frac{1}{\sqrt{\mathcal{N}}} \sum_k c_k e^{ikx} \quad (\text{A.3})$$

$$\sum_k \left(c_k \frac{\hbar^2 k^2}{2m} e^{ikx} \right) + \sum_{k,j} (c_k V_j e^{i(k+jG)x}) = \varepsilon \sum_k c_k e^{ikx} \quad (\text{A.4})$$

$$\sum_k \left(c_k \frac{\hbar^2 k^2}{2m} e^{ikx} \right) + \sum_{k',j} (c_{k'-jG} V_j e^{ik'x}) = \varepsilon \sum_k c_k e^{ikx} \quad (\text{A.5})$$

$$\sum_k \left(c_k \left(\frac{\hbar^2 k^2}{2m} - \varepsilon \right) e^{ikx} + \sum_j (c_{k-jG} V_j e^{ikx}) \right) = 0 \quad (\text{A.6})$$

$$\sum_k \left(c_k \left(\frac{\hbar^2 k^2}{2m} - \varepsilon \right) + \sum_j (c_{k-jG} V_j) \right) e^{ikx} = 0 \quad (\text{A.7})$$

$$c_k \left(\frac{\hbar^2 k^2}{2m} - \varepsilon \right) + \sum_j (c_{k-jG} V_j) = 0, \quad (\text{A.8})$$

where from eq. A.4 to eq. A.5 we substitute $k+jG=k'$ and from eq. A.5 to eq. A.6 we relabel $k'=k$. Because eq. A.7 has to hold for all x and the exponentials e^{ikx} form an orthonormal basis, all terms have to be equal to zero. From eq. A.8 we can see that all constants c_k , that are separated by multiples of the lattice constant G , form a common system of countably infinitely many equations, which can be solved numerically, yielding infinitely many solutions, that can be grouped (for different k) in bands of increasing energy ε , labeled by n (this is done explicitly for the case of a sinusoidal lattice in section 2.2.2). Constants $c_{n,k}$ whose k are not separated by multiples of G do not depend on

each other and belong to different states. After solving for the constants $c_{n,k}$, we can write the eigenstates $\psi_{n,k}(x)$ as:

$$\psi_{n,k}(x) = \frac{1}{\sqrt{\mathcal{N}}} \sum_j c_{n,k+jG} e^{i(k+jG)x} \quad (\text{A.9})$$

$$\psi_{n,k}(x) = \left(\frac{1}{\sqrt{\mathcal{N}}} \sum_j c_{n,k+jG} e^{ijGx} \right) e^{ikx} := u_{n,k}(x) e^{ikx} \quad (\text{A.10})$$

From eg. A.9 we can see, that states $\psi_{n,k}(x)$, with wave numbers k that differ by multiples of G , are equal as they correspond to a different labeling of the constants $c_{n,k+jG}$. Thus, we can restrict wave numbers to the range $k \in \left[-\frac{\pi}{d}, \frac{\pi}{d}\right]$, with $k = -\frac{\pi}{d}$ and $k = \frac{\pi}{d}$ describing the same state. This range is called the Brillouin zone (BZ).

A.2 Orthonormal Bloch Functions

Bloch functions form an orthonormal basis of the Hilbert space (with normalization by choice of $c_{n,k}$) [154]:

$$\int dx \psi_{n,k}^*(x) \psi_{n',k'}(x) = \int dx \left(\frac{1}{\sqrt{\mathcal{N}}} \sum_j c_{n,k+jG}^* e^{-i(k+jG)x} \cdot \frac{1}{\sqrt{\mathcal{N}}} \sum_{j'} c_{n',k'+j'G} e^{i(k'+j'G)x} \right) \quad (\text{A.11})$$

$$= \frac{1}{\mathcal{N}} \sum_{j,j'} c_{n,k+jG}^* c_{n',k'+j'G} \int dx e^{i(k'-k+(j'-j)G)x} \quad (\text{A.12})$$

$$= \frac{1}{\mathcal{N}} \sum_{j,j'} c_{n,k+jG}^* c_{n',k'+j'G} 2\pi \delta(k'-k+(j'-j)G) \quad (\text{A.13})$$

The argument of the delta function is zero if $k-k'=mG$, with $m=j'-j \in \mathbb{N}$, so only if k and k' define the same state. Because we constrained $k \in \left[-\frac{\pi}{d}, \frac{\pi}{d}\right]$, k and k' need to be equal and only the case of $j=j'$ is relevant:

$$\int dx \psi_{n,k}^*(x) \psi_{n',k'}(x) = \frac{1}{\mathcal{N}} \sum_j c_{n,k+jG}^* c_{n',k'+jG} 2\pi \delta(k'-k) \quad (\text{A.14})$$

$$= \sum_j c_{n,k+jG}^* c_{n',k'+jG} \delta_{k,k'}, \quad (\text{A.15})$$

with $2\pi \delta(0)=\mathcal{N}$ fixing the normalization constant \mathcal{N} .

Finally, because eigenvectors to different eigenvalues are orthogonal:

$$\sum_j c_{n,k+jG}^* c_{n',k+jG} = \delta_{n,n'} \quad (\text{A.16})$$

$$\Rightarrow \int dx \psi_{n,k}^*(x) \psi_{n',k'}(x) = \delta_{n,n'} \delta_{k,k'} \quad (\text{A.17})$$

A.3 Equation for Bloch Functions

The eigenfunctions $\psi(x)$ of the Hamiltonian in eq. 2.17 can be easily found by equating the coefficients of the Fourier series [154]:

$$\psi(x) = \sum_k c_k e^{ikx} \quad (\text{A.18})$$

$$\hat{H} \psi(x) = \varepsilon \psi(x) \quad (\text{A.19})$$

$$\left(\frac{-\hbar^2}{2m} \partial_x^2 + \frac{V_0}{2} + \frac{V_0}{4} e^{iGx} + \frac{V_0}{4} e^{-iGx} \right) \sum_k c_k e^{ikx} = \varepsilon \sum_k c_k e^{ikx} \quad (\text{A.20})$$

$$\sum_k \left(c_k \frac{\hbar^2 k^2}{2m} e^{ikx} + c_k \frac{V_0}{2} e^{ikx} + c_k \frac{V_0}{4} e^{i(k+G)x} + c_k \frac{V_0}{4} e^{i(k-G)x} \right) = \varepsilon \sum_k c_k e^{ikx} \quad (\text{A.21})$$

$$\sum_k \left(c_k \left(\frac{\hbar^2 k^2}{2m} - \varepsilon \right) e^{ikx} + c_k \frac{V_0}{2} e^{ikx} + c_{k-G} \frac{V_0}{4} e^{ikx} + c_{k+G} \frac{V_0}{4} e^{ikx} \right) = 0 \quad (\text{A.22})$$

$$\sum_k \left(c_k \left(\frac{\hbar^2 k^2}{2m} - \varepsilon \right) + c_k \frac{V_0}{2} + c_{k-G} \frac{V_0}{4} + c_{k+G} \frac{V_0}{4} \right) e^{ikx} = 0 \quad (\text{A.23})$$

$$c_k \left(\frac{\hbar^2 k^2}{2m} - \varepsilon \right) + c_k \frac{V_0}{2} + c_{k-G} \frac{V_0}{4} + c_{k+G} \frac{V_0}{4} = 0, \quad (\text{A.24})$$

where from eq. A.21 to eq. A.22 we regroup the sum to accumulate all terms with the same exponential e^{ikx} . Because eq. A.23 has to be fulfilled for all x and the exponentials e^{ikx} are orthogonal, all terms have to be equal to zero. We can see that all constants c_k that are separated by multiples of the lattice constant G form a common system of countably infinitely many equations. This allows us to put eq. A.24 in matrix form [154]:

$$\begin{pmatrix} \ddots & \vdots & \vdots & \vdots & \vdots & \vdots & \ddots \\ \dots & \frac{V_0}{2} + \frac{\hbar^2(k-2G)^2}{2m} - \varepsilon & \frac{V_0}{4} & 0 & 0 & 0 & \dots \\ \dots & \frac{V_0}{4} & \frac{V_0}{2} + \frac{\hbar^2(k-G)^2}{2m} - \varepsilon & \frac{V_0}{4} & 0 & 0 & \dots \\ \dots & 0 & \frac{V_0}{4} & \frac{V_0}{2} + \frac{\hbar^2 k^2}{2m} - \varepsilon & \frac{V_0}{4} & 0 & \dots \\ \dots & 0 & 0 & \frac{V_0}{4} & \frac{V_0}{2} + \frac{\hbar^2(k+G)^2}{2m} - \varepsilon & \frac{V_0}{4} & \dots \\ \dots & 0 & 0 & 0 & \frac{V_0}{4} & \frac{V_0}{2} + \frac{\hbar^2(k+2G)^2}{2m} - \varepsilon & \dots \\ \ddots & \vdots & \vdots & \vdots & \vdots & \vdots & \ddots \end{pmatrix} \begin{pmatrix} \vdots \\ c_{k-2G} \\ c_{k-G} \\ c_k \\ c_{k+G} \\ c_{k+2G} \\ \vdots \end{pmatrix} = \mathbf{0} \quad (\text{A.25})$$

A.4 Orthogonal Wannier Functions

Wannier functions of different sites j or bands n are orthogonal [154]:

$$\int dx w_{n,j}^*(x) w_{n',j'}(x) \quad (\text{A.26})$$

$$= \int dx \frac{1}{\sqrt{\mathcal{N}_w}} \int_{k \in \text{BZ}} dk e^{ikjd} \psi_{n,k}^*(x) \frac{1}{\sqrt{\mathcal{N}_w}} \int_{k' \in \text{BZ}} dk' e^{-ik'j'd} \psi_{n',k'}(x) \quad (\text{A.27})$$

$$= \frac{1}{\mathcal{N}_w} \int_{k,k' \in \text{BZ}} dk dk' e^{i(kjd - k'j'd)} \int dx \psi_{n,k}^*(x) \psi_{n',k'}(x) \quad (\text{A.28})$$

$$= \frac{1}{\mathcal{N}_w} \int_{k,k' \in \text{BZ}} dk dk' e^{i(kjd - k'j'd)} \delta_{n,n'} \delta_{k,k'} \quad (\text{A.29})$$

$$= \frac{1}{\mathcal{N}_w} \delta_{n,n'} \int_{k,k' \in \text{BZ}} dk dk' e^{i(kjd - k'j'd)} \frac{2\pi}{\mathcal{N}} \delta(k - k') \quad (\text{A.30})$$

$$= \frac{2\pi}{\mathcal{N} \mathcal{N}_w} \delta_{n,n'} \int_{k \in \text{BZ}} dk e^{ik(j-j')d} \quad (\text{A.31})$$

$$= \frac{2\pi}{\mathcal{N} \mathcal{N}_w} \delta_{n,n'} 2\pi \delta(j - j') \quad (\text{A.32})$$

$$= \delta_{n,n'} \delta_{j,j'}, \quad (\text{A.33})$$

where we have used the orthonormality of Bloch functions $\psi_{n,k}(x)$ in eq. A.28 and the normalization factor of Bloch functions $\mathcal{N} = 2\pi \delta(0)$ in eq. A.30 (see page 88). In eq. A.32, $\frac{(2\pi)^2}{\mathcal{N}} \delta(0) = 2\pi = \mathcal{N}_w$ fixes the normalization constant \mathcal{N}_w .

Energy of the BEC in Hamiltonian 2.27

Hamiltonian 2.27 reads:

$$\hat{H} = \sum_{i=1}^{N_0} \left(\frac{\hat{\mathbf{p}}_i^2}{2m} + V(\mathbf{r}_i) \right) + U_0 \sum_{\langle i,j \rangle} \delta(\mathbf{r}_i - \mathbf{r}_j),$$

with $\hat{\mathbf{p}} = -i\hbar \partial_r$, the momentum operator, $U_0 = \frac{4\pi\hbar^2 a_s}{m}$ the interaction parameter and $\langle i, j \rangle$ indicating the sum running over all possible pairs of particles.

All N_0 atoms in the condensate occupy the same single-particle state $\Phi(\mathbf{r})$, which is normalized, so

$$\int d\mathbf{r} |\Phi(\mathbf{r})|^2 \stackrel{!}{=} 1. \quad (\text{B.1})$$

The N_0 -particle wave function can be written as:

$$\Psi(\mathbf{r}_1, \mathbf{r}_2, \dots, \mathbf{r}_{N_0}) = \prod_{i=1}^{N_0} \Phi(\mathbf{r}_i). \quad (\text{B.2})$$

The BEC will minimize the Hamiltonian, so we can simply write down the energy E of the N_0 -particle wave function and then minimize E [147]:

$$E = \langle \Psi | \hat{H} | \Psi \rangle \quad (\text{B.3})$$

$$= \int \prod_{k=1}^{N_0} d\mathbf{r}_k \Psi(\mathbf{r}_1, \mathbf{r}_2, \dots, \mathbf{r}_{N_0}) \hat{H} \Psi(\mathbf{r}_1, \mathbf{r}_2, \dots, \mathbf{r}_{N_0}) \quad (\text{B.4})$$

$$= \int \prod_{k=1}^{N_0} d\mathbf{r}_k \prod_{l=1}^{N_0} \Phi^*(\mathbf{r}_l) \left(\sum_{i=1}^{N_0} \left(\frac{\hat{\mathbf{p}}_i^2}{2m} + V(\mathbf{r}_i) \right) + U_0 \sum_{\langle i,j \rangle} \delta(\mathbf{r}_i - \mathbf{r}_j) \right) \prod_{m=1}^{N_0} \Phi(\mathbf{r}_m) \quad (\text{B.5})$$

The three products can be written into one as they are in turn multiplied with each other:

$$E = \int \prod_{k=1}^{N_0} d\mathbf{r}_k \Phi^*(\mathbf{r}_k) \left(\sum_{i=1}^{N_0} \left(\frac{\hat{\mathbf{p}}_i^2}{2m} + V(\mathbf{r}_i) \right) + U_0 \sum_{\langle i,j \rangle} \delta(\mathbf{r}_i - \mathbf{r}_j) \right) \Phi(\mathbf{r}_k) \quad (\text{B.6})$$

At this point, it makes sense to split the Hamiltonian in two parts (the non-interacting single-particle part and the interactions) and draw the sum in front of the integral:

$$\begin{aligned}
E &= \sum_{i=1}^{N_0} \int \prod_{k=1}^{N_0} d\mathbf{r}_k \Phi^*(\mathbf{r}_k) \left(\frac{\hat{\mathbf{p}}_i^2}{2m} + V(\mathbf{r}_i) \right) \Phi(\mathbf{r}_k) \\
&\quad + U_0 \sum_{\langle i,j \rangle} \int \prod_{k=1}^{N_0} d\mathbf{r}_k |\Phi(\mathbf{r}_k)|^2 \delta(\mathbf{r}_i - \mathbf{r}_j)
\end{aligned} \tag{B.7}$$

In the single-particle part, wave functions $\Phi(\mathbf{r})$ with $k \neq i$ are unaffected by the momentum operator and thus commute with it. In the second part, we will also separate all terms $\Phi(\mathbf{r})$ that are not affected by the delta function:

$$\begin{aligned}
E &= \sum_{i=1}^{N_0} \int \prod_{\substack{k=1 \\ k \neq i}}^{N_0} d\mathbf{r}_k |\Phi(\mathbf{r}_k)|^2 d\mathbf{r}_i \Phi^*(\mathbf{r}_i) \left(\frac{\hat{\mathbf{p}}_i^2}{2m} + V(\mathbf{r}_i) \right) \Phi(\mathbf{r}_i) \\
&\quad + U_0 \sum_{\langle i,j \rangle} \int \prod_{\substack{k=1 \\ k \neq \{i,j\}}}^{N_0} d\mathbf{r}_k |\Phi(\mathbf{r}_k)|^2 d\mathbf{r}_i d\mathbf{r}_j |\Phi(\mathbf{r}_i)|^2 |\Phi(\mathbf{r}_j)|^2 \delta(\mathbf{r}_i - \mathbf{r}_j)
\end{aligned} \tag{B.8}$$

Most terms can now be integrated out to 1:

$$\begin{aligned}
E &= \sum_{i=1}^{N_0} \int d\mathbf{r}_i \Phi^*(\mathbf{r}_i) \left(\frac{\hat{\mathbf{p}}_i^2}{2m} + V(\mathbf{r}_i) \right) \Phi(\mathbf{r}_i) \\
&\quad + U_0 \sum_{\langle i,j \rangle} \int d\mathbf{r}_i d\mathbf{r}_j |\Phi(\mathbf{r}_i)|^2 |\Phi(\mathbf{r}_j)|^2 \delta(\mathbf{r}_i - \mathbf{r}_j)
\end{aligned} \tag{B.9}$$

Since the contribution of all particles is equal, the first sum can be written as a multiplication with the particle number N_0 . In the second term, we can integrate out the delta function:

$$\begin{aligned}
E &= N_0 \int d\mathbf{r} \Phi^*(\mathbf{r}) \left(\frac{\hat{\mathbf{p}}^2}{2m} + V(\mathbf{r}) \right) \Phi(\mathbf{r}) \\
&\quad + U_0 \sum_{\langle i,j \rangle} \int d\mathbf{r}_i |\Phi(\mathbf{r}_i)|^4
\end{aligned} \tag{B.10}$$

In the remaining sum, there are $\frac{N_0(N_0-1)}{2}$ identical terms, one for every pair of particles (by design), so the whole term can be cast together again as:

$$E = N_0 \int d\mathbf{r} \Phi^*(\mathbf{r}) \left(\frac{\hat{\mathbf{p}}^2}{2m} + V(\mathbf{r}) \right) \Phi(\mathbf{r}) + U_0 \frac{N_0(N_0-1)}{2} \int d\mathbf{r} |\Phi(\mathbf{r})|^4 \quad (\text{B.11})$$

$$E \approx \int d\mathbf{r} \sqrt{N_0} \Phi^*(\mathbf{r}) \left(\frac{\hat{\mathbf{p}}^2}{2m} + V(\mathbf{r}) + \frac{U_0}{2} N_0 \Phi^*(\mathbf{r}) \Phi(\mathbf{r}) \right) \sqrt{N_0} \Phi(\mathbf{r}), \quad (\text{B.12})$$

where we approximated $N_0(N_0-1) \approx N_0^2$, which is valid for $N_0 \gg 1$.

Bogoliubov Approximation

C.1 Transformation to Momentum Space

We will now transform Hamiltonian 2.38 into momentum space [147]:

$$\hat{H} = \int_V d\mathbf{r} \hat{\psi}^\dagger(\mathbf{r}) \frac{\hat{\mathbf{p}}^2}{2m} \hat{\psi}(\mathbf{r}) + V(\mathbf{r}) \hat{\psi}^\dagger(\mathbf{r}) \hat{\psi}(\mathbf{r}) + \frac{U_0}{2} \hat{\psi}^\dagger(\mathbf{r}) \hat{\psi}^\dagger(\mathbf{r}) \hat{\psi}(\mathbf{r}) \hat{\psi}(\mathbf{r}),$$

with $\hat{\psi}(\mathbf{r})$ the field operator of a particle in the condensate. The volume V is included explicitly in the integral and we can later send it to infinity while keeping the density constant. We use the following definition for \hat{b}_p the annihilation operator in momentum space [147]:

$$\hat{b}_p := \frac{1}{\sqrt{V}} \int_V d\mathbf{r} e^{-i\frac{p\mathbf{r}}{\hbar}} \hat{\psi}(\mathbf{r}) \quad (\text{C.1})$$

$$\Rightarrow \hat{\psi}(\mathbf{r}) = \frac{1}{\sqrt{V}} \sum_p e^{i\frac{p\mathbf{r}}{\hbar}} \hat{b}_p, \quad (\text{C.2})$$

where the sum runs over all (equally spaced) allowed momentum modes. If we insert eq. C.2 into the Hamiltonian, we get:

$$\begin{aligned} \hat{H} = \int_V d\mathbf{r} \left(\frac{1}{\sqrt{V}} \sum_p e^{-i\frac{p\mathbf{r}}{\hbar}} \hat{b}_p^\dagger \frac{-\hbar^2}{2m} \partial_r^2 \frac{1}{\sqrt{V}} \sum_{p'} e^{i\frac{p'\mathbf{r}}{\hbar}} \hat{b}_{p'} \right. \\ + V(\mathbf{r}) \frac{1}{\sqrt{V}} \sum_p e^{-i\frac{p\mathbf{r}}{\hbar}} \hat{b}_p^\dagger \frac{1}{\sqrt{V}} \sum_{p'} e^{i\frac{p'\mathbf{r}}{\hbar}} \hat{b}_{p'} \\ + \frac{U_0}{2} \frac{1}{\sqrt{V}} \sum_p e^{-i\frac{p\mathbf{r}}{\hbar}} \hat{b}_p^\dagger \frac{1}{\sqrt{V}} \sum_{p'} e^{-i\frac{p'\mathbf{r}}{\hbar}} \hat{b}_{p'}^\dagger \\ \left. \cdot \frac{1}{\sqrt{V}} \sum_{p''} e^{i\frac{p''\mathbf{r}}{\hbar}} \hat{b}_{p''} \frac{1}{\sqrt{V}} \sum_{p'''} e^{i\frac{p'''\mathbf{r}}{\hbar}} \hat{b}_{p'''} \right) \quad (\text{C.3}) \end{aligned}$$

$$\begin{aligned}
\hat{H} &= \sum_{p,p'} \frac{-\hbar^2}{2m} \hat{b}_p^\dagger \hat{b}_{p'} \frac{1}{V} \int_V d\mathbf{r} e^{-i\frac{\mathbf{p}\mathbf{r}}{\hbar}} \partial_r^2 e^{i\frac{\mathbf{p}'\mathbf{r}}{\hbar}} \\
&+ \sum_{p,p'} \hat{b}_p^\dagger \hat{b}_{p'} \frac{1}{V} \int_V d\mathbf{r} e^{-i(\mathbf{p}'-\mathbf{p})\frac{\mathbf{r}}{\hbar}} V(\mathbf{r}) \\
&+ \frac{U_0}{2} \sum_{p,p',p'',p'''} \hat{b}_p^\dagger \hat{b}_{p'}^\dagger \hat{b}_{p''} \hat{b}_{p'''} \frac{1}{V^2} \int_V d\mathbf{r} e^{i(\mathbf{p}''+\mathbf{p}'''-\mathbf{p}-\mathbf{p}')\frac{\mathbf{r}}{\hbar}}
\end{aligned} \tag{C.4}$$

Now we can start using eq. C.5 to get rid of the integral over r :

$$V \delta_{p,p'} = \int_V d\mathbf{r} e^{i(\mathbf{p}-\mathbf{p}')\frac{\mathbf{r}}{\hbar}} \tag{C.5}$$

$$\begin{aligned}
\hat{H} &= \sum_{p,p'} \frac{-\hbar^2}{2m} \hat{b}_p^\dagger \hat{b}_{p'} \frac{1}{V} \int_V d\mathbf{r} \frac{-\mathbf{p}'^2}{\hbar^2} e^{i(\mathbf{p}'-\mathbf{p})\frac{\mathbf{r}}{\hbar}} \\
&+ \sum_{p,p'} \hat{b}_p^\dagger \hat{b}_{p'} \frac{1}{V} \int_V d\mathbf{r} e^{-i(\mathbf{p}'-\mathbf{p})\frac{\mathbf{r}}{\hbar}} V(\mathbf{r}) \\
&+ \frac{U_0}{2} \sum_{p,p',p'',p'''} \hat{b}_p^\dagger \hat{b}_{p'}^\dagger \hat{b}_{p''} \hat{b}_{p'''} \frac{V}{V^2} \delta_{(\mathbf{p}''+\mathbf{p}'''-\mathbf{p}),\mathbf{p}'}
\end{aligned} \tag{C.6}$$

To keep this simple, we will assume $V(\mathbf{r}) = 0$ at this point and end up with the free space single-particle dispersion $\varepsilon_p^f = \frac{p^2}{2m}$, which we will later replace by an arbitrary single-particle dispersion ε_q^0 , the zero index marking 'single-particle' as opposed to the collective excitations' dispersion that we will obtain later and q instead of p indicating a change from momentum to quasi-momentum as we introduce the lattice.

$$\begin{aligned}
\hat{H} &= \sum_{p,p'} \frac{p'^2}{2m} \hat{b}_p^\dagger \hat{b}_{p'} \frac{V}{V} \delta_{p',p} \\
&+ 0 \\
&+ \frac{U_0}{2V} \sum_{p,p'',p'''} \hat{b}_p^\dagger \hat{b}_{p''+p'''} \hat{b}_{p''} \hat{b}_{p'''}
\end{aligned} \tag{C.7}$$

In the last term, we will now substitute $\mathbf{p} = \mathbf{q} + \mathbf{p}'''$:

$$\hat{H} = \sum_p \frac{p^2}{2m} \hat{b}_p^\dagger \hat{b}_p + \frac{U_0}{2V} \sum_{q,p'',p'''} \hat{b}_{p'''+q}^\dagger \hat{b}_{p''-q}^\dagger \hat{b}_{p''} \hat{b}_{p'''} \tag{C.8}$$

Now we substitute once again $\mathbf{p}''' = \mathbf{p}$, $\mathbf{p}'' = \mathbf{p}'$ and $\mathbf{q} = \mathbf{p}'$:

$$\hat{H} = \sum_p \varepsilon_p^f \hat{b}_p^\dagger \hat{b}_p + \frac{U_0}{2V} \sum_{p,p',p''} \hat{b}_{p+p''}^\dagger \hat{b}_{p'-p''}^\dagger \hat{b}_{p'} \hat{b}_p \tag{C.9}$$

Eq. C.9 shows Hamiltonian 2.38 in momentum space. To allow for an arbitrary dispersion, we can also replace the free-particle dispersion ε_p^f by ε_p^0 .

C.2 Extraction of the zero-Momentum Mode

As most particles will be in the ground state $q=0$, operators that work on that state will carry a much greater weight and it makes sense to expand the sum in eq.2.42 with respect to \hat{b}_0 . The whole sum will be called X for concise representation:

$$\begin{aligned}
X &= \sum_{q,q',q''} \hat{b}_{q+q''}^\dagger \hat{b}_{q'-q''}^\dagger \hat{b}_{q'} \hat{b}_q \\
&= \hat{b}_0^\dagger \hat{b}_0^\dagger \hat{b}_0 \hat{b}_0 \\
&\quad + \sum_{q'' \neq 0} \hat{b}_0^\dagger \hat{b}_0^\dagger \hat{b}_{q''} \hat{b}_{-q''} + \sum_{q'' \neq 0} \hat{b}_0^\dagger \hat{b}_{-q''}^\dagger \hat{b}_0 \hat{b}_{-q''} + \sum_{q' \neq 0} \hat{b}_0^\dagger \hat{b}_{q'}^\dagger \hat{b}_{q'} \hat{b}_0 \\
&\quad + \sum_{q \neq 0} \hat{b}_q^\dagger \hat{b}_0^\dagger \hat{b}_0 \hat{b}_q + \sum_{q' \neq 0} \hat{b}_{q'}^\dagger \hat{b}_0^\dagger \hat{b}_{q'} \hat{b}_0 + \sum_{q'' \neq 0} \hat{b}_{q''}^\dagger \hat{b}_{-q''}^\dagger \hat{b}_0 \hat{b}_0 \\
&\quad + \mathcal{O}(\hat{b}_{q \neq 0}^3)
\end{aligned} \tag{C.10}$$

It can be easily seen that there cannot be a term with exactly one operator having non-zero momentum, which can physically be explained by momentum conservation, so second order is next to leading and we will neglect all higher order terms $\mathcal{O}(\hat{b}_{q \neq 0}^3)$:

$$\begin{aligned}
X &\approx \hat{b}_0^\dagger \hat{b}_0^\dagger \hat{b}_0 \hat{b}_0 \\
&\quad + \sum_{q \neq 0} \hat{b}_0^\dagger \hat{b}_0^\dagger \hat{b}_q \hat{b}_{-q} + \sum_{q \neq 0} \hat{b}_0^\dagger \hat{b}_q^\dagger \hat{b}_0 \hat{b}_q + \sum_{q \neq 0} \hat{b}_0^\dagger \hat{b}_q^\dagger \hat{b}_q \hat{b}_0 \\
&\quad + \sum_{q \neq 0} \hat{b}_q^\dagger \hat{b}_0^\dagger \hat{b}_0 \hat{b}_q + \sum_{q \neq 0} \hat{b}_q^\dagger \hat{b}_0^\dagger \hat{b}_q \hat{b}_0 + \sum_{q \neq 0} \hat{b}_q^\dagger \hat{b}_{-q}^\dagger \hat{b}_0 \hat{b}_0
\end{aligned} \tag{C.11}$$

$$\begin{aligned}
&= \hat{b}_0^\dagger \hat{b}_0^\dagger \hat{b}_0 \hat{b}_0 \\
&\quad + \hat{b}_0^\dagger \hat{b}_0^\dagger \sum_{q \neq 0} \hat{b}_q \hat{b}_{-q} + \hat{b}_0^\dagger \hat{b}_0 \sum_{q \neq 0} \hat{b}_q^\dagger \hat{b}_q + \hat{b}_0^\dagger \hat{b}_0 \sum_{q \neq 0} \hat{b}_q^\dagger \hat{b}_q \\
&\quad + \hat{b}_0^\dagger \hat{b}_0 \sum_{q \neq 0} \hat{b}_q^\dagger \hat{b}_q + \hat{b}_0^\dagger \hat{b}_0 \sum_{q \neq 0} \hat{b}_q^\dagger \hat{b}_q + \hat{b}_0 \hat{b}_0 \sum_{q \neq 0} \hat{b}_q^\dagger \hat{b}_{-q}^\dagger
\end{aligned} \tag{C.12}$$

Again, because we have many (N_0) atoms in the ground state, we can approximate $\hat{b}_0^\dagger \approx \hat{b}_0 \approx \sqrt{N_0}$:

$$X \approx N_0^2 + N_0 \left(4 \sum_{q \neq 0} \hat{b}_q^\dagger \hat{b}_q + \sum_{q \neq 0} (\hat{b}_q^\dagger \hat{b}_{-q}^\dagger + \hat{b}_q \hat{b}_{-q}) \right) \tag{C.13}$$

Now we put back eq.C.13 in the complete Hamiltonian (eq.2.42) and we get:

$$\hat{H} = \frac{N_0^2 U_0}{2V} + \sum_{q \neq 0} \left(\varepsilon_q^o + \frac{2N_0 U_0}{V} \right) \hat{b}_q^\dagger \hat{b}_q + \frac{N_0 U_0}{2V} \sum_{q \neq 0} (\hat{b}_q^\dagger \hat{b}_{-q}^\dagger + \hat{b}_q \hat{b}_{-q}) \tag{C.14}$$

We introduce the condensate density $n_0 = \frac{N_0}{V}$ and let the sum run only over positive values of q to get the Hamiltonian into a more symmetrical form:

$$\hat{H} = \frac{N_0 n_0 U_0}{2} + \sum_{q>0} \left((\varepsilon_q^0 + 2n_0 U_0) (\hat{b}_q^\dagger \hat{b}_q + \hat{b}_{-q}^\dagger \hat{b}_{-q}) + n_0 U_0 (\hat{b}_q^\dagger \hat{b}_{-q}^\dagger + \hat{b}_q \hat{b}_{-q}) \right) \quad (\text{C.15})$$

Finally, we introduce the interaction parameter $g := n_0 U_0$, which happens to be equal to the chemical potential μ , and shift the whole Hamiltonian, i.e. all modes, by E_μ . This is sensible because we are interested in the excitations atop the condensate.

$$E_\mu = -N_0 g - \sum_{q>0} g (\hat{b}_q^\dagger \hat{b}_q + \hat{b}_{-q}^\dagger \hat{b}_{-q}) \quad (\text{C.16})$$

$$\hat{H} = -\frac{g N_0}{2} + \sum_{q>0} \left((\varepsilon_q^0 + g) (\hat{b}_q^\dagger \hat{b}_q + \hat{b}_{-q}^\dagger \hat{b}_{-q}) + g (\hat{b}_q^\dagger \hat{b}_{-q}^\dagger + \hat{b}_q \hat{b}_{-q}) \right) \quad (\text{C.17})$$

C.3 Bogoliubov Transformation

We start with a Hamiltonian \hat{H} of the form:

$$\hat{H} = \varepsilon_0 (\hat{a}^\dagger \hat{a} + \hat{b}^\dagger \hat{b}) + \varepsilon_1 (\hat{a}^\dagger \hat{b}^\dagger + \hat{a} \hat{b}), \quad (\text{C.18})$$

with the bosonic annihilation operators \hat{a} and \hat{b} that satisfy:

$$[\hat{a}, \hat{a}^\dagger] = [\hat{b}, \hat{b}^\dagger] = 1 \quad (\text{C.19})$$

$$[\hat{a}, \hat{b}] = [\hat{a}, \hat{b}^\dagger] = 0 \quad (\text{C.20})$$

We now transform the Hamiltonian by introducing new bosonic annihilation operators $\hat{\alpha}$ and $\hat{\beta}$ with real valued factors u, v according to [147]:

$$\hat{\alpha} = u \hat{a} + v \hat{b}^\dagger \quad (\text{C.21})$$

$$\hat{\beta} = u \hat{b} + v \hat{a}^\dagger \quad (\text{C.22})$$

$$\Rightarrow \hat{a} = u \hat{\alpha} - v \hat{\beta}^\dagger \quad (\text{C.23})$$

$$\Rightarrow \hat{b} = u \hat{\beta} - v \hat{\alpha}^\dagger, \quad (\text{C.24})$$

that satisfy the same commutation relations:

$$[\hat{\alpha}, \hat{\alpha}^\dagger] = [\hat{\beta}, \hat{\beta}^\dagger] = 1 \quad (\text{C.25})$$

$$[\hat{\alpha}, \hat{\beta}] = [\hat{\alpha}, \hat{\beta}^\dagger] = 0 \quad (\text{C.26})$$

While eq. C.26 is trivially true, eq. C.25 yields the condition:

$$u^2 - v^2 = 1 \quad (\text{C.27})$$

We can now substitute eqs. C.23 and C.24 into eq. 2.44 and end up with:

$$\begin{aligned} \hat{H} = & 2v^2 \varepsilon_0 - 2uv \varepsilon_1 + \left(\varepsilon_0 (u^2 + v^2) - 2uv \varepsilon_1 \right) (\hat{\alpha}^\dagger \hat{\alpha} + \hat{\beta}^\dagger \hat{\beta}) \\ & + \left(\varepsilon_1 (u^2 + v^2) - 2uv \varepsilon_0 \right) (\hat{\alpha} \hat{\beta} + \hat{\alpha}^\dagger \hat{\beta}^\dagger) \end{aligned} \quad (\text{C.28})$$

The remaining degree of freedom in u and v can be fixed by making the last term in eq. C.28 vanish:

$$\varepsilon_1 (u^2 + v^2) - 2uv \varepsilon_0 \stackrel{!}{=} 0 \quad (\text{C.29})$$

For this it makes sense to parametrize u and v to make eq. C.27 trivially fulfilled:

$$u = \cosh(t) \quad (\text{C.30})$$

$$v = \sinh(t) \quad (\text{C.31})$$

At this point, we should recall the following hyperbolic trigonometric identities:

$$\cosh(2x) = \cosh^2(x) + \sinh^2(x) \quad (\text{C.32})$$

$$\sinh(2x) = 2 \cosh(x) \sinh(x) \quad (\text{C.33})$$

$$\text{artanh}(x) = \frac{1}{2} \log \left(\frac{1+x}{1-x} \right) \quad (\text{C.34})$$

$$\cosh^2(x) = \frac{1}{2} + \frac{1}{2} \cosh(2x) \quad (\text{C.35})$$

If we insert eqs. C.30 and C.31 in eq. C.29 and then use the identities eqs. C.32 and C.33, we can solve for the parameter t :

$$0 = \varepsilon_1 (\cosh^2(t) + \sinh^2(t)) - \varepsilon_0 2 \cosh(t) \sinh(t) \quad (\text{C.36})$$

$$= \varepsilon_1 \cosh(2t) - \varepsilon_0 \sinh(2t) \quad (\text{C.37})$$

$$\tanh(2t) = \frac{\varepsilon_1}{\varepsilon_0} \quad (\text{C.38})$$

$$t = \frac{1}{2} \text{artanh} \left(\frac{\varepsilon_1}{\varepsilon_0} \right) \quad (\text{C.39})$$

$$x := \frac{\varepsilon_1}{\varepsilon_0} \quad (\text{C.40})$$

Inserting eq. C.40 and eq. C.34 in eq. C.39 makes it possible to get $t(x)$ in a form that is suitable to simplify the $\cosh()$ function:

$$t = \frac{1}{2} \operatorname{artanh}(x) \quad (\text{C.41})$$

$$= \frac{1}{4} \log\left(\frac{1+x}{1-x}\right) \quad (\text{C.42})$$

Squaring eq. C.30 using eq. C.35 and inserting eq. C.42, we get $u^2(x)$:

$$u^2 = \frac{1}{2} + \frac{1}{2} \cosh(2t) \quad (\text{C.43})$$

$$= \frac{1}{2} + \frac{1}{2} \cosh\left(\frac{1}{2} \log\left(\frac{1+x}{1-x}\right)\right) \quad (\text{C.44})$$

$$= \frac{1}{2} + \frac{1}{2} \cosh\left(\log\sqrt{\frac{1+x}{1-x}}\right) \quad (\text{C.45})$$

$$= \frac{1}{2} + \frac{1}{2} \left(\frac{e^{\log\sqrt{\frac{1+x}{1-x}}} + e^{-\log\sqrt{\frac{1+x}{1-x}}}}{2} \right) \quad (\text{C.46})$$

$$= \frac{1}{2} + \frac{1}{4} \left(\sqrt{\frac{1+x}{1-x}} + \sqrt{\frac{1-x}{1+x}} \right) \quad (\text{C.47})$$

$$= \frac{1}{2} + \frac{1}{4} \left(\sqrt{\frac{(1+x)(1+x)}{(1-x)(1+x)}} + \sqrt{\frac{(1-x)(1-x)}{(1+x)(1-x)}} \right) \quad (\text{C.48})$$

$$= \frac{1}{2} + \frac{1}{4} \left(\frac{(1+x) + (1-x)}{\sqrt{1-x^2}} \right) \quad (\text{C.49})$$

$$= \frac{1}{2} + \frac{1}{2} \left(\frac{1}{\sqrt{1-x^2}} \right) \quad (\text{C.50})$$

Now, we can insert eq. C.40 in eq. C.50 and use eq. C.27 to also get an expression for v :

$$u^2 = \frac{1}{2} + \frac{1}{2} \left(\frac{1}{\sqrt{1 - \frac{\varepsilon_1^2}{\varepsilon_0^2}}} \right) \quad (\text{C.51})$$

$$= \frac{1}{2} \left(\frac{\varepsilon_0}{\sqrt{\varepsilon_0^2 - \varepsilon_1^2}} + 1 \right) \quad (\text{C.52})$$

$$u^2 = \frac{1}{2} \left(\frac{\varepsilon_0}{\varepsilon} + 1 \right) \quad (\text{C.53})$$

$$\Rightarrow v^2 = \frac{1}{2} \left(\frac{\varepsilon_0}{\varepsilon} - 1 \right) \quad (\text{C.54})$$

$$\varepsilon := \sqrt{\varepsilon_0^2 - \varepsilon_1^2} \quad (\text{C.55})$$

The Hamiltonian from eq. C.28 can now be simplified by inserting eqs. C.53 and C.54 and using eq. C.55:

$$\begin{aligned} \hat{H} &= 2\varepsilon_0 \frac{1}{2} \left(\frac{\varepsilon_0}{\varepsilon} - 1 \right) - 2\varepsilon_1 \sqrt{\frac{1}{2} \left(\frac{\varepsilon_0}{\varepsilon} + 1 \right)} \sqrt{\frac{1}{2} \left(\frac{\varepsilon_0}{\varepsilon} - 1 \right)} \\ &\quad + \left(\varepsilon_0 \left(\frac{1}{2} \left(\frac{\varepsilon_0}{\varepsilon} + 1 \right) + \frac{1}{2} \left(\frac{\varepsilon_0}{\varepsilon} - 1 \right) \right) \right. \\ &\quad \left. - 2\varepsilon_1 \sqrt{\frac{1}{2} \left(\frac{\varepsilon_0}{\varepsilon} + 1 \right)} \sqrt{\frac{1}{2} \left(\frac{\varepsilon_0}{\varepsilon} - 1 \right)} \right) (\hat{\alpha}^\dagger \hat{\alpha} + \hat{\beta}^\dagger \hat{\beta}) \end{aligned} \quad (\text{C.56})$$

$$\begin{aligned} &= \varepsilon_0 \left(\frac{\varepsilon_0}{\varepsilon} - 1 \right) - \varepsilon_1 \sqrt{\left(\frac{\varepsilon_0}{\varepsilon} + 1 \right) \left(\frac{\varepsilon_0}{\varepsilon} - 1 \right)} \\ &\quad + \left(\varepsilon_0 \frac{\varepsilon_0}{\varepsilon} - \varepsilon_1 \sqrt{\left(\frac{\varepsilon_0}{\varepsilon} + 1 \right) \left(\frac{\varepsilon_0}{\varepsilon} - 1 \right)} \right) (\hat{\alpha}^\dagger \hat{\alpha} + \hat{\beta}^\dagger \hat{\beta}) \end{aligned} \quad (\text{C.57})$$

$$= \frac{\varepsilon_0^2}{\varepsilon} - \varepsilon_0 - \varepsilon_1 \sqrt{\frac{\varepsilon_0^2}{\varepsilon^2} - 1} + \left(\frac{\varepsilon_0^2}{\varepsilon} - \varepsilon_1 \sqrt{\frac{\varepsilon_0^2}{\varepsilon^2} - 1} \right) (\hat{\alpha}^\dagger \hat{\alpha} + \hat{\beta}^\dagger \hat{\beta}) \quad (\text{C.58})$$

$$= \frac{\varepsilon_0^2}{\varepsilon} - \varepsilon_0 - \varepsilon_1 \sqrt{\frac{\varepsilon_0^2 - \varepsilon^2}{\varepsilon^2}} + \left(\frac{\varepsilon_0^2}{\varepsilon} - \varepsilon_1 \sqrt{\frac{\varepsilon_0^2 - \varepsilon^2}{\varepsilon^2}} \right) (\hat{\alpha}^\dagger \hat{\alpha} + \hat{\beta}^\dagger \hat{\beta}) \quad (\text{C.59})$$

$$= \frac{\varepsilon_0^2}{\varepsilon} - \varepsilon_0 - \varepsilon_1 \frac{\varepsilon_1}{\varepsilon} + \left(\frac{\varepsilon_0^2}{\varepsilon} - \varepsilon_1 \frac{\varepsilon_1}{\varepsilon} \right) (\hat{\alpha}^\dagger \hat{\alpha} + \hat{\beta}^\dagger \hat{\beta}) \quad (\text{C.60})$$

$$= \frac{\varepsilon_0^2 - \varepsilon_1^2}{\varepsilon} - \varepsilon_0 + \left(\frac{\varepsilon_0^2 - \varepsilon_1^2}{\varepsilon} \right) (\hat{\alpha}^\dagger \hat{\alpha} + \hat{\beta}^\dagger \hat{\beta}) \quad (\text{C.61})$$

$$\hat{H} = \varepsilon (\hat{\alpha}^\dagger \hat{\alpha} + \hat{\beta}^\dagger \hat{\beta}) + \varepsilon - \varepsilon_0 \quad (\text{C.62})$$

C.4 Bose-Hubbard Hamiltonian

Our experiment is well described by an extension of the Bose-Hubbard Hamiltonian. It can be derived from Hamiltonian 2.42 by a change of basis from momentum states \mathbf{q} to Wannier states (see sec. 2.2.3) located on site i with coordinates R_i according to:

$$\hat{H} = \sum_{\mathbf{q}} \varepsilon_{\mathbf{q}} \hat{b}_{\mathbf{q}}^\dagger \hat{b}_{\mathbf{q}} + \frac{U_0}{2V} \sum_{\mathbf{q}, \mathbf{q}', \mathbf{q}''} \hat{b}_{\mathbf{q}+\mathbf{q}''}^\dagger \hat{b}_{\mathbf{q}'-\mathbf{q}''}^\dagger \hat{b}_{\mathbf{q}'} \hat{b}_{\mathbf{q}} \quad (\text{C.63})$$

$$\hat{a}_i = \frac{1}{\sqrt{N_s}} \sum_{\mathbf{q}} e^{i \frac{\mathbf{q}}{\hbar} R_i} \hat{b}_{\mathbf{q}} \quad (\text{C.64})$$

$$\hat{b}_{\mathbf{q}} = \frac{1}{\sqrt{N_s}} \sum_j e^{-i \frac{\mathbf{q}}{\hbar} R_j} \hat{a}_j \quad (\text{C.65})$$

Here N_s is the number of sites, which is equal to the number of momentum states.

We can now perform the change of basis by inserting eq.C.65 in Hamiltonian 2.42:

$$\hat{H} = \sum_q \varepsilon_q \hat{b}_q^\dagger \hat{b}_q + \frac{U_0}{2V} \sum_{q,q',q''} \hat{b}_{q+q''}^\dagger \hat{b}_{q'-q''}^\dagger \hat{b}_{q'} \hat{b}_q \quad (\text{C.66})$$

$$\begin{aligned} &= \sum_q \varepsilon_q \frac{1}{N} \sum_j e^{i\frac{q}{\hbar}R_j} \hat{a}_j^\dagger \sum_l e^{-i\frac{q}{\hbar}R_l} \hat{a}_l \\ &\quad + \frac{U_0}{2V} \sum_{q,q',q''} \frac{1}{N^2} \sum_j e^{i\frac{q+q''}{\hbar}R_j} \hat{a}_j^\dagger \sum_l e^{i\frac{q'-q''}{\hbar}R_l} \hat{a}_l^\dagger \sum_m e^{-i\frac{q'}{\hbar}R_m} \hat{a}_m \sum_n e^{-i\frac{q}{\hbar}R_n} \hat{a}_n \end{aligned} \quad (\text{C.67})$$

$$\begin{aligned} &= \sum_{j,l} \hat{a}_j^\dagger \hat{a}_l \frac{1}{N} \sum_q \varepsilon_q e^{i\frac{q}{\hbar}(R_j-R_l)} \\ &\quad + \frac{U_0 N}{2V} \sum_{j,l,m,n} \hat{a}_j^\dagger \hat{a}_l^\dagger \hat{a}_m \hat{a}_n \frac{1}{N^3} \sum_q e^{i\frac{q}{\hbar}(R_j-R_n)} \sum_{q'} e^{i\frac{q'}{\hbar}(R_l-R_m)} \sum_{q''} e^{i\frac{q''}{\hbar}(R_j-R_l)} \end{aligned} \quad (\text{C.68})$$

$$\begin{aligned} &= \sum_{j,l} \hat{a}_j^\dagger \hat{a}_l \frac{1}{N} \sum_q \varepsilon_q e^{i\frac{q}{\hbar}(R_j-R_l)} \\ &\quad + \frac{U_0 N}{2V} \sum_{j,l,m,n} \hat{a}_j^\dagger \hat{a}_l^\dagger \hat{a}_m \hat{a}_n \frac{1}{N^3} N\delta_{j,n} N\delta_{l,m} N\delta_{j,l} \end{aligned} \quad (\text{C.69})$$

$$\hat{H} = \sum_{j,l} \hat{a}_j^\dagger \hat{a}_l \frac{1}{N} \sum_q \varepsilon_q e^{i\frac{q}{\hbar}(R_j-R_l)} + \frac{U_0 N}{2V} \sum_j \hat{a}_j^\dagger \hat{a}_j^\dagger \hat{a}_j \hat{a}_j \quad (\text{C.70})$$

Thomas-Fermi Approximation in the Lattice

Because there are many subtleties in the definition of the relevant parameters of the Thomas-Fermi approximation in the lattice, we will show the whole derivation with all relevant steps in this appendix [146, 165].

We start with the wave operators $\hat{\psi}(\mathbf{r})$ expressed via the Wannier functions of the lowest band $w_0(x)$ along x and some \mathcal{L}^2 -integrable functions $\phi_{j,\perp}(\mathbf{r}_\perp)$ with j the site index and $\mathbf{r}=(x, \mathbf{r}_\perp)$ along y and z according to eq. 2.71:

$$\hat{\psi}(\mathbf{r}) = \sum_j w_0(x-x_j) \phi_{j,\perp}(\mathbf{r}_\perp) \hat{a}_j,$$

where \hat{a}_j annihilates a particle on site j . Now the interaction Hamiltonian takes the form:

$$\begin{aligned} \hat{H}_{\text{int}} = \sum_{i,j,k,l} \int d\mathbf{r} \frac{1}{2} U_0 w_0(x-x_i)^* w_0(x-x_j)^* w_0(x-x_k) w_0(x-x_l) \\ \cdot \phi_{i,\perp}(\mathbf{r}_\perp)^* \phi_{j,\perp}(\mathbf{r}_\perp)^* \phi_{k,\perp}(\mathbf{r}_\perp) \phi_{l,\perp}(\mathbf{r}_\perp) \hat{a}_i^\dagger \hat{a}_j^\dagger \hat{a}_k \hat{a}_l. \end{aligned} \quad (\text{D.1})$$

Due to the localization of the Wannier functions at their respective sites, terms where $i=j=k=l$ is not fulfilled are suppressed by at least $\approx U/J$ with the (Bose-Hubbard) tunneling element J and the (Bose-Hubbard) on site interaction U . As we have no 3D lattice but pancakes and so the on site interaction is quite small, we can make this approximation:

$$\hat{H}_{\text{int}} \approx \frac{1}{2} U_0 \sum_j \hat{a}_j^\dagger \hat{a}_j^\dagger \hat{a}_j \hat{a}_j \int dx |w_0(x-x_j)|^4 \int d\mathbf{r}_\perp |\phi_{j,\perp}(\mathbf{r}_\perp)|^4 \quad (\text{D.2})$$

The integral along the x -direction yields the same for all sites j , so we define the Wannier integral of the lowest band $w_{0I} := \int dx |w_0(x)|^4$ that only depends on the lattice depth and draw w_{0I} in front of the sum as a constant (is index $0I$ indicates that it is the integral of the Wannier function of the lowest band, which we refer to as the zeroth). We further approximate $\hat{a}_j^\dagger \hat{a}_j^\dagger \hat{a}_j \hat{a}_j \approx \hat{n}_j^2$, with the number operator $\hat{n}_j = \hat{a}_j^\dagger \hat{a}_j$, which is valid for large atom numbers:

$$\hat{H}_{\text{int}} \approx \frac{1}{2} U_0 w_{0I} \sum_j \int d\mathbf{r}_\perp \hat{n}_j^2 |\phi_{j,\perp}(\mathbf{r}_\perp)|^4 \quad (\text{D.3})$$

We can now define the 2D density operator $\hat{n}_{j,\perp}(\mathbf{r}_\perp) = \hat{n}_j |\phi_{j,\perp}(\mathbf{r}_\perp)|^2$ which describes the 2D density in pancake j along \mathbf{r}_\perp . For small fluctuations $\langle \hat{n}_{j,\perp}(\mathbf{r}_\perp) \rangle^2 \approx \langle \hat{n}_{j,\perp}(\mathbf{r}_\perp)^2 \rangle$ it is valid to classically approximate the density as its expectation value $n_{j,\perp}(\mathbf{r}_\perp) := \langle \hat{n}_{j,\perp}(\mathbf{r}_\perp) \rangle \approx \hat{n}_{j,\perp}(\mathbf{r}_\perp)$. This yields the interaction energy in state ψ :

$$E_{\text{int}} := \langle \psi | \hat{H}_{\text{int}} | \psi \rangle \quad (\text{D.4})$$

$$\approx \frac{1}{2} U_0 w_{0I} \sum_j \int d\mathbf{r}_\perp n_{j,\perp}^2(\mathbf{r}_\perp) \quad (\text{D.5})$$

The 2D density $n_{j,\perp}(\mathbf{r}_\perp)$ is now an array of 2D functions, one for each lattice site. To make it continuous along the lattice direction, we define a 3D density $n'(\mathbf{r})$ by approximating the sum \sum_j with an integral $\frac{1}{d} \int dx$ [146]:

$$n'(\mathbf{r}) := \frac{n_{[\frac{x}{d}],\perp}(\mathbf{r}_\perp)}{d} \quad (\text{D.6})$$

$$\Rightarrow E_{\text{int}} \approx \frac{1}{2} U_{3D} w_{0I} d \int d\mathbf{r} n'^2(\mathbf{r}), \quad (\text{D.7})$$

where $[\cdot]$ denotes the rounding operation, so $[\frac{x}{d}] \cong j$. This means that the density $n'(\mathbf{r})$ is uniform within each site and we have steps between neighboring sites. We should emphasize at this point that $n'(\mathbf{r})$ is a 3D density that does not feature the modulation imprinted by the lattice. We will now go one step further and define a new 3D density $n(\mathbf{r})$, that does not depend explicitly on any density we introduced before. The reason for this is that up till now, we worked towards a useful expression for the interaction energy E_{int} , which we achieved in eq. D.7. Now we want to solve this equation for a smooth density $n(\mathbf{r})$, that does not show any modulation features or steps. We can interpret this as the envelope of the density in the experiment, which is what we see in the experiment due to the finite resolution. It should be noted at this point, that we will end up with a profile that is not quite an envelope, but rather a scaled envelope. The reason for this is that the integral over the envelope does of course not yield the atom number, but is larger. The final density will be scaled so its integral yields exactly the number of atoms in the condensate.

We now add the effective trap potential $V_{\text{trap}}(\mathbf{r})$:

$$V_{\text{trap}}(\mathbf{r}) = \frac{1}{2} m_K (\omega_x^2 x^2 + \omega_y^2 y^2 + \omega_z^2 z^2), \quad (\text{D.8})$$

to get the total potential energy of the particles in the trap E_{trap} . Note that the effective trap potential holds all confining and deconfining effects of lattice and dipole beams, but no lattice features.

Finally, we introduce the zeta parameter $\zeta := w_{0l} d$ and note that it is the only thing reminiscent of the lattice in our energy term:

$$E_{\text{pot}} := \frac{1}{2} U_0 \zeta \int d^3 r n^2(\mathbf{r}) + \int d\mathbf{r} V(\mathbf{r}) n(\mathbf{r}) \quad (\text{D.9})$$

$$= \int d\mathbf{r} \left(\frac{1}{2} U_0 \zeta n^2(\mathbf{r}) + V(\mathbf{r}) n(\mathbf{r}) \right) \quad (\text{D.10})$$

The proper density distribution of the ground state $n(\mathbf{r})$ will minimize this energy while conserving atom number N_0 . We can now use the method of Lagrange multipliers with the chemical potential μ as Lagrange multiplier:

$$\delta E_{\text{pot}} - \mu \delta N_0 \stackrel{!}{=} 0 \quad (\text{D.11})$$

$$N_0 \stackrel{!}{=} \int d\mathbf{r} n(\mathbf{r}) \quad (\text{D.12})$$

$$\Rightarrow 0 \stackrel{!}{=} \frac{\delta E_{\text{pot}}}{\delta n(\mathbf{r})} - \mu \frac{\delta N_0}{\delta n(\mathbf{r})} \quad (\text{D.13})$$

$$0 \stackrel{!}{=} \int d\mathbf{r} \left(U_0 \zeta n(\mathbf{r}) + V_{\text{trap}}(\mathbf{r}) - \mu \right) \quad (\text{D.14})$$

This is fulfilled if the integrand is zero: $U_0 \zeta n(\mathbf{r}) + V_{\text{trap}}(\mathbf{r}) - \mu = 0$. Combined with non-negativity of the density $n(\mathbf{r}) \geq 0 \forall \mathbf{r}$, we end up with:

$$n(\mathbf{r}) = \begin{cases} \frac{\mu - V_{\text{trap}}(\mathbf{r})}{U_0 \zeta} & \text{where } V_{\text{trap}}(\mathbf{r}) \leq \mu \\ 0 & \text{else.} \end{cases} \quad (\text{D.15})$$

We can now define the Thomas-Fermi radii R_i as the point on each axis where the density $n(\mathbf{r})$ goes to zero:

$$0 \stackrel{!}{=} n(r_i = R_i, r_{i \neq j} = 0) \quad (\text{D.16})$$

$$\Rightarrow \mu = V_{\text{trap}}(r_i = R_i, r_{i \neq j} = 0), \quad (\text{D.17})$$

which if inserted in eq. D.8 yields:

$$\mu = \frac{1}{2} m_K \omega_i^2 R_i^2 \quad (\text{D.18})$$

$$\Rightarrow R_i = \frac{1}{\omega_i} \sqrt{\frac{2\mu}{m_K}} \quad (\text{D.19})$$

The Thomas-Fermi radii R_i can now be used to evaluate the integral in eq. D.12 and solve for μ by substituting $q_i := \frac{r_i}{R_i}$, which with the help of eq. D.18 simplifies the trap potential in eq. D.8¹:

$$V_{\text{trap}}(\mathbf{R}q) = \frac{1}{2} m_K \left(\omega_x^2 R_x^2 q_x^2 + \omega_y^2 R_y^2 q_y^2 + \omega_z^2 R_z^2 q_z^2 \right) \quad (\text{D.20})$$

$$= \mu q^2 \quad (\text{D.21})$$

$$\Rightarrow N_0 = \int_{V \leq \mu} d\mathbf{r} \frac{\mu - V_{\text{trap}}(\mathbf{r})}{U_0 \zeta} \quad (\text{D.22})$$

$$= R_x R_y R_z \int_{V \leq \mu} d\mathbf{q} \frac{\mu - V_{\text{trap}}(\mathbf{R}q)}{U_0 \zeta}, \quad (\text{D.23})$$

$$N_0 = R_x R_y R_z \int_{|q| \leq 1} d\mathbf{q} \frac{\mu - \mu q^2}{U_0 \zeta}, \quad (\text{D.24})$$

In eq. D.24 we adjusted the integration limits using the fact that the transformation $\mathbf{r} \rightarrow \mathbf{q}$ made the Thomas-Fermi profile spherically symmetric. The integral can now easily be solved using spherical coordinates with $q := |\mathbf{q}|$:

$$N_0 = R_x R_y R_z \frac{\mu}{U_0 \zeta} \int_{|q| \leq 1} d\mathbf{q} (1 - q^2) \quad (\text{D.25})$$

$$= R_x R_y R_z \frac{\mu}{U_0 \zeta} \int_0^1 dq 4\pi q^2 (1 - q^2) \quad (\text{D.26})$$

$$N_0 = R_x R_y R_z \frac{\mu}{U_0 \zeta} 4\pi \frac{2}{15} \quad (\text{D.27})$$

We insert eq. D.19 in eq. D.27 to make all dependence on the chemical potential μ explicit:

$$N_0 = \frac{8\pi}{15} \frac{1}{\omega_x \omega_y \omega_z} \left(\frac{2\mu}{m_K} \right)^{\frac{3}{2}} \frac{\mu}{U_0 \zeta} \quad (\text{D.28})$$

Solving for μ yields the chemical potential as a function of atom number N_0 , trapping frequencies ω_i and lattice depth (implicitly contained in ζ):

$$\mu = \left(\frac{15}{8\pi} N_0 U_0 \zeta \omega_x \omega_y \omega_z \left(\frac{m_K}{2} \right)^{\frac{3}{2}} \right)^{\frac{2}{5}} \quad (\text{D.29})$$

¹This notation is actually a bit shady as $\mathbf{R}q$ in $V_{\text{trap}}(\mathbf{R}q)$ is not a scalar product, but stands for $(R_x q_x, R_y q_y, R_z q_z)$. We use it in these lines for lack of a better concise expression.

Eq. D.29 can now be in turn plugged in eq. D.19 to get the Thomas-Fermi radii R_i :

$$R_i = \frac{1}{\omega_i} \sqrt{\frac{2}{m_K}} \left(\frac{15}{8\pi} N_0 U_0 \zeta \omega_x \omega_y \omega_z \left(\frac{m_K}{2} \right)^{\frac{3}{2}} \right)^{\frac{1}{5}} \quad (\text{D.30})$$

$$= \left(\frac{15}{8\pi} N_0 U_0 \zeta \frac{\omega_x \omega_y \omega_z}{\omega_i^5} \left(\frac{2}{m_K} \right)^{-\frac{3}{2}} \left(\frac{2}{m_K} \right)^{\frac{5}{2}} \right)^{\frac{1}{5}} \quad (\text{D.31})$$

$$= \left(\frac{15}{8\pi} N_0 U_0 \zeta \frac{\omega_x \omega_y \omega_z}{\omega_i^5} \frac{2}{m_K} \right)^{\frac{1}{5}} \quad (\text{D.32})$$

$$R_i = \left(\frac{15}{4\pi} \frac{N_0 U_0 \zeta}{m_K} \frac{\omega_x \omega_y \omega_z}{\omega_i^5} \right)^{\frac{1}{5}}, \quad (\text{D.33})$$

finally plugging in $U_0 = \frac{4\pi\hbar^2 a_s}{m_K}$, we get the chemical potential μ and the Thomas-Fermi radii R_i as functions of atom number N_0 , trapping frequencies ω_i , lattice depth (implicitly contained in ζ) and scattering length a_s :

$$\mu = \left(\frac{15\hbar^2 a_s}{2m_K} N_0 \zeta \omega_x \omega_y \omega_z \left(\frac{m_K}{2} \right)^{\frac{3}{2}} \right)^{\frac{2}{5}} \quad (\text{D.34})$$

$$R_i = \left(\frac{15\hbar^2}{m_K^2} \frac{\omega_x \omega_y \omega_z}{\omega_i^5} N_0 \zeta a_s \right)^{\frac{1}{5}} \quad (\text{D.35})$$

The values for a system without lattice are reproduced for $\zeta = 1$.

Floquet Theory

E.1 Fourier Coefficients $\Phi^{(m)}$ of $\Phi(t)$

As $\Phi(t)$ is periodic in time, we can write down its Fourier series (eq. 2.94):

$$\Phi(t) = \sum_{m=-\infty}^{\infty} e^{im\omega t} \Phi^{(m)}$$

Inserting eq. 2.94 and eq. 2.86 into eq. 2.92, we get:

$$\varepsilon \sum_{m=-\infty}^{\infty} e^{im\omega t} \Phi^{(m)} = \left(\sum_{m'=-\infty}^{\infty} \left(e^{im'\omega t} \hat{H}^{(m')} \right) - i\hbar \partial_t \right) \sum_{m''=-\infty}^{\infty} e^{im''\omega t} \Phi^{(m'')} \quad (\text{E.1})$$

$$\begin{aligned} \sum_{m=-\infty}^{\infty} e^{im\omega t} \varepsilon \Phi^{(m)} &= \sum_{m', m''=-\infty}^{\infty} \left(e^{i(m'+m'')\omega t} \hat{H}^{(m')} \Phi^{(m'')} \right) \\ &+ \sum_{m''=-\infty}^{\infty} e^{im''\omega t} m'' \hbar \omega \Phi^{(m'')} \end{aligned} \quad (\text{E.2})$$

After relabeling the first term on the right hand side with $m' = m - m''$ and then again with $m'' = m'$, and the second term with $m'' = m$, we get:

$$\sum_{m=-\infty}^{\infty} e^{im\omega t} \varepsilon \Phi^{(m)} = \sum_{m, m'=-\infty}^{\infty} \left(e^{im\omega t} \hat{H}^{(m-m')} \Phi^{(m')} \right) + \sum_{m=-\infty}^{\infty} e^{im\omega t} m \hbar \omega \Phi^{(m)} \quad (\text{E.3})$$

Because eq. E.3 has to be fulfilled for all t , all coefficients of the exponential $e^{im\omega t}$ need fulfill:

$$\varepsilon \Phi^{(m)} = \sum_{m'=-\infty}^{\infty} \left(\hat{H}^{(m-m')} \Phi^{(m')} \right) + m \hbar \omega \Phi^{(m)} \quad (\text{E.4})$$

$$0 = (m \hbar \omega - \varepsilon) \Phi^{(m)} + \sum_{m'=-\infty}^{\infty} \hat{H}^{(m-m')} \Phi^{(m')} \quad (\text{E.5})$$

E.2 Effective Hamiltonian $\hat{H}_{F'}$

From the definition of the micro-motion operator $\hat{M}_{F'}(t)$ (eq. 2.100) that transforms the state $\psi(t)$ into the Floquet frame, we can derive the form of the Hamiltonian in the Floquet frame $\hat{H}_{F'}$:

$$\psi(t) := \hat{M}_{F'}(t) \psi_{F'}(t)$$

$$i\hbar \partial_t |\psi(t)\rangle = \hat{H}(t) |\psi(t)\rangle \quad (\text{E.6})$$

$$\hat{M}_{F'}^\dagger(t) i\hbar \partial_t |\psi(t)\rangle = \hat{M}_{F'}^\dagger(t) \hat{H}(t) |\psi(t)\rangle \quad (\text{E.7})$$

$$i\hbar \hat{M}_{F'}^\dagger(t) \partial_t \left(\hat{M}_{F'}(t) |\psi_{F'}(t)\rangle \right) = \hat{M}_{F'}^\dagger(t) \hat{H}(t) \hat{M}_{F'}(t) |\psi_{F'}(t)\rangle \quad (\text{E.8})$$

$$\left(i\hbar \hat{M}_{F'}^\dagger(t) \hat{U}_{F'}(t) + i\hbar \partial_t \right) |\psi_{F'}(t)\rangle = \hat{M}_{F'}^\dagger(t) \hat{H}(t) \hat{M}_{F'}(t) |\psi_{F'}(t)\rangle \quad (\text{E.9})$$

$$i\hbar \partial_t |\psi_{F'}(t)\rangle = \left(\hat{M}_{F'}^\dagger(t) \hat{H}(t) \hat{M}_{F'}(t) \right. \quad (\text{E.10})$$

$$\left. - i\hbar \hat{M}_{F'}^\dagger(t) \dot{\hat{M}}_{F'}(t) \right) |\psi_{F'}(t)\rangle \quad (\text{E.11})$$

$$i\hbar \partial_t |\psi_{F'}(t)\rangle := \hat{H}_{F'} |\psi_{F'}(t)\rangle \quad (\text{E.12})$$

$$\hat{H}_{F'} = \hat{M}_{F'}^\dagger(t) \hat{H}(t) \hat{M}_{F'}(t) - i\hbar \hat{M}_{F'}^\dagger(t) \dot{\hat{M}}_{F'}(t), \quad (\text{E.13})$$

where we started from the Schrödinger equation, multiplied by $\hat{M}_{F'}^\dagger(t)$ from the left and the inserted eq. 2.100.

E.3 Time-Evolution Operator $\hat{U}(t_2, t_1)$

The effective Hamiltonian $\hat{H}_{F'}$ can be used to simplify the time-evolution operator $\hat{U}(t, t_0)$ by transforming to the Floquet frame and back. We start from the definition of the time-evolution operator in eq. 2.102:

$$\hat{U}(t, t_0) := \mathcal{T}_t e^{-\frac{i}{\hbar} \int_{t_0}^t dt' \hat{H}(t')}$$

$$\hat{U}_{F'}(t, t_0) = \mathcal{T}_t e^{-\frac{i}{\hbar} \int_{t_0}^t dt' \hat{H}_{F'}} \quad (\text{E.14})$$

$$= e^{-\frac{i}{\hbar} (t-t_0) \hat{H}_{F'}}, \quad (\text{E.15})$$

with the time-ordering operator \mathcal{T}_t . Here we make use of the fact that the effective Hamiltonian $\hat{H}_{F'}$ was designed to be time-independent.

The norm of states can now be used to get to equal formulations of $\hat{U}(t, t_0)$:

$$1 = \langle \psi_{F'}(t) | \psi_{F'}(t) \rangle \quad (\text{E.16})$$

$$= \langle \psi_{F'}(t) | \hat{U}_{F'}(t, t_0) | \psi_{F'}(t_0) \rangle \quad (\text{E.17})$$

$$= \langle \psi(t) | \hat{M}_{F'}(t) \hat{U}_{F'}(t, t_0) \hat{M}_{F'}^\dagger(t_0) | \psi(t_0) \rangle \quad (\text{E.18})$$

$$1 = \langle \psi_F(t) | \psi_F(t) \rangle \quad (\text{E.19})$$

$$= \langle \psi(t) | \hat{U}(t, t_0) | \psi(t_0) \rangle \quad (\text{E.20})$$

By equating eqs. E.18 and E.20, and inserting eq. E.15, we arrive at:

$$\hat{U}(t, t_0) = \hat{M}_{F'}(t) e^{-\frac{i}{\hbar}(t-t_0)\hat{H}_{F'}} \hat{M}_{F'}^\dagger(t_0), \quad (\text{E.21})$$

The time-evolution operator $\hat{U}(t, t_0)$ has the following interesting properties:

1.) Periodicity with respect to a shift by multiples of the driving period T :

$$\hat{U}(nT+t_0+t, nT+t_0) = \mathcal{T}_t e^{-\frac{i}{\hbar} \int_{nT+t_0}^{nT+t_0+t} dt' \hat{H}(t')} \quad (\text{E.22})$$

$$= \mathcal{T}_t e^{-\frac{i}{\hbar} \int_{t_0}^{t_0+t} dt' \hat{H}(t'-nT)} \quad (\text{E.23})$$

$$= \mathcal{T}_t e^{-\frac{i}{\hbar} \int_{t_0}^{t_0+t} dt' \hat{H}(t')} \quad (\text{E.24})$$

$$\hat{U}(nT+t_0+t, nT+t_0) = \hat{U}(t_0+t, t_0), \quad (\text{E.25})$$

where we make use of the periodicity of the Hamiltonian $\hat{H}(t)$.

2.) An operator mediating time-evolution over more than one cycle can be split into two operators starting evolution at $t = 0$:

$$\hat{U}(nT+t, 0) = \hat{U}(nT+t, nT) \hat{U}(nT, 0) \quad (\text{E.26})$$

$$\hat{U}(nT+t, 0) = \hat{U}(t, 0) \hat{U}(nT, 0), \quad (\text{E.27})$$

where we make use of eq. E.25.

3.) An operator mediating time-evolution over multiple cycles is equal to repeated application of evolution over a single-cycle:

$$\hat{U}(nT, 0) = \hat{U}(nT, T) \hat{U}(T, 0) \quad (\text{E.28})$$

$$= \hat{U}((n-1)T, 0) \hat{U}(T, 0) \quad (\text{E.29})$$

$$\Rightarrow \hat{U}(nT, 0) = \hat{U}(T, 0)^n, \quad (\text{E.30})$$

where we also make use of eq. E.25.

E.4 Transformation to the Rotating Frame

If we have a Hamiltonian of the form:

$$\hat{H}(t) = \hat{H}_0 + \lambda(t) \hat{H}_1, \quad (\text{E.31})$$

we can transform it to the rotating frame by applying a transformation $\hat{V}(t)$ (by convention $\hat{V}(t)$ describes the transformation from the rotating frame to the lab frame) that effectively annuls the effect of $\lambda(t)$ [179]:

$$|\psi^{\text{rot}}\rangle = \hat{V}^\dagger(t) |\psi\rangle \quad (\text{E.32})$$

$$\hat{H}^{\text{rot}}(t) = \hat{V}^\dagger(t) \hat{H}(t) \hat{V}(t) - i\hbar \hat{V}^\dagger(t) \dot{\hat{V}}(t) \quad (\text{E.33})$$

$$= \hat{V}^\dagger(t) (\hat{H}_0 + \lambda(t) \hat{H}_1) \hat{V}(t) - i\hbar \hat{V}^\dagger(t) \dot{\hat{V}}(t) \quad (\text{E.34})$$

$$\stackrel{!}{=} \hat{V}^\dagger(t) \hat{H}_0 \hat{V}(t) \quad (\text{E.35})$$

$$\Rightarrow \lambda(t) \hat{H}_1 \hat{V}(t) \stackrel{!}{=} i\hbar \dot{\hat{V}}(t) \quad (\text{E.36})$$

$$\Rightarrow \hat{V}(t) = e^{-\frac{i}{\hbar} \hat{H}_1 \int_{t_0}^t dt' \lambda(t')} \quad (\text{E.37})$$

Applied to our extended Bose-Hubbard Hamiltonian (eq.2.65), we make the following transformation [164]:

$$\hat{H}(t) = -J \sum_j (\hat{a}_j^\dagger \hat{a}_{j+1} + \hat{a}_{j+1}^\dagger \hat{a}_j) + K \cos(\omega t) \sum_j j \hat{n}_j + \frac{U}{2} \sum_j \hat{n}_j (\hat{n}_j - 1)$$

$$\Rightarrow \hat{H}_0 = -J \sum_j (\hat{a}_j^\dagger \hat{a}_{j+1} + \hat{a}_{j+1}^\dagger \hat{a}_j) + \frac{U}{2} \sum_j \hat{n}_j (\hat{n}_j - 1) \quad (\text{E.38})$$

$$\hat{H}_1 = \sum_j j \hat{n}_j \quad (\text{E.39})$$

$$\lambda(t) = K \cos(\omega t) \quad (\text{E.40})$$

$$\Rightarrow \hat{V}(t) = e^{-i \frac{K}{\hbar} \sum_j j \hat{n}_j \int_{t_0}^t dt' \cos(\omega t')}, \quad (\text{E.41})$$

with J the tunneling, K the driving amplitude and U the on-site interaction energy. For $t_0=0$ and $\alpha = \frac{K}{\hbar\omega}$ the driving strength, $\hat{V}(t)$ evaluates to:

$$\hat{V}(t) = e^{-i\alpha \sin(\omega t) \sum_j j \hat{n}_j} \quad (\text{E.42})$$

$$(\text{E.43})$$

Performing this transformation results in $\hat{H}^{\text{rot}}(t)$:

$$\hat{H}^{\text{rot}}(t) = e^{i\alpha \sin(\omega t) \sum_k k \hat{n}_k} \left(-J \sum_j (\hat{a}_j^\dagger \hat{a}_{j+1} + \hat{a}_{j+1}^\dagger \hat{a}_j) + \frac{U}{2} \sum_j \hat{n}_j (\hat{n}_j - 1) \right) e^{-i\alpha \sin(\omega t) \sum_l l \hat{n}_l} \quad (\text{E.44})$$

$$\hat{H}^{\text{rot}}(t) = -J e^{i\alpha \sin(\omega t) \sum_k k \hat{n}_k} \sum_j (\hat{a}_j^\dagger \hat{a}_{j+1} + \hat{a}_{j+1}^\dagger \hat{a}_j) e^{-i\alpha \sin(\omega t) \sum_l l \hat{n}_l} + \frac{U}{2} \sum_j \hat{n}_j (\hat{n}_j - 1), \quad (\text{E.45})$$

where we used that a function of an operator commutes with that operator to move the interaction part of the Hamiltonian past $\hat{V}(t)$. To also move the tunneling part of the Hamiltonian, we use the commutators $[\hat{a}, e^{x \hat{n}}]$ and $[\hat{a}^\dagger, e^{x \hat{n}}]$ as derived in appendix E.5 (eqs. E.68 and E.87) and arrive at:

$$\begin{aligned} \hat{a} e^{x \hat{n}} &= e^{x \hat{n}} \hat{a} e^x \\ \hat{a}^\dagger e^{x \hat{n}} &= e^{x \hat{n}} \hat{a}^\dagger e^{-x} \end{aligned}$$

We can rearrange eq. E.45 using the fact that creation and annihilation operators commute for different sites:

$$e^{i\alpha \sin(\omega t) \sum_k k \hat{n}_k} (\hat{a}_j^\dagger \hat{a}_{j+1} + \hat{a}_{j+1}^\dagger \hat{a}_j) e^{-i\alpha \sin(\omega t) \sum_l l \hat{n}_l} \quad (\text{E.46})$$

$$= e^{i\alpha \sin(\omega t) (j \hat{n}_j + (j+1) \hat{n}_{j+1})} (\hat{a}_j^\dagger \hat{a}_{j+1} + \hat{a}_{j+1}^\dagger \hat{a}_j) e^{-i\alpha \sin(\omega t) (j \hat{n}_j + (j+1) \hat{n}_{j+1})} \quad (\text{E.47})$$

$$= e^{i\alpha \sin(\omega t) (j \hat{n}_j + (j+1) \hat{n}_{j+1})} e^{-i\alpha \sin(\omega t) (j \hat{n}_j + (j+1) \hat{n}_{j+1})} \cdot \left(\hat{a}_j^\dagger e^{i j \alpha \sin(\omega t)} \hat{a}_{j+1} e^{-i(j+1) \alpha \sin(\omega t)} + \hat{a}_{j+1}^\dagger e^{i(j+1) \alpha \sin(\omega t)} \hat{a}_j e^{-i j \alpha \sin(\omega t)} \right) \quad (\text{E.48})$$

$$= e^{-i\alpha \sin(\omega t)} \hat{a}_j^\dagger \hat{a}_{j+1} + e^{i\alpha \sin(\omega t)} \hat{a}_{j+1}^\dagger \hat{a}_j \quad (\text{E.49})$$

Because this rearrangement is independent of the site index j , we can do it for all pairs $\langle j, j+1 \rangle$ and insert eq. E.49 into eq. E.45:

$$\hat{H}^{\text{rot}}(t) = -J \sum_{\langle i, j \rangle} \left(e^{-i\alpha \sin(\omega t)} \hat{a}_i^\dagger \hat{a}_j + e^{i\alpha \sin(\omega t)} \hat{a}_j^\dagger \hat{a}_i \right) + \frac{U}{2} \sum_j \hat{n}_j (\hat{n}_j - 1) \quad (\text{E.50})$$

E.5 Commutators $[\hat{a}, e^{x \hat{n}}]$ and $[\hat{a}^\dagger, e^{x \hat{n}}]$

To get the commutator $[\hat{a}, e^{\hat{n}}]$, we will start with two functions $f(x)$, $g(x)$, the commutator $[\hat{a}, \hat{a}^\dagger \hat{a}]$ and show that these two functions are equal¹:

$$\begin{aligned} [\hat{a}, \hat{a}^\dagger \hat{a}] &= [\hat{a}, \hat{a}^\dagger] \hat{a} + \hat{a}^\dagger [\hat{a}, \hat{a}] \\ &= [\hat{a}, \hat{a}^\dagger] \hat{a} \\ [\hat{a}, \hat{a}^\dagger \hat{a}] &= \hat{a} \end{aligned} \tag{E.51}$$

$$f(x) := e^{-x \hat{a}^\dagger \hat{a}} \hat{a} e^{x \hat{a}^\dagger \hat{a}} \tag{E.52}$$

$$g(x) := e^x \hat{a} \tag{E.53}$$

$$f(0) = e^{-0} \hat{a} e^0 = \hat{a} \tag{E.54}$$

$$g(0) = e^0 \hat{a} = \hat{a} \tag{E.55}$$

$$\Rightarrow f(0) = g(0) \tag{E.56}$$

Both functions are equal at $x = 0$. We will show that they also satisfy the same first order differential equation:

$$\frac{\partial}{\partial x} f(x) = e^{-x \hat{a}^\dagger \hat{a}} (-\hat{a}^\dagger \hat{a}) \hat{a} e^{x \hat{a}^\dagger \hat{a}} + e^{-x \hat{a}^\dagger \hat{a}} \hat{a} e^{x \hat{a}^\dagger \hat{a}} (\hat{a}^\dagger \hat{a}) \tag{E.57}$$

$$= -e^{-x \hat{a}^\dagger \hat{a}} (\hat{a}^\dagger \hat{a}) \hat{a} e^{x \hat{a}^\dagger \hat{a}} + e^{-x \hat{a}^\dagger \hat{a}} \hat{a} (\hat{a}^\dagger \hat{a}) e^{x \hat{a}^\dagger \hat{a}} \tag{E.58}$$

$$= e^{-x \hat{a}^\dagger \hat{a}} [\hat{a}, \hat{a}^\dagger \hat{a}] e^{x \hat{a}^\dagger \hat{a}} \tag{E.59}$$

$$= e^{-x \hat{a}^\dagger \hat{a}} \hat{a} e^{x \hat{a}^\dagger \hat{a}} \tag{E.60}$$

$$\frac{\partial}{\partial x} f(x) = f(x) \tag{E.61}$$

where from eq. E.57 to eq. E.58 we used that a function of an operator commutes with that operator.

$$\frac{\partial}{\partial x} g(x) = e^x \hat{a} \tag{E.62}$$

$$= g(x) \tag{E.63}$$

So $f(x)$ and $g(x)$ satisfy the same differential equation with the same boundary condition.

¹ This proof was posted on <https://www.physicsforums.com/threads/creation-anhilation-operator-exponential-commutator-relation.793052/> by **arkajad** in response to a question by **teroenza**.

They must therefore be equal:

$$f(x) = g(x) \quad (\text{E.64})$$

$$e^{-x\hat{a}^\dagger\hat{a}}\hat{a}e^{x\hat{a}^\dagger\hat{a}} = e^x\hat{a} \quad (\text{E.65})$$

We can now rearrange eq. E.65 to get the original commutator:

$$e^{-x\hat{a}^\dagger\hat{a}}\hat{a}e^{x\hat{a}^\dagger\hat{a}} = e^{-x\hat{a}^\dagger\hat{a}}e^{x\hat{a}^\dagger\hat{a}}e^x\hat{a} \quad (\text{E.66})$$

$$e^{-x\hat{a}^\dagger\hat{a}}\hat{a}e^{x\hat{a}^\dagger\hat{a}} = e^{-x\hat{a}^\dagger\hat{a}}e^xe^{x\hat{a}^\dagger\hat{a}}\hat{a} \quad (\text{E.67})$$

$$\hat{a}e^{x\hat{a}^\dagger\hat{a}} = e^xe^{x\hat{a}^\dagger\hat{a}}\hat{a} \quad (\text{E.68})$$

$$\hat{a}e^{x\hat{a}^\dagger\hat{a}} - e^{x\hat{a}^\dagger\hat{a}}\hat{a} = e^xe^{x\hat{a}^\dagger\hat{a}}\hat{a} - e^{x\hat{a}^\dagger\hat{a}}\hat{a} \quad (\text{E.69})$$

$$[\hat{a}, e^{x\hat{a}^\dagger\hat{a}}] = (e^x - 1)e^{x\hat{a}^\dagger\hat{a}}\hat{a} \quad (\text{E.70})$$

$$[\hat{a}, e^{x\hat{n}}] = (e^x - 1)e^{x\hat{n}}\hat{a} \quad (\text{E.71})$$

Analogously, we get the commutator $[\hat{a}^\dagger, e^{x\hat{n}}]$ by redefining $f(x)$ and $g(x)$:

$$f(x) := e^{-x\hat{a}^\dagger\hat{a}}\hat{a}^\dagger e^{x\hat{a}^\dagger\hat{a}} \quad (\text{E.72})$$

$$f(0) = e^{-0}\hat{a}^\dagger e^0 = \hat{a}^\dagger \quad (\text{E.73})$$

$$\frac{\partial}{\partial x}f(x) = e^{-x\hat{a}^\dagger\hat{a}}(-\hat{a}^\dagger\hat{a})\hat{a}^\dagger e^{x\hat{a}^\dagger\hat{a}} + e^{-x\hat{a}^\dagger\hat{a}}\hat{a}^\dagger e^{x\hat{a}^\dagger\hat{a}}(\hat{a}^\dagger\hat{a}) \quad (\text{E.74})$$

$$= e^{-x\hat{a}^\dagger\hat{a}}[\hat{a}^\dagger, \hat{a}^\dagger\hat{a}]e^{x\hat{a}^\dagger\hat{a}} \quad (\text{E.75})$$

$$= -e^{-x\hat{a}^\dagger\hat{a}}\hat{a}^\dagger e^{x\hat{a}^\dagger\hat{a}} \quad (\text{E.76})$$

$$\frac{\partial}{\partial x}f(x) = -f(x), \quad (\text{E.77})$$

so the proper definition for $g(x)$ is now:

$$g(x) := e^{-x}\hat{a}^\dagger \quad (\text{E.78})$$

$$g(0) = e^{-0}\hat{a}^\dagger = \hat{a}^\dagger \quad (\text{E.79})$$

$$\Rightarrow f(0) = g(0) \quad (\text{E.80})$$

$$\frac{\partial}{\partial x}g(x) = -e^{-x}\hat{a}^\dagger \quad (\text{E.81})$$

$$= -g(x) \quad (\text{E.82})$$

Again, due to the uniqueness of the solution to a first-order differential equation with one boundary condition:

$$f(x) = g(x) \quad (\text{E.83})$$

$$e^{-x \hat{a}^\dagger \hat{a}} \hat{a}^\dagger e^{x \hat{a}^\dagger \hat{a}} = e^{-x} \hat{a}^\dagger \quad (\text{E.84})$$

$$e^{-x \hat{a}^\dagger \hat{a}} \hat{a}^\dagger e^{x \hat{a}^\dagger \hat{a}} = e^{-x \hat{a}^\dagger \hat{a}} e^{x \hat{a}^\dagger \hat{a}} e^{-x} \hat{a}^\dagger \quad (\text{E.85})$$

$$\hat{a}^\dagger e^{x \hat{a}^\dagger \hat{a}} = e^{x \hat{a}^\dagger \hat{a}} e^{-x} \hat{a}^\dagger \quad (\text{E.86})$$

$$\hat{a}^\dagger e^{x \hat{a}^\dagger \hat{a}} = e^{-x} e^{x \hat{a}^\dagger \hat{a}} \hat{a}^\dagger \quad (\text{E.87})$$

$$\hat{a}^\dagger e^{x \hat{a}^\dagger \hat{a}} - e^{x \hat{a}^\dagger \hat{a}} \hat{a}^\dagger = e^{-x} e^{x \hat{a}^\dagger \hat{a}} \hat{a}^\dagger - e^{x \hat{a}^\dagger \hat{a}} \hat{a}^\dagger \quad (\text{E.88})$$

$$[\hat{a}^\dagger, e^{x \hat{a}^\dagger \hat{a}}] = (e^{-x} - 1) e^{x \hat{a}^\dagger \hat{a}} \hat{a}^\dagger \quad (\text{E.89})$$

$$[\hat{a}^\dagger, e^{x \hat{n}}] = (e^{-x} - 1) e^{x \hat{n}} \hat{a}^\dagger \quad (\text{E.90})$$

Parametric Oscillator

F.1 Mapping to Hill Differential Equation

A homogeneous differential equation of second order as eq. 2.136 with $\beta(t)$ and $\omega^2(t)$ having a common period can be mapped onto the Hill differential equation.

$$\ddot{x}(t) + \beta(t) \dot{x}(t) + \omega^2(t) x(t) = 0$$

We perform this mapping by choosing the ansatz eq. F.1 :

$$x(t) := q(t) e^{-\frac{1}{2} \int_0^t dt' \beta(t')} \quad (\text{F.1})$$

$$\Rightarrow \dot{x}(t) = \dot{q}(t) e^{-\frac{1}{2} \int_0^t dt' \beta(t')} + q(t) e^{-\frac{1}{2} \int_0^t dt' \beta(t')} \left(-\frac{1}{2} \beta(t) \right) \quad (\text{F.2})$$

$$\begin{aligned} \Rightarrow \ddot{x}(t) = & \ddot{q}(t) e^{-\frac{1}{2} \int_0^t dt' \beta(t')} + \dot{q}(t) e^{-\frac{1}{2} \int_0^t dt' \beta(t')} \left(-\frac{1}{2} \beta(t) \right) \\ & + \dot{q}(t) e^{-\frac{1}{2} \int_0^t dt' \beta(t')} \left(-\frac{1}{2} \beta(t) \right) + q(t) e^{-\frac{1}{2} \int_0^t dt' \beta(t')} \left(-\frac{1}{2} \beta(t) \right)^2 \\ & + q(t) e^{-\frac{1}{2} \int_0^t dt' \beta(t')} \left(-\frac{1}{2} \dot{\beta}(t) \right) \end{aligned} \quad (\text{F.3})$$

Inserting $x(t)$, $\dot{x}(t)$ and $\ddot{x}(t)$ in the original differential equation 2.136 yields a new differential equation for $q(t)$:

$$\begin{aligned} 0 = & \ddot{q}(t) + 2\dot{q}(t) \left(-\frac{1}{2} \beta(t) \right) + q(t) \left(-\frac{1}{2} \beta(t) \right)^2 + q(t) \left(-\frac{1}{2} \dot{\beta}(t) \right) \\ & + \dot{q}(t) \beta(t) + q(t) \beta(t) \left(-\frac{1}{2} \beta(t) \right) + \omega^2(t) q(t) \end{aligned} \quad (\text{F.4})$$

$$0 = \ddot{q}(t) - \frac{1}{4} \beta^2(t) q(t) - \frac{1}{2} \dot{\beta}(t) q(t) + \omega^2(t) q(t) \quad (\text{F.5})$$

$$(\text{F.6})$$

All pre-factors of $q(t)$ can be summed up to define the effective time-dependent frequency $\omega'(t)$:

$$0 = \ddot{q}(t) + \omega'^2(t) q(t) \quad (\text{F.7})$$

$$\omega'^2(t) := \omega^2(t) - \frac{1}{4}\beta^2(t) - \frac{1}{2}\dot{\beta}(t) \quad (\text{F.8})$$

F.2 Classical Parametric Oscillator

While the driven harmonic oscillator always oscillates with the driving frequency, the parametric oscillator's dynamics is governed by the current eigen-frequency $\omega_0^2(1+A\cos(\Omega t))$ on short timescales $\Delta t \ll \frac{1}{\Omega}$.

The differential equation of the parametric oscillator (eq. 2.140) can be solved using ansatz F.9 [186]:

$$\begin{aligned} 0 &= \ddot{q}(t) + \omega_0^2(1+A\cos(\Omega t)) q(t) \\ q(t) &= c_1(t) \cos\left(\frac{\Omega}{2}t\right) + c_2(t) \sin\left(\frac{\Omega}{2}t\right) \end{aligned} \quad (\text{F.9})$$

With this ansatz, the derivatives of $q(t)$ are:

$$\begin{aligned} \dot{q}(t) &= \dot{c}_1(t) \cos\left(\frac{\Omega}{2}t\right) - c_1(t) \frac{\Omega}{2} \sin\left(\frac{\Omega}{2}t\right) \\ &\quad + \dot{c}_2(t) \sin\left(\frac{\Omega}{2}t\right) + c_2(t) \frac{\Omega}{2} \cos\left(\frac{\Omega}{2}t\right) \end{aligned} \quad (\text{F.10})$$

$$\begin{aligned} \ddot{q}(t) &= \ddot{c}_1(t) \cos\left(\frac{\Omega}{2}t\right) - 2\dot{c}_1(t) \frac{\Omega}{2} \sin\left(\frac{\Omega}{2}t\right) - c_1(t) \frac{\Omega^2}{4} \cos\left(\frac{\Omega}{2}t\right) \\ &\quad + \ddot{c}_2(t) \sin\left(\frac{\Omega}{2}t\right) + 2\dot{c}_2(t) \frac{\Omega}{2} \cos\left(\frac{\Omega}{2}t\right) - c_2(t) \frac{\Omega^2}{4} \sin\left(\frac{\Omega}{2}t\right) \end{aligned} \quad (\text{F.11})$$

If we assume that the coefficients $c_1(t)$ and $c_2(t)$ vary slowly in time compared to the main oscillation with frequency $\frac{\Omega}{2}$ and their second derivatives $\ddot{c}_1(t)$ and $\ddot{c}_2(t)$ are small, we can neglect the respective terms in eq. F.11 [186]:

$$\begin{aligned} \ddot{q}(t) &\approx -2\dot{c}_1(t) \frac{\Omega}{2} \sin\left(\frac{\Omega}{2}t\right) - c_1(t) \frac{\Omega^2}{4} \cos\left(\frac{\Omega}{2}t\right) \\ &\quad + 2\dot{c}_2(t) \frac{\Omega}{2} \cos\left(\frac{\Omega}{2}t\right) - c_2(t) \frac{\Omega^2}{4} \sin\left(\frac{\Omega}{2}t\right) \end{aligned} \quad (\text{F.12})$$

We can now put eqs. F.9 and F.12 in eq. 2.140 :

$$\begin{aligned}
0 = & -2\dot{c}_1(t) \frac{\Omega}{2} \sin\left(\frac{\Omega}{2} t\right) - c_1(t) \frac{\Omega^2}{4} \cos\left(\frac{\Omega}{2} t\right) \\
& + 2\dot{c}_2(t) \frac{\Omega}{2} \cos\left(\frac{\Omega}{2} t\right) - c_2(t) \frac{\Omega^2}{4} \sin\left(\frac{\Omega}{2} t\right) \\
& + \omega_0^2 \left(1 + A \cos(\Omega t)\right) \left(c_1(t) \cos\left(\frac{\Omega}{2} t\right) + c_2(t) \sin\left(\frac{\Omega}{2} t\right)\right)
\end{aligned} \tag{F.13}$$

The following trigonometric identities can be used to simplify the last term:

$$\begin{aligned}
\cos(x) \cos(2x) &= \frac{e^{ix} + e^{-ix}}{2} \frac{e^{2ix} + e^{-2ix}}{2} = \frac{e^{3ix} + e^{-3ix} + e^{ix} + e^{-ix}}{4} \\
&= \frac{1}{2} \left(\cos(3x) + \cos(x)\right)
\end{aligned} \tag{F.14}$$

$$\begin{aligned}
\sin(x) \cos(2x) &= \frac{e^{ix} - e^{-ix}}{2} \frac{e^{2ix} + e^{-2ix}}{2} = \frac{e^{3ix} - e^{-3ix} - e^{ix} + e^{-ix}}{4} \\
&= \frac{1}{2} \left(\sin(3x) - \sin(x)\right)
\end{aligned} \tag{F.15}$$

If we put eqs. F.14 and F.15 in eq. F.13, we get:

$$\begin{aligned}
0 = & -2\dot{c}_1(t) \frac{\Omega}{2} \sin\left(\frac{\Omega}{2} t\right) - c_1(t) \frac{\Omega^2}{4} \cos\left(\frac{\Omega}{2} t\right) \\
& + 2\dot{c}_2(t) \frac{\Omega}{2} \cos\left(\frac{\Omega}{2} t\right) - c_2(t) \frac{\Omega^2}{4} \sin\left(\frac{\Omega}{2} t\right) \\
& + c_1(t) \omega_0^2 \cos\left(\frac{\Omega}{2} t\right) + c_2(t) \omega_0^2 \sin\left(\frac{\Omega}{2} t\right) \\
& + \frac{1}{2} c_1(t) \omega_0^2 A \cos\left(\frac{3\Omega}{2} t\right) + \frac{1}{2} c_1(t) \omega_0^2 A \cos\left(\frac{\Omega}{2} t\right) \\
& + \frac{1}{2} c_2(t) \omega_0^2 A \sin\left(\frac{3\Omega}{2} t\right) - \frac{1}{2} c_2(t) \omega_0^2 A \sin\left(\frac{\Omega}{2} t\right)
\end{aligned} \tag{F.16}$$

In eq. F.16 we neglect the fast terms $\sin\left(\frac{3\Omega}{2} t\right)$ and $\cos\left(\frac{3\Omega}{2} t\right)$, because $c_1(t)$ and $c_2(t)$ are supposed to vary slowly compared to $\frac{\Omega}{2}$ [186]:

$$\begin{aligned}
0 = & \left(-2\dot{c}_1(t) \frac{\Omega}{2} - c_2(t) \frac{\Omega^2}{4} + c_2(t) \omega_0^2 - \frac{1}{2} c_2(t) \omega_0^2 A\right) \sin\left(\frac{\Omega}{2} t\right) \\
& + \left(-c_1(t) \frac{\Omega^2}{4} + 2\dot{c}_2(t) \frac{\Omega}{2} + c_1(t) \omega_0^2 + \frac{1}{2} c_1(t) \omega_0^2 A\right) \cos\left(\frac{\Omega}{2} t\right)
\end{aligned} \tag{F.17}$$

$$\begin{aligned}
= & -\left(\dot{c}_1(t) \Omega + c_2(t) \left(\frac{\Omega^2}{4} - \omega_0^2 + \frac{\omega_0^2 A}{2}\right)\right) \sin\left(\frac{\Omega}{2} t\right) \\
& + \left(\dot{c}_2(t) \Omega - c_1(t) \left(\frac{\Omega^2}{4} - \omega_0^2 - \frac{\omega_0^2 A}{2}\right)\right) \cos\left(\frac{\Omega}{2} t\right)
\end{aligned} \tag{F.18}$$

Since eq. F.18 has to be satisfied at all times, the pre-factors of $\sin(\frac{\Omega}{2}t)$ and $\cos(\frac{\Omega}{2}t)$ have to vanish:

$$0 = \dot{c}_1(t) \Omega + c_2(t) \left(\frac{\Omega^2}{4} - \omega_0^2 + \frac{\omega_0^2 A}{2} \right) \quad (\text{F.19})$$

$$= \dot{c}_1(t) + c_2(t) \left(\frac{\Omega}{4} - \frac{\omega_0^2}{\Omega} + \frac{\omega_0^2 A}{2\Omega} \right) \quad (\text{F.20})$$

$$= \dot{c}_1(t) + c_2(t) \left(\frac{2\omega_0 + \varepsilon}{4} - \frac{\omega_0^2}{2\omega_0 + \varepsilon} + \frac{\omega_0^2 A}{4\omega_0 + 2\varepsilon} \right) \quad (\text{F.21})$$

$$\approx \dot{c}_1(t) + c_2(t) \left(\frac{\omega_0}{2} + \frac{\varepsilon}{4} - \frac{\omega_0}{2} + \frac{\omega_0 A}{4} \right) \quad (\text{F.22})$$

$$0 = \dot{c}_1(t) + c_2(t) \left(\frac{\varepsilon}{4} + \frac{\omega_0 A}{4} \right) \quad (\text{F.23})$$

$$\dot{c}_1(t) = -c_2(t) \left(\frac{\varepsilon}{4} + \frac{\omega_0 A}{4} \right) \quad (\text{F.24})$$

$$0 = \dot{c}_2(t) \Omega - c_1(t) \left(\frac{\Omega^2}{4} - \omega_0^2 - \frac{\omega_0 A}{2} \right) \quad (\text{F.25})$$

$$\dot{c}_2(t) = c_1(t) \left(\frac{\varepsilon}{4} - \frac{\omega_0 A}{4} \right) \quad (\text{F.26})$$

We can now differentiate once more and then insert eqs. F.24 and F.26 into eqs. F.27 and F.28, respectively:

$$\ddot{c}_2(t) = \dot{c}_1(t) \left(\frac{\varepsilon}{4} - \frac{\omega_0 A}{4} \right) \quad (\text{F.27})$$

$$\ddot{c}_1(t) = -\dot{c}_2(t) \left(\frac{\varepsilon}{4} + \frac{\omega_0 A}{4} \right) \quad (\text{F.28})$$

$$\ddot{c}_1(t) = -c_1(t) \left(\frac{\varepsilon}{4} - \frac{\omega_0 A}{4} \right) \left(\frac{\varepsilon}{4} + \frac{\omega_0 A}{4} \right) \quad (\text{F.29})$$

$$= -\frac{1}{16} c_1(t) (\varepsilon^2 - \omega_0^2 A^2) \quad (\text{F.30})$$

$$= \frac{1}{16} c_1(t) (\omega_0^2 A^2 - \varepsilon^2) \quad (\text{F.31})$$

$$\ddot{c}_2(t) = -c_2(t) \left(\frac{\varepsilon}{4} - \frac{\omega_0 A}{4} \right) \left(\frac{\varepsilon}{4} + \frac{\omega_0 A}{4} \right) \quad (\text{F.32})$$

$$= \frac{1}{16} c_2(t) (\omega_0^2 A^2 - \varepsilon^2) \quad (\text{F.33})$$

F.3 Mapping to Bogoliubov Hamiltonian

We can map the quantum mechanical parametric oscillator onto the Bogoliubov Hamiltonian. We will show this by mapping onto Hamiltonian 2.43. Starting from the quantum mechanical version of the parametric oscillator (eq. 2.148),

$$\hat{H} = \frac{\hat{p}^2}{2m} + \frac{1}{2} m \omega_0^2 (1 + \alpha \cos(\Omega t)) \hat{x}^2,$$

we introduce a standard annihilation operator $\hat{\gamma}$:

$$\hat{\gamma} := \sqrt{\frac{m \omega_0}{2}} \left(\hat{x} + i \frac{\hat{p}}{m \omega_0} \right) \quad (\text{F.34})$$

$$\Rightarrow \hat{\gamma}^\dagger = \sqrt{\frac{m \omega_0}{2}} \left(\hat{x} - i \frac{\hat{p}}{m \omega_0} \right) \quad (\text{F.35})$$

$$\Rightarrow \hat{x} = \sqrt{\frac{1}{2m \omega_0}} (\hat{\gamma}^\dagger + \hat{\gamma}) \quad (\text{F.36})$$

$$\Rightarrow \hat{p} = i \sqrt{\frac{m \omega_0}{2}} (\hat{\gamma}^\dagger - \hat{\gamma}) \quad (\text{F.37})$$

$$1 = [\hat{\gamma}, \hat{\gamma}^\dagger] \quad (\text{F.38})$$

To insert eqs. F.36 and F.37 in the Hamiltonian, we square them:

$$\hat{x}^2 = \frac{1}{2m \omega_0} (\hat{\gamma}^\dagger + \hat{\gamma})^2 \quad (\text{F.39})$$

$$= \frac{1}{2m \omega_0} (\hat{\gamma}^\dagger \hat{\gamma}^\dagger + \hat{\gamma}^\dagger \hat{\gamma} + \hat{\gamma} \hat{\gamma}^\dagger + \hat{\gamma} \hat{\gamma}) \quad (\text{F.40})$$

$$= \frac{1}{2m \omega_0} (\hat{\gamma}^\dagger \hat{\gamma}^\dagger + 2\hat{\gamma}^\dagger \hat{\gamma} + \hat{\gamma} \hat{\gamma} + 1) \quad (\text{F.41})$$

$$\hat{p}^2 = -\frac{m \omega_0}{2} (\hat{\gamma}^\dagger - \hat{\gamma})^2 \quad (\text{F.42})$$

$$= -\frac{m \omega_0}{2} (\hat{\gamma}^\dagger \hat{\gamma}^\dagger - 2\hat{\gamma}^\dagger \hat{\gamma} + \hat{\gamma} \hat{\gamma} - 1) \quad (\text{F.43})$$

Now we can insert \hat{x}^2 and \hat{p}^2 (eqs. F.41 and F.43) in eq. 2.148:

$$\hat{H} = -\frac{1}{2m} \frac{m\omega_0}{2} (\hat{\gamma}^\dagger \hat{\gamma}^\dagger - 2\hat{\gamma}^\dagger \hat{\gamma} + \hat{\gamma} \hat{\gamma} - 1) \quad (\text{F.44})$$

$$+ \frac{1}{2} m \omega_0^2 (1 + \alpha \cos(\Omega t)) \frac{1}{2m\omega_0} (\hat{\gamma}^\dagger \hat{\gamma}^\dagger + 2\hat{\gamma}^\dagger \hat{\gamma} + \hat{\gamma} \hat{\gamma} + 1) \quad (\text{F.45})$$

$$= \frac{\omega_0}{4} (-\hat{\gamma}^\dagger \hat{\gamma}^\dagger + 2\hat{\gamma}^\dagger \hat{\gamma} - \hat{\gamma} \hat{\gamma} + 1) \quad (\text{F.46})$$

$$+ \frac{\omega_0}{4} (1 + \alpha \cos(\Omega t)) (\hat{\gamma}^\dagger \hat{\gamma}^\dagger + 2\hat{\gamma}^\dagger \hat{\gamma} + \hat{\gamma} \hat{\gamma} + 1) \quad (\text{F.47})$$

$$= \frac{\omega_0}{4} (4\hat{\gamma}^\dagger \hat{\gamma} + 2) + \frac{\alpha\omega_0}{4} \cos(\Omega t) (\hat{\gamma}^\dagger \hat{\gamma}^\dagger + 2\hat{\gamma}^\dagger \hat{\gamma} + \hat{\gamma} \hat{\gamma} + 1) \quad (\text{F.48})$$

$$\hat{H} = \omega_0 \left(1 + \frac{\alpha}{2} \cos(\Omega t)\right) \left(\hat{\gamma}^\dagger \hat{\gamma} + \frac{1}{2}\right) + \frac{\alpha\omega_0}{4} \cos(\Omega t) (\hat{\gamma}^\dagger \hat{\gamma}^\dagger + \hat{\gamma} \hat{\gamma}) \quad (\text{F.49})$$

All that is left to do now is shifting the Hamiltonian by the time-dependent vacuum energy $\frac{\omega_0}{2} (1 + \frac{\alpha}{2} \cos(\Omega t))$:

$$\hat{H}_{\text{para}} = \omega_0 \left(1 + \frac{\alpha}{2} \cos(\Omega t)\right) \hat{\gamma}^\dagger \hat{\gamma} + \frac{\alpha\omega_0}{4} \cos(\Omega t) (\hat{\gamma}^\dagger \hat{\gamma}^\dagger + \hat{\gamma} \hat{\gamma}) \quad (\text{F.50})$$

Bogoliubov-de Gennes Equations of Motion

The Bogoliubov-de Gennes formalism can be used to get the time-evolution of the condensates' excitations. We start with Heisenberg's equations of motion (EOM) for the annihilation operator \hat{b}_q and then perform the Bogoliubov transformation.

We use Hamiltonian 2.43 in the Heisenberg's EOM and for $q \neq 0$ we get [164]:

$$\hat{H} = -\frac{gN_0}{2} + \sum_{q>0} \left((\varepsilon_q^0 + g) (\hat{b}_q^\dagger \hat{b}_q + \hat{b}_{-q}^\dagger \hat{b}_{-q}) + g (\hat{b}_q^\dagger \hat{b}_{-q}^\dagger + \hat{b}_q \hat{b}_{-q}) \right)$$

$$i \hbar \partial_t \hat{b}_q(t) = [\hat{b}_q(t), \hat{H}(t)] \quad (\text{G.1})$$

$$= \left[\hat{b}_q(t), -\frac{gN_0}{2} + \sum_{q'>0} \left((\varepsilon_{q'}^0 + g) (\hat{b}_{q'}^\dagger(t) \hat{b}_{q'}(t) + \hat{b}_{-q'}^\dagger(t) \hat{b}_{-q'}(t)) + g (\hat{b}_{q'}^\dagger(t) \hat{b}_{-q'}^\dagger(t) + \hat{b}_{q'}(t) \hat{b}_{-q'}(t)) \right) \right] \quad (\text{G.2})$$

$$= \left[\hat{b}_q(t), \sum_{q' \neq 0} \left((\varepsilon_{q'}^0 + g) \hat{b}_{q'}^\dagger(t) \hat{b}_{q'}(t) \right) \right] + \left[\hat{b}_q(t), \sum_{q' \neq 0} \left(\frac{g}{2} (\hat{b}_{q'}^\dagger(t) \hat{b}_{-q'}^\dagger(t) + \hat{b}_{q'}(t) \hat{b}_{-q'}(t)) \right) \right] \quad (\text{G.3})$$

$$= (\varepsilon_q^0 + g) [\hat{b}_q, \hat{b}_q^\dagger(t)] \hat{b}_q(t) + \frac{g}{2} [\hat{b}_q(t), \hat{b}_q^\dagger(t) \hat{b}_{-q}^\dagger(t) + \hat{b}_{-q}^\dagger(t) \hat{b}_q^\dagger(t)] \quad (\text{G.4})$$

$$= (\varepsilon_q^0 + g) \hat{b}_q(t) + g [\hat{b}_q(t), \hat{b}_q^\dagger(t)] \hat{b}_{-q}^\dagger(t) \quad (\text{G.5})$$

$$i \hbar \partial_t \hat{b}_q(t) = (\varepsilon_q^0 + g) \hat{b}_q(t) + g \hat{b}_{-q}^\dagger(t) \quad (\text{G.6})$$

At this point, we perform the Bogoliubov transformation (eqs. 2.49 and 2.50) and put the time dependence into the factors u_q and v_q :

$$\begin{aligned}\hat{b}_q(t) &= u_q(t) \hat{\alpha}_q - v_q(t) \hat{\alpha}_{-q}^\dagger \\ \hat{b}_{-q}(t) &= u_q(t) \hat{\alpha}_{-q} - v_q(t) \hat{\alpha}_q^\dagger\end{aligned}$$

$$i\hbar \partial_t \hat{b}_q = i\hbar \partial_t (u_q(t) \hat{\alpha}_q - v_q(t) \hat{\alpha}_{-q}^\dagger) \quad (\text{G.7})$$

$$= i\hbar \partial_t u_q(t) \hat{\alpha}_q - i\hbar \partial_t v_q(t) \hat{\alpha}_{-q}^\dagger \quad (\text{G.8})$$

Here, we applied eq. 2.49. We can also use eq. G.6:

$$i\hbar \partial_t \hat{b}_q = (\varepsilon_q^0 + g) (u_q(t) \hat{\alpha}_q - v_q(t) \hat{\alpha}_{-q}^\dagger) + g (u_q(t) \hat{\alpha}_{-q}^\dagger - v_q(t) \hat{\alpha}_q) \quad (\text{G.9})$$

$$= \left((\varepsilon_q^0 + g) u_q(t) - g v_q(t) \right) \hat{\alpha}_q + \left(g u_q(t) - (\varepsilon_q^0 + g) v_q(t) \right) \hat{\alpha}_{-q}^\dagger \quad (\text{G.10})$$

By comparing coefficients of $\hat{\alpha}_q$ in eqs. G.8 and G.10, we arrive at the coupled equations of motion for u_q and v_q , the Bogoliubov-de Gennes (BdG) equations:

$$i\hbar \partial_t \begin{pmatrix} u_q(t) \\ v_q(t) \end{pmatrix} = \begin{pmatrix} \varepsilon_q^0 + g & -g \\ g & -\varepsilon_q^0 - g \end{pmatrix} \begin{pmatrix} u_q(t) \\ v_q(t) \end{pmatrix} \quad (\text{G.11})$$

Weak Coupling Conserving Approximation

The Weak coupling conserving approximation (WCCA) builds on the Bogoliubov model, but also restores the global $U(1)$ -symmetry associated with particle conservation [190]. It works in momentum space, so we assume a finite number of equal sites with periodic boundary conditions. In particular, this means that the trap has to be neglected and the condensate is carried by the $p = 0$ mode completely. Within the WCCA, we define new annihilation operators $\hat{\beta}_q(t)$ in a manner so their expectation value always vanishes:

$$\hat{b}_{q=0}(t) := \sqrt{N_0(t)} + \hat{\beta}_{q=0}(t) \quad (\text{H.1})$$

$$\hat{b}_{q \neq 0}(t) := \hat{\beta}_{q \neq 0}(t) \quad (\text{H.2})$$

The quantities of interest are the order parameter (i.e. condensate mode in momentum space) $\Phi(t)$ and the quasiparticle correlators $F_{11}(t, \mathbf{q})$ and $F_{12}(t, \mathbf{q})$, which are defined according to [190]:

$$\Phi(t) := \langle \hat{b}_{q=0}(t) \rangle = \sqrt{N_0(t)} \quad (\text{H.3})$$

$$F_{11}(t, \mathbf{q}) := \frac{1}{2} \langle \{ \hat{b}_q(t), \hat{b}_q^\dagger(t) \} \rangle_C = \frac{1}{2} \langle \{ \hat{\beta}_q(t), \hat{\beta}_q^\dagger(t) \} \rangle \quad (\text{H.4})$$

$$F_{12}(t, \mathbf{q}) := \langle \{ \hat{b}_q(t), \hat{b}_{-q}^\dagger(t) \} \rangle_C = \langle \{ \hat{\beta}_q(t), \hat{\beta}_{-q}^\dagger(t) \} \rangle, \quad (\text{H.5})$$

where $\langle \cdot \rangle_C$ denotes the correlation function $\langle \hat{A}\hat{B} \rangle_C = \langle \hat{A}\hat{B} \rangle - \langle \hat{A} \rangle \langle \hat{B} \rangle$, $\langle \cdot \rangle$ the expectation value and $\{ \cdot, \cdot \}$ the anti-commutator. If we minimize the effective action of the Bose-Hubbard model with respect to the order parameter and these correlators as shown in the supplementary material of [190], we get the following system of coupled integro-differential equations:

$$i\hbar \partial_t \Phi(t) = \left(\varepsilon_{q_{\text{BEC}}}(t) - \mu(t) \right) \Phi(t) + \frac{U}{N_s} \left(\Phi(t)^* \Phi(t)^2 + 2\Phi(t) \sum_{q'} F_{11}(t, q') + \Phi(t)^* \sum_{q'} F_{12}(t, q') \right) \quad (\text{H.6})$$

$$\hbar \partial_t F_{11}(t, \mathbf{q}) = 2 \text{Im} \left(\frac{U}{N_s} \left(\Phi(t)^2 + \sum_{q'} F_{12}(t, q') \right) F_{12}(t, \mathbf{q})^* \right) \quad (\text{H.7})$$

$$i\hbar \partial_t F_{12}(t, \mathbf{q}) = \left(\varepsilon_q(t) + \varepsilon_{-q}(t) - 2\mu(t) \right) F_{12}(t, \mathbf{q}) + 2 \frac{U}{N_s} \left(2 \left(|\Phi(t)|^2 + \sum_{q'} F_{11}(t, q') \right) F_{12}(t, \mathbf{q}) + \left(\Phi(t)^2 + \sum_{q'} F_{12}(t, q') \right) F_{11}(t, \mathbf{q}) \right) \quad (\text{H.8})$$

Because the chemical potential $\mu(t)$ is real, it has no effect on observables in the WCCA equations of motion. In the Bogoliubov-de Gennes formalism however, it is crucial since it fixes the condensate background for the described quasi-particle excitations. To compare the two schemes, it makes sense to fix the chemical potential to $\mu(t) = \varepsilon_{q_{\text{BEC}}}(t) + g$.

It is interesting to note what happens if the summation terms $\sum_{q'}$ are neglected in eqs. H.6 to H.8: From eq. H.6 we recover the Gross-Pitaevskii equation in the presence of the periodic drive (manifesting itself in the time-dependence of $\varepsilon_{q_{\text{BEC}}}(t)$). Using the definition eq. H.3 it follows that (neglecting the summations $\sum_{q'}$):

$$\partial_t F_{11}(t, \mathbf{q}) = \frac{1}{2} \left(|u_q(t)|^2 + |v_q(t)|^2 \right) \quad (\text{H.9})$$

$$\partial_t F_{12}(t, \mathbf{q}) = u_q(t) v_q(t), \quad (\text{H.10})$$

making the system equivalent to the Bogoliubov-de Gennes system again. From there it is easy to convince oneself that it is these summation terms that provide the necessary coupling to restore $U(1)$ -symmetry and thus particle number N_0 conservation in the model.

$$\begin{aligned} N_0 &= |\Phi(t)|^2 + \sum_q n_q(t) \\ &= |\Phi(t)|^2 + \sum_q \left(F_{11}(t, \mathbf{q}) - \frac{1}{2} \right) \end{aligned} \quad (\text{H.11})$$

It is not possible to find simple analytical solutions to the WCCA EOM due to their non-locality in momentum space. Also, because collisions of quasi-particles are not modeled (they happen at $\mathcal{O}(U^2)$), the system cannot thermalize at long times and the model is bound to fail in the prediction of the later stages of time-evolution. However, we have to point out that a description at $\mathcal{O}(U^2)$ has recently been done [251, 252].

Truncated Wigner Approximation

The Truncated Wigner approximation (TWA) is a particle number conserving semi-classical model that has the advantage of being more easy to analyze than full-quantum models like for example BdG and WCCA [253, 254]. It is well suited for the kind of situation present in this work as the condensate is in the superfluid phase, which is well described also by the classical GPE (see chap. 2.3). Also, it is capable of describing thermalization and recent works indicate that thermalization works alike in classical and the respective quantum systems [255–257].

In a homogeneous system with periodic boundary conditions, the classical ground state of the condensate is the $q=0$ mode and the dynamics can be described by the GPE-like equation:

$$i\hbar \partial_t \Phi(t) = (\epsilon_q(t) - \mu(t)) \Phi(t) + U_0 |\Phi(t)|^2 \Phi(t), \quad (\text{I.1})$$

where like in the WCCA, the chemical potential $\mu(t)$ is irrelevant to any observable and only adds an overall energy offset.

To go from classical to semi-classical, we can model the finite quantum mechanical occupation of higher modes (quantum depletion) in a statistical way.

We start from the quantum mechanical operator \hat{a}_j that annihilates a particle on site j :

$$\hat{a}_j = \frac{1}{\sqrt{N_s}} \hat{b}_{q=0} + \frac{1}{\sqrt{N_s}} \sum_{q \neq 0} \hat{b}_q e^{-i \frac{q}{\hbar} R_j} \quad (\text{I.2})$$

$$= \frac{1}{\sqrt{N_s}} \hat{b}_{q=0} + \frac{1}{\sqrt{N_s}} \sum_{q \neq 0} (u_q \hat{\gamma}_q e^{-i \frac{q}{\hbar} R_j} - v_q \hat{\gamma}_{-q}^\dagger e^{-i \frac{q}{\hbar} R_j}), \quad (\text{I.3})$$

where N_s is the number of sites or momentum states and $\hat{\gamma}_q$ denotes the annihilation operator of Bogoliubov mode q . We can classically model the order parameter $\langle \hat{a}_j \rangle$ on site j via the mean $\overline{a_j^k}$ of the classical ensemble a_j^k , where k runs over the ensemble. Also, the annihilation operator of the ground state is approximated by its expectation value $\hat{b}_{q=0} \approx \sqrt{N_0}$ and the mean density $n := \sqrt{\frac{N_0}{N_s}}$ is introduced:

$$a_j^k = \sqrt{n} + \frac{1}{\sqrt{N_s}} \sum_{q \neq 0} (u_q \gamma_q^k e^{-i \frac{q}{\hbar} R_j} - v_q^* \gamma_{-q}^{k*} e^{-i \frac{q}{\hbar} R_j}) \quad (\text{I.4})$$

Mean and variance of the Gaussian distribution of γ_q^k are chosen in such a way that they correctly reproduce the quantum mechanical fluctuations up to quadratic order. The expectation value of any observable can now be calculated by time-evolving all realizations of a_j^k to the point of interest, evaluating the observable for each realization and averaging in the end.

Within TWA, collisions of quasi-particles are captured to some extent. However, because there are higher-order moments beyond the quadratic one captured in this model, the dynamics cannot be exact within TWA. It is of course possible to extend the model to higher-order moments, but this is usually not done due to increasing complexity.

Bibliography

- [1] S. N. Bose. *Plancks Gesetz und Lichtquantenhypothese*. [Zeitschrift für Physik](#) **26**, 178–181 (1924). Cited on page: 2
- [2] A. Einstein. *Quantentheorie des einatomigen idealen Gases – Zweite Abhandlung*. Sitzungsberichte der preussischen Akademie der Wissenschaften (1925). Cited on page: 2
- [3] T. H. Maiman. *Stimulated Optical Radiation in Ruby*. [Nature](#) **187** (1960). Cited on page: 2
- [4] A. Einstein. *Strahlungs-Emission und Absorption nach der Quantentheorie*. Deutsche Physikalische Gesellschaft, Verhandlungen 18 (1916). Cited on page: 2
- [5] T. Hänsch and A. Schawlow. *Cooling of gases by laser radiation*. [Optics Communications](#) **13**, 68–69 (1975). Cited on page: 2
- [6] D. J. Wineland, R. E. Drullinger, and F. L. Walls. *Radiation-Pressure Cooling of Bound Resonant Absorbers*. [Physical Review Letters](#) **40**, 1639–1642 (1978). Cited on page: 2
- [7] E. L. Raab, M. Prentiss, A. Cable, S. Chu, and D. E. Pritchard. *Trapping of Neutral Sodium Atoms with Radiation Pressure*. [Physical Review Letters](#) **59**, 2631–2634 (1987). Cited on pages: 2, 48
- [8] M. H. Anderson, J. R. Ensher, M. R. Matthews, C. E. Wieman, and E. A. Cornell. *Observation of Bose-Einstein Condensation in a Dilute Atomic Vapor*. [Science](#) **269**, 198–201 (1995). Cited on page: 2
- [9] K. B. Davis, M. O. Mewes, M. R. Andrews, N. J. van Druten, D. S. Durfee, D. M. Kurn, and W. Ketterle. *Bose-Einstein Condensation in a Gas of Sodium Atoms*. [Physical Review Letters](#) **75**, 3969–3973 (1995). Cited on page: 46
- [10] C. C. Bradley, C. A. Sackett, J. J. Tollett, and R. G. Hulet. *Evidence of Bose-Einstein Condensation in an Atomic Gas with Attractive Interactions*. [Physical Review Letters](#) **75**, 1687–1690 (1995).
- [11] W. Ketterle, D. S. Durfee, and D. M. Stamper-Kurn. *Making, probing and understanding Bose-Einstein condensates*. [ArXiv](#) (1999). Cited on page: 57
- [12] I. Bloch, J. Dalibard, and W. Zwerger. *Many-body physics with ultracold gases*. [Reviews of Modern Physics](#) **80**, 885–964 (2008).

- [13] I. Bloch, J. Dalibard, and S. Nascimbène. *Quantum simulations with ultracold quantum gases*. *Nature Physics* **8**, 267–276 (2012). Cited on page: 2
- [14] B. DeMarco and D. S. Jin. *Onset of Fermi Degeneracy in a Trapped Atomic Gas*. *Science* **285**, 1703–1706 (1999). Cited on page: 2
- [15] T. Esslinger. *Fermi-Hubbard Physics with Atoms in an Optical Lattice*. *Annual Review of Condensed Matter Physics* **1**, 129–152 (2010). Cited on page: 2
- [16] T. Lahaye, C. Menotti, L. Santos, M. Lewenstein, and T. Pfau. *The physics of dipolar bosonic quantum gases*. *Reports on Progress in Physics* **72**, 126401 (2009). Cited on page: 2
- [17] J. G. Danzl, E. Haller, M. Gustavsson, M. J. Mark, R. Hart, N. Bouloufa, O. Dulieu, H. Ritsch, and H.-C. Nägerl. *Quantum Gas of Deeply Bound Ground State Molecules*. *Science* **321**, 1062–1066 (2008).
- [18] K.-K. Ni, S. Ospelkaus, M. H. G. de Miranda, A. Pe’er, B. Neyenhuis, J. J. Zirbel, S. Kotochigova, P. S. Julienne, D. S. Jin, and J. Ye. *A High Phase-Space-Density Gas of Polar Molecules*. *Science* **322**, 231–235 (2008). Cited on page: 2
- [19] M. Lewenstein, A. Sanpera, V. Ahufinger, B. Damski, A. Sen(De), and U. Sen. *Ultra-cold atomic gases in optical lattices: mimicking condensed matter physics and beyond*. *Advances in Physics* **56**, 243–379 (2007). Cited on page: 2
- [20] M. R. Matthews, B. P. Anderson, P. C. Haljan, D. S. Hall, C. E. Wieman, and E. A. Cornell. *Vortices in a Bose-Einstein Condensate*. *Physical Review Letters* **83**, 2498–2501 (1999). Cited on page: 2
- [21] K. W. Madison, F. Chevy, W. Wohlleben, and J. Dalibard. *Vortex Formation in a Stirred Bose-Einstein Condensate*. *Physical Review Letters* **84**, 806–809 (2000). Cited on page: 2
- [22] M. R. Andrews, D. M. Kurn, H.-J. Miesner, D. S. Durfee, C. G. Townsend, S. Inouye, and W. Ketterle. *Propagation of Sound in a Bose-Einstein Condensate*. *Physical Review Letters* **79**, 553–556 (1997). Cited on page: 2
- [23] D. M. Stamper-Kurn, A. P. Chikkatur, A. Görlitz, S. Inouye, S. Gupta, D. E. Pritchard, and W. Ketterle. *Excitation of Phonons in a Bose-Einstein Condensate by Light Scattering*. *Physical Review Letters* **83**, 2876–2879 (1999). Cited on page: 2
- [24] S. Inouye, M. R. Andrews, J. Stenger, H.-J. Miesner, D. M. Stamper-Kurn, and W. Ketterle. *Observation of Feshbach resonances in a Bose-Einstein condensate*. *Nature* **392**, 151–154 (1998). Cited on page: 2
- [25] C. Chin, R. Grimm, P. Julienne, and E. Tiesinga. *Feshbach resonances in ultracold gases*. *Reviews of Modern Physics* **82**, 1225–1286 (2010). Cited on pages: 2, 46

- [26] B. Paredes, A. Widera, V. Murg, O. Mandel, S. Fölling, I. Cirac, G. V. Shlyapnikov, T. W. Hänsch, and I. Bloch. *Tonks–Girardeau gas of ultracold atoms in an optical lattice*. *Nature* **429**, 277–281 (2004). Cited on page: 2
- [27] T. Kinoshita. *Observation of a One-Dimensional Tonks-Girardeau Gas*. *Science* **305**, 1125–1128 (2004). Cited on page: 2
- [28] W. S. Bakr, J. I. Gillen, A. Peng, S. Fölling, and M. Greiner. *A quantum gas microscope for detecting single atoms in a Hubbard-regime optical lattice*. *Nature* **462**, 74–77 (2009). Cited on page: 2
- [29] J. F. Sherson, C. Weitenberg, M. Endres, M. Cheneau, I. Bloch, and S. Kuhr. *Single-atom-resolved fluorescence imaging of an atomic Mott insulator*. *Nature* **467**, 68–72 (2010).
- [30] E. Haller, J. Hudson, A. Kelly, D. A. Cotta, B. Peaudecerf, G. D. Bruce, and S. Kuhr. *Single-atom imaging of fermions in a quantum-gas microscope*. *Nature Physics* **11**, 738–742 (2015).
- [31] M. F. Parsons, F. Huber, A. Mazurenko, C. S. Chiu, W. Setiawan, K. Wooley-Brown, S. Blatt, and M. Greiner. *Site-Resolved Imaging of Fermionic Li-6 in an Optical Lattice*. *Physical Review Letters* **114**, 213002 (2015).
- [32] A. Omran, M. Boll, T. A. Hilker, K. Kleinlein, G. Salomon, I. Bloch, and C. Gross. *Microscopic Observation of Pauli Blocking in Degenerate Fermionic Lattice Gases*. *Physical Review Letters* **115**, 263001 (2015).
- [33] G. J. A. Edge, R. Anderson, D. Jervis, D. C. McKay, R. Day, S. Trotzky, and J. H. Thywissen. *Imaging and addressing of individual fermionic atoms in an optical lattice*. *Physical Review A* **92**, 063406 (2015).
- [34] L. W. Cheuk, M. A. Nichols, M. Okan, T. Gersdorf, V. V. Ramasesh, W. S. Bakr, T. Lompe, and M. W. Zwierlein. *Quantum-Gas Microscope for Fermionic Atoms*. *Physical Review Letters* **114**, 193001 (2015). Cited on page: 2
- [35] C. Weitenberg, M. Endres, J. F. Sherson, M. Cheneau, P. Schauß, T. Fukuhara, I. Bloch, and S. Kuhr. *Single-spin addressing in an atomic Mott insulator*. *Nature* **471**, 319–324 (2011). Cited on page: 2
- [36] S. Eckel, D. S. Barker, J. A. Fedchak, N. N. Klimov, E. Norrgard, J. Scherschligt, C. Makrides, and E. Tiesinga. *Challenges to miniaturizing cold atom technology for deployable vacuum metrology*. *Metrologia* **55**, S182–S193 (2018). Cited on page: 2
- [37] G. Roati, E. de Mirandes, F. Ferlaino, H. Ott, G. Modugno, and M. Inguscio. *Atom Interferometry with Trapped Fermi Gases*. *Physical Review Letters* **92**, 230402 (2004). Cited on page: 2

- [38] Y. Shin, M. Saba, T. A. Pasquini, W. Ketterle, D. E. Pritchard, and A. E. Leanhardt. *Atom Interferometry with Bose-Einstein Condensates in a Double-Well Potential*. *Physical Review Letters* **92**, 050405 (2004).
- [39] D. A. Abanin, T. Kitagawa, I. Bloch, and E. Demler. *Interferometric Approach to Measuring Band Topology in 2D Optical Lattices*. *Physical Review Letters* **110**, 165304 (2013).
- [40] M. Atala, M. Aidelsburger, J. T. Barreiro, D. Abanin, T. Kitagawa, E. Demler, and I. Bloch. *Direct measurement of the Zak phase in topological Bloch bands*. *Nature Physics* **9**, 795–800 (2013). Cited on page: 2
- [41] S. L. Campbell, R. B. Hutson, G. E. Marti, A. Goban, N. Darkwah Oppong, R. L. McNally, L. Sonderhouse, J. M. Robinson, W. Zhang, B. J. Bloom, and J. Ye. *A Fermi-degenerate three-dimensional optical lattice clock*. *Science* **358**, 90–94 (2017). Cited on page: 2
- [42] C. Freier, M. Hauth, V. Schkolnik, B. Leykauf, M. Schilling, H. Wziontek, H.-G. Scherneck, J. Müller, and A. Peters. *Mobile quantum gravity sensor with unprecedented stability*. *Journal of Physics: Conference Series* **723**, 012050 (2016). Cited on page: 2
- [43] M.-K. Zhou, X.-C. Duan, L.-L. Chen, Q. Luo, Y.-Y. Xu, and Z.-K. Hu. *Micro-Gal level gravity measurements with cold atom interferometry*. *Chinese Physics B* **24**, 050401 (2015). Cited on page: 2
- [44] R. Bondarescu, M. Bondarescu, G. Hetényi, L. Boschi, P. Jetzer, and J. Balakrishna. *Geophysical applicability of atomic clocks: direct continental geoid mapping*. *Geophysical Journal International* **191**, 78–82 (2012). Cited on page: 2
- [45] M. Dransfield. *Airborne gravity gradiometry in the search for mineral deposits*. *Proceedings of exploration* **7** (2007). Cited on page: 2
- [46] S. Pollock, J. P. Cotter, A. Laliotis, and E. A. Hinds. *Integrated magneto-optical traps on a chip using silicon pyramid structures*. *Optics Express* **17**, 14109 (2009). Cited on page: 2
- [47] R. P. Feynman. *Simulating physics with computers*. *International Journal of Theoretical Physics* **21**, 467–488 (1982). Cited on page: 2
- [48] U.-J. Wiese. *Ultracold quantum gases and lattice systems: quantum simulation of lattice gauge theories*. *Annalen der Physik* **525**, 777–796 (2013). Cited on page: 2
- [49] E. Zohar, J. I. Cirac, and B. Reznik. *Quantum simulations of lattice gauge theories using ultracold atoms in optical lattices*. *Reports on Progress in Physics* **79**, 014401 (2016). Cited on page: 2

- [50] I. Bloch. *Ultracold quantum gases in optical lattices*. *Nature Physics* **1**, 23–30 (2005). Cited on page: 2
- [51] D. Jaksch, C. Bruder, J. I. Cirac, C. W. Gardiner, and P. Zoller. *Cold Bosonic Atoms in Optical Lattices*. *Physical Review Letters* **81**, 3108–3111 (1998). Cited on page: 2
- [52] L. Tarruell, D. Greif, T. Uehlinger, G. Jotzu, and T. Esslinger. *Creating, moving and merging Dirac points with a Fermi gas in a tunable honeycomb lattice*. *Nature* **483**, 302–305 (2012). Cited on page: 2
- [53] L. Duca, T. Li, M. Reitter, I. Bloch, M. Schleier-Smith, and U. Schneider. *An Aharonov-Bohm interferometer for determining Bloch band topology*. *Science* **347**, 288–292 (2015). Cited on pages: 2, 53
- [54] G. Wirth, M. Ölschläger, and A. Hemmerich. *Evidence for orbital superfluidity in the P-band of a bipartite optical square lattice*. *Nature Physics* **7**, 147–153 (2011). Cited on page: 2
- [55] C. Becker, P. Soltan-Panahi, J. Kronjäger, S. Dörscher, K. Bongs, and K. Sengstock. *Ultracold quantum gases in triangular optical lattices*. *New Journal of Physics* **12**, 065025 (2010). Cited on page: 2
- [56] G. B. Jo, J. Guzman, C. K. Thomas, P. Hosur, A. Vishwanath, and D. M. Stamper-Kurn. *Ultracold atoms in a tunable optical kagome lattice*. *Physical Review Letters* **108**, 1–5 (2012). Cited on page: 2
- [57] J. Hubbard. *Electron correlations in narrow energy bands*. *Proceedings of the Royal Society of London. Series A. Mathematical and Physical Sciences* **276**, 238–257 (1963). Cited on page: 2
- [58] M. Greiner, O. Mandel, T. Esslinger, T. W. Hänsch, and I. Bloch. *Quantum phase transition from a superfluid to a Mott insulator in a gas of ultracold atoms*. *Nature* **415**, 39–44 (2002). Cited on page: 2
- [59] J. Struck, C. Olschlager, R. Le Targat, P. Soltan-Panahi, A. Eckardt, M. Lewenstein, P. Windpassinger, and K. Sengstock. *Quantum Simulation of Frustrated Classical Magnetism in Triangular Optical Lattices*. *Science* **333**, 996–999 (2011). Cited on page: 2
- [60] Y.-J. Lin, R. L. Compton, K. Jiménez-García, J. V. Porto, and I. B. Spielman. *Synthetic magnetic fields for ultracold neutral atoms*. *Nature* **462**, 628–632 (2009). Cited on page: 2
- [61] M. Aidelsburger, M. Atala, S. Nascimbène, S. Trotzky, Y.-A. Chen, and I. Bloch. *Experimental realization of strong effective magnetic fields in optical superlattice potentials*. *Applied Physics B* **113**, 1–11 (2013). Cited on page: 2

- [62] M. Pasienski, D. McKay, M. White, and B. DeMarco. *A disordered insulator in an optical lattice*. [Nature Physics](#) **6**, 677–680 (2010). Cited on page: 2
- [63] G. Roati, C. D’Errico, L. Fallani, M. Fattori, C. Fort, M. Zaccanti, G. Modugno, M. Modugno, and M. Inguscio. *Anderson localization of a non-interacting Bose–Einstein condensate*. [Nature](#) **453**, 895–898 (2008). Cited on page: 2
- [64] M. White, M. Pasienski, D. McKay, S. Q. Zhou, D. Ceperley, and B. DeMarco. *Strongly Interacting Bosons in a Disordered Optical Lattice*. [Physical Review Letters](#) **102**, 055301 (2009). Cited on page: 2
- [65] P. W. Anderson. *Absence of Diffusion in Certain Random Lattices*. [Physical Review](#) **109**, 1492–1505 (1958). Cited on page: 2
- [66] J. Billy, V. Josse, Z. Zuo, A. Bernard, B. Hambrecht, P. Lugan, D. Clément, L. Sanchez-Palencia, P. Bouyer, and A. Aspect. *Direct observation of Anderson localization of matter waves in a controlled disorder*. [Nature](#) **453**, 891–894 (2008). Cited on page: 2
- [67] M. Schreiber, S. S. Hodgman, P. Bordia, H. P. Lüschen, M. H. Fischer, R. Vosk, E. Altman, U. Schneider, and I. Bloch. *Observation of many-body localization of interacting fermions in a quasirandom optical lattice*. [Science](#) **349**, 842–845 (2015). Cited on page: 2
- [68] P. Bordia, H. P. Lüschen, S. S. Hodgman, M. Schreiber, I. Bloch, and U. Schneider. *Coupling Identical one-dimensional Many-Body Localized Systems*. [Physical Review Letters](#) **116**, 140401 (2016).
- [69] J. Z. Imbrie. *On Many-Body Localization for Quantum Spin Chains*. [Journal of Statistical Physics](#) **163**, 998–1048 (2016).
- [70] H. P. Lüschen, P. Bordia, S. S. Hodgman, M. Schreiber, S. Sarkar, A. J. Daley, M. H. Fischer, E. Altman, I. Bloch, and U. Schneider. *Signatures of Many-Body Localization in a Controlled Open Quantum System*. [Physical Review X](#) **7**, 011034 (2017). Cited on page: 2
- [71] I. B. Spielman. *Detection of topological matter with quantum gases*. [Annalen der Physik](#) **525**, 797–807 (2013). Cited on page: 2
- [72] N. R. Cooper, J. Dalibard, and I. B. Spielman. *Topological Bands for Ultracold Atoms*. arXiv (2018). Cited on page: 2
- [73] J. B. Listing. *Vorstudien zur Topologie*. Vandenhoeck und Ruprecht, Göttingen (1848). Cited on page: 2
- [74] P. Wilson. *Curved Spaces: From Classical Geometries to Elementary Differential Geometry*. Cambridge University Press, Cambridge (2007). Cited on page: 2

- [75] K. V. Klitzing, G. Dorda, and M. Pepper. *New Method for High-Accuracy Determination of the Fine-Structure Constant Based on Quantized Hall Resistance*. *Physical Review Letters* **45**, 494–497 (1980). Cited on page: 2
- [76] M. Z. Hasan and C. L. Kane. *Colloquium : Topological insulators*. *Reviews of Modern Physics* **82**, 3045–3067 (2010). Cited on page: 3
- [77] X.-L. Qi and S.-C. Zhang. *Topological insulators and superconductors*. *Reviews of Modern Physics* **83**, 1057–1110 (2011).
- [78] M. Z. Hasan and J. E. Moore. *Three-Dimensional Topological Insulators*. *Annual Review of Condensed Matter Physics* **2**, 55–78 (2011).
- [79] J. E. Moore. *The birth of topological insulators*. *Nature* **464**, 194–198 (2010). Cited on page: 3
- [80] B. Jeckelmann and B. Jeanneret. *The quantum Hall effect as an electrical resistance standard*. *Reports on Progress in Physics* **64**, 1603–1655 (2001). Cited on page: 3
- [81] P. J. Mohr, B. N. Taylor, and D. B. Newell. *CODATA recommended values of the fundamental physical constants: 2010*. *Reviews of Modern Physics* **84**, 1527–1605 (2012). Cited on page: 3
- [82] M. V. Berry. *Quantal Phase Factors Accompanying Adiabatic Changes*. *Proceedings of the Royal Society A: Mathematical, Physical and Engineering Sciences* **392**, 45–57 (1984). Cited on page: 3
- [83] B. Simon. *Holonomy, the Quantum Adiabatic Theorem, and Berry's Phase*. *Physical Review Letters* **51**, 2167–2170 (1983).
- [84] F. Wilczek and A. Zee. *Appearance of Gauge Structure in Simple Dynamical Systems*. *Physical Review Letters* **52**, 2111–2114 (1984).
- [85] Y. Aharonov and J. Anandan. *Phase change during a cyclic quantum evolution*. *Physical Review Letters* **58**, 1593–1596 (1987). Cited on page: 3
- [86] R. Y. Chiao and Y. S. Wu. *Manifestations of Berry's topological phase for the photon*. *Physical Review Letters* **57**, 933–936 (1986). Cited on page: 3
- [87] P. G. Kwiat and R. Y. Chiao. *Observation of a nonclassical Berry's phase for the photon*. *Physical Review Letters* **66**, 588–591 (1991). Cited on page: 3
- [88] D. Suter, G. C. Chingas, R. A. Harris, and A. Pines. *Berry's phase in magnetic resonance*. *Molecular Physics* **61**, 1327–1340 (1987). Cited on page: 3
- [89] R. Tycko. *Adiabatic Rotational Splittings and Berry's Phase in Nuclear Quadrupole Resonance*. *Physical Review Letters* **58**, 2281–2284 (1987).

- [90] T. Bitter and D. Dubbers. *Manifestation of Berry's topological phase in neutron spin rotation*. *Physical Review Letters* **59**, 251–254 (1987). Cited on page: 3
- [91] E. Alba, X. Fernandez-Gonzalvo, J. Mur-Petit, J. K. Pachos, and J. J. Garcia-Ripoll. *Seeing Topological Order in Time-of-Flight Measurements*. *Physical Review Letters* **107**, 235301 (2011). Cited on page: 3
- [92] P. Hauke, M. Lewenstein, and A. Eckardt. *Tomography of Band Insulators from Quench Dynamics*. *Physical Review Letters* **113**, 045303 (2014). Cited on page: 3
- [93] N. Flaschner, B. S. Rem, M. Tarnowski, D. Vogel, D.-S. Luhmann, K. Sengstock, and C. Weitenberg. *Experimental reconstruction of the Berry curvature in a Floquet Bloch band*. *Science* **352**, 1091–1094 (2016). Cited on page: 3
- [94] S. Raghu, X. L. Qi, C. Honerkamp, and S. C. Zhang. *Topological mott insulators*. *Physical Review Letters* **100**, 1–4 (2008). Cited on pages: 3, 82
- [95] R. B. Laughlin. *Anomalous Quantum Hall Effect: An Incompressible Quantum Fluid with Fractionally Charged Excitations*. *Physical Review Letters* **50**, 1395–1398 (1983). Cited on page: 3
- [96] A. S. Sørensen, E. Demler, and M. D. Lukin. *Fractional Quantum Hall States of Atoms in Optical Lattices*. *Physical Review Letters* **94**, 086803 (2005). Cited on page: 3
- [97] N. R. Cooper and J. Dalibard. *Reaching fractional quantum hall states with optical flux lattices*. *Physical Review Letters* **110**, 1–5 (2013). Cited on page: 3
- [98] H. M. Price and N. R. Cooper. *Mapping the Berry curvature from semiclassical dynamics in optical lattices*. *Physical Review A* **85**, 033620 (2012). Cited on page: 3
- [99] A. Dauphin and N. Goldman. *Extracting the Chern Number from the Dynamics of a Fermi Gas: Implementing a Quantum Hall Bar for Cold Atoms*. *Physical Review Letters* **111**, 135302 (2013). Cited on page: 3
- [100] M. Killi, S. Trotzky, and A. Paramekanti. *Anisotropic quantum quench in the presence of frustration or background gauge fields: A probe of bulk currents and topological chiral edge modes*. *Physical Review A* **86**, 063632 (2012). Cited on page: 3
- [101] P. Delplace, D. Ullmo, and G. Montambaux. *Zak phase and the existence of edge states in graphene*. *Physical Review B* **84**, 195452 (2011). Cited on page: 3
- [102] N. Goldman, J. Dalibard, A. Dauphin, F. Gerbier, M. Lewenstein, P. Zoller, and I. B. Spielman. *Direct imaging of topological edge states in cold-atom systems*. *Proceedings of the National Academy of Sciences* **110**, 6736–6741 (2013).
- [103] B. Irsigler, J.-H. Zheng, and W. Hofstetter. *Interacting Hofstadter Interface*. *Physical Review Letters* **122**, 010406 (2019). Cited on page: 3

- [104] N. Goldman and J. Dalibard. *Periodically Driven Quantum Systems: Effective Hamiltonians and Engineered Gauge Fields*. *Physical Review X* **4**, 031027 (2014). Cited on pages: 3, 27, 28, 29
- [105] W. Zheng and H. Zhai. *Floquet topological states in shaking optical lattices*. *Physical Review A* **89**, 061603 (2014).
- [106] N. Goldman, J. C. Budich, and P. Zoller. *Topological quantum matter with ultracold gases in optical lattices*. *Nature Physics* **12**, 639–645 (2016).
- [107] T. Kitagawa, E. Berg, M. Rudner, and E. Demler. *Topological characterization of periodically driven quantum systems*. *Physical Review B* **82**, 235114 (2010). Cited on page: 3
- [108] G. Jotzu, M. Messer, R. Desbuquois, M. Lebrat, T. Uehlinger, D. Greif, and T. Esslinger. *Experimental realisation of the topological Haldane model*. *Nature* **515**, 14 (2014). Cited on page: 3
- [109] N. Fläschner, D. Vogel, M. Tarnowski, B. S. Rem, D.-S. Lühmann, M. Heyl, J. C. Budich, L. Mathey, K. Sengstock, and C. Weitenberg. *Observation of dynamical vortices after quenches in a system with topology*. *Nature Physics* **14**, 265–268 (2018).
- [110] F. D. M. Haldane. *Model for a Quantum Hall Effect without Landau Levels: Condensed-Matter Realization of the "Parity Anomaly"*. *Physical Review Letters* **61**, 2015–2018 (1988). Cited on page: 3
- [111] F. Gerbier and J. Dalibard. *Gauge fields for ultracold atoms in optical superlattices*. *New Journal of Physics* **12** (2010). Cited on page: 3
- [112] J. Dalibard, F. Gerbier, G. Juzeliūnas, and P. Öhberg. *Colloquium : Artificial gauge potentials for neutral atoms*. *Reviews of Modern Physics* **83**, 1523–1543 (2011).
- [113] P. Hauke, O. Tieleman, A. Celi, C. Ölschläger, J. Simonet, J. Struck, M. Weinberg, P. Windpassinger, K. Sengstock, M. Lewenstein, and A. Eckardt. *Non-Abelian Gauge Fields and Topological Insulators in Shaken Optical Lattices*. *Physical Review Letters* **109**, 145301 (2012).
- [114] J. Struck, C. Ölschläger, M. Weinberg, P. Hauke, J. Simonet, A. Eckardt, M. Lewenstein, K. Sengstock, and P. Windpassinger. *Tunable Gauge Potential for Neutral and Spinless Particles in Driven Optical Lattices*. *Physical Review Letters* **108**, 225304 (2012).
- [115] J. Struck, M. Weinberg, C. Ölschläger, P. Windpassinger, J. Simonet, K. Sengstock, R. Höppner, P. Hauke, A. Eckardt, M. Lewenstein, and L. Mathey. *Engineering Ising-XY spin-models in a triangular lattice using tunable artificial gauge fields*. *Nature Physics* **9**, 738–743 (2013).

- [116] N. Goldman, G. Juzeliūnas, P. Öhberg, and I. B. Spielman. *Light-induced gauge fields for ultracold atoms*. [Reports on Progress in Physics](#) **77**, 126401 (2014). Cited on page: 3
- [117] A. Hemmerich. *Effective time-independent description of optical lattices with periodic driving*. [Physical Review A](#) **81**, 063626 (2010). Cited on page: 3
- [118] T. Oka and H. Aoki. *Photovoltaic Hall effect in graphene*. [Physical Review B](#) **79**, 081406 (2009). Cited on page: 3
- [119] T. Kitagawa, T. Oka, A. Brataas, L. Fu, and E. Demler. *Transport properties of nonequilibrium systems under the application of light: Photoinduced quantum Hall insulators without Landau levels*. [Physical Review B](#) **84**, 235108 (2011).
- [120] N. H. Lindner, G. Refael, and V. Galitski. *Floquet topological insulator in semiconductor quantum wells*. [Nature Physics](#) **7**, 490–495 (2011). Cited on page: 3
- [121] C. Schweizer, F. Grusdt, M. Berngruber, L. Barbiero, E. Demler, N. Goldman, I. Bloch, and M. Aidelsburger. *Floquet approach to Z₂ lattice gauge theories with ultracold atoms in optical lattices*. arXiv (2019). Cited on page: 3
- [122] A. Stephenson. *On induced stability*. [The London, Edinburgh, and Dublin Philosophical Magazine and Journal of Science](#) **15**, 233–236 (1908). Cited on page: 3
- [123] N. Gemelke, E. Sarajlic, Y. Bidel, S. Hong, and S. Chu. *Parametric Amplification of Matter Waves in Periodically Translated Optical Lattices*. [Physical Review Letters](#) **95**, 170404 (2005). Cited on page: 3
- [124] H. Lignier, C. Sias, D. Ciampini, Y. Singh, A. Zenesini, O. Morsch, and E. Arimondo. *Dynamical Control of Matter-Wave Tunneling in Periodic Potentials*. [Physical Review Letters](#) **99**, 220403 (2007). Cited on pages: 3, 30
- [125] A. Eckardt, M. Holthaus, H. Lignier, A. Zenesini, D. Ciampini, O. Morsch, and E. Arimondo. *Exploring dynamic localization with a Bose-Einstein condensate*. [Physical Review A - Atomic, Molecular, and Optical Physics](#) **79**, 1–7 (2009). Cited on page: 3
- [126] B. J. Keay, S. Zeuner, S. J. Allen, K. D. Maranowski, A. C. Gossard, U. Bhattacharya, and M. J. W. Rodwell. *Dynamic localization, absolute negative conductance, and stimulated, multiphoton emission in sequential resonant tunneling semiconductor superlattices*. [Physical Review Letters](#) **75**, 4102–4105 (1995). Cited on page: 3
- [127] M. Holthaus. *Collapse of minibands in far-infrared irradiated superlattices*. [Physical Review Letters](#) **69**, 351–354 (1992).
- [128] X.-G. Zhao. *The suppression of a Bloch band in a driving laser field*. [Journal of Physics: Condensed Matter](#) **6**, 2751–2756 (1994).

- [129] K. Drese and M. Holthaus. *Ultracold atoms in modulated standing light waves*. *Chemical Physics* **217**, 201–219 (1997). Cited on page: 3
- [130] D. H. Dunlap and V. M. Kenkre. *Dynamic localization of a charged particle moving under the influence of an electric field*. *Physical Review B* **34**, 3625–3633 (1986). Cited on pages: 3, 30
- [131] K. W. Madison, M. C. Fischer, R. B. Diener, Q. Niu, and M. G. Raizen. *Dynamical Bloch band suppression in an optical lattice*. *Physical Review Letters* **81**, 5093–5096 (1998). Cited on page: 3
- [132] T. Meier, G. von Plessen, P. Thomas, and S. Koch. *Coherent effects induced by static and time-dependent electric fields in semiconductors*. *Physical Review B* **51** (1995). Cited on page: 3
- [133] A. Eckardt, C. Weiss, and M. Holthaus. *Superfluid-Insulator Transition in a Periodically Driven Optical Lattice*. *Physical Review Letters* **95**, 260404 (2005). Cited on page: 3
- [134] A. Zenesini, H. Lignier, D. Ciampini, O. Morsch, and E. Arimondo. *Coherent Control of Dressed Matter Waves*. *Physical Review Letters* **102**, 100403 (2009). Cited on page: 3
- [135] A. Lazarides, A. Das, and R. Moessner. *Equilibrium states of generic quantum systems subject to periodic driving*. *Physical Review E* **90**, 012110 (2014). Cited on page: 3
- [136] L. D’Alessio and M. Rigol. *Long-time Behavior of Isolated Periodically Driven Interacting Lattice Systems*. *Physical Review X* **4**, 041048 (2014). Cited on page: 3
- [137] S. Choudhury and E. J. Mueller. *Stability of a Floquet Bose-Einstein condensate in a one-dimensional optical lattice*. *Physical Review A* **90**, 013621 (2014). Cited on page: 3
- [138] S. Choudhury and E. J. Mueller. *Transverse collisional instabilities of a Bose-Einstein condensate in a driven one-dimensional lattice*. *Physical Review A* **91**, 023624 (2015).
- [139] S. Choudhury and E. J. Mueller. *Stability of a Bose-Einstein condensate in a driven optical lattice: Crossover between weak and tight transverse confinement*. *Physical Review A* **92**, 063639 (2015).
- [140] T. Bilitewski and N. R. Cooper. *Scattering theory for Floquet-Bloch states*. *Physical Review A - Atomic, Molecular, and Optical Physics* **91**, 1–20 (2015).
- [141] T. Bilitewski and N. R. Cooper. *Population dynamics in a Floquet realization of the Harper-Hofstadter Hamiltonian*. *Physical Review A* **91**, 063611 (2015). Cited on page: 3

- [142] D. T. Tran, A. Dauphin, A. G. Grushin, P. Zoller, and N. Goldman. *Probing topology by “heating”: Quantized circular dichroism in ultracold atoms*. *Science Advances* **3**, e1701207 (2017). Cited on page: 3
- [143] L. Asteria, D. T. Tran, T. Ozawa, M. Tarnowski, B. S. Rem, N. Fläschner, K. Sengstock, N. Goldman, and C. Weitenberg. *Measuring quantized circular dichroism in ultracold topological matter*. arXiv (2018). Cited on page: 3
- [144] T. Boulier, J. Maslek, M. Bukov, C. Bracamontes, E. Magnan, S. Lellouch, E. Demler, N. Goldman, and J. V. Porto. *Parametric instabilities in a 2D periodically-driven bosonic system: Beyond the weakly-interacting regime*. arXiv (2018). Cited on page: 4
- [145] M. Reitter. *Scattering processes in interacting Floquet systems*. PhD Thesis (2017). Cited on pages: 4, 6
- [146] M. Reitter, J. Näger, K. Wintersperger, C. Sträter, I. Bloch, A. Eckardt, and U. Schneider. *Interaction Dependent Heating and Atom Loss in a Periodically Driven Optical Lattice*. *Physical Review Letters* **119**, 1–6 (2017). Cited on pages: 6, 21, 31, 60, 103, 104
- [147] C. J. Smith and H. Pethick. *Bose-Einstein Condensation in Dilute Gases Bose-Einstein Condensation in Dilute Gases*. Cambridge U. Press, New York (2002). Cited on pages: 7, 14, 15, 16, 20, 78, 91, 95, 98
- [148] L. Pitaevskii and S. Stringari. *Bose-Einstein condensation (International series of monographs on physics)*. Clarendon Press, Oxford (2003). Cited on pages: 7, 14
- [149] D. Becker, M. D. Lachmann, S. T. Seidel, H. Ahlers, A. N. Dinkelaker, J. Grosse, O. Hellmig, H. Müntinga, V. Schkolnik, T. Wendrich, A. Wenzlawski, B. Weps, R. Corgier, T. Franz, N. Gaaloul, W. Herr, D. Lüdtkke, M. Popp, S. Amri, H. Duncker, M. Erbe, A. Kohfeldt, A. Kubelka-Lange, C. Braxmaier, E. Charron, W. Ertmer, M. Krutzik, C. Lämmerzahl, A. Peters, W. P. Schleich, K. Sengstock, R. Walser, A. Wicht, P. Windpassinger, and E. M. Rasel. *Space-borne Bose-Einstein condensation for precision interferometry*. *Nature* **562**, 391–395 (2018). Cited on page: 8
- [150] T. van Zoest, N. Gaaloul, Y. Singh, H. Ahlers, W. Herr, S. T. Seidel, W. Ertmer, E. Rasel, M. Eckart, E. Kajari, S. Arnold, G. Nandi, W. P. Schleich, R. Walser, A. Vogel, K. Sengstock, K. Bongs, W. Lewoczko-Adamczyk, M. Schiemangk, T. Schuldt, A. Peters, T. Konemann, H. Müntinga, C. Lämmerzahl, H. Dittus, T. Steinmetz, T. W. Hansch, and J. Reichel. *Bose-Einstein Condensation in Microgravity*. *Science* **328**, 1540–1543 (2010). Cited on page: 8
- [151] J. Stark. *Weitere Resultate über den Effekt des elektrischen Feldes auf Spektrallinien*. *Annalen der Physik* **2**, 145–148 (1914). Cited on pages: 8, 51

- [152] L. J. Hornbeck. *Multi-level digital micromirror device* (1993). Cited on page: 8
- [153] S. Bergamini, B. Darquié, M. Jones, L. Jacubowicz, A. Browaeys, and P. Grangier. *Holographic generation of microtrap arrays for single atoms by use of a programmable phase modulator*. *Journal of the Optical Society of America B* **21**, 1889 (2004). Cited on page: 8
- [154] C. Kittel. *Einführung in die Festkörperphysik*. Oldenbourg Wissenschaftsverlag, München, 14 edition (2006). Cited on pages: 9, 10, 11, 87, 88, 89, 90
- [155] F. Bloch. *Über die Quantenmechanik der Elektronen in Kristallgittern*. *Zeitschrift für Physik* **52**, 555–600 (1929).
- [156] G. Floquet. *Sur les équations différentielles linéaires à coefficients périodiques*. *Annales scientifiques de l'École normale supérieure* **12**, 47–88 (1883). Cited on pages: 9, 24
- [157] E. Noether. *Invarianten beliebiger Differentialausdrücke*. *Gött. Nachr.* (1918). Cited on page: 9
- [158] C. E. Shannon. *A Mathematical Theory of Communication*. *Bell System Technical Journal* **27**, 379–423 (1948). Cited on page: 10
- [159] N. Marzari, A. A. Mostofi, J. R. Yates, I. Souza, and D. Vanderbilt. *Maximally localized Wannier functions: Theory and applications*. *Reviews of Modern Physics* **84**, 1419–1475 (2012). Cited on page: 12
- [160] G. H. Wannier. *The structure of electronic excitation levels in insulating crystals*. *Physical Review* **52**, 191–197 (1937). Cited on page: 12
- [161] W. Kohn and L. J. Sham. *Self-Consistent Equations Including Exchange and Correlation Effects*. *Physical Review* **140**, A1133–A1138 (1965). Cited on page: 12
- [162] A. Altland and B. Simons. *Condensed Matter Field Theory*. University Press, Cambridge, fourth edition (2009). Cited on pages: 18, 19
- [163] H. A. Gersch and G. C. Knollman. *Quantum cell model for bosons*. *Physical Review* **129**, 959–967 (1963). Cited on page: 19
- [164] S. Lellouch, M. Bukov, E. Demler, and N. Goldman. *Parametric instability rates in periodically driven band systems*. *Physical Review X* **7**, 1–32 (2017). Cited on pages: 19, 29, 36, 37, 38, 39, 41, 60, 82, 112, 123
- [165] F. Dalfovo, S. Giorgini, L. P. Pitaevskii, and S. Stringari. *Theory of Bose-Einstein condensation in trapped gases*. *Reviews of Modern Physics* **71**, 463–512 (1999). Cited on pages: 21, 103

- [166] S. Arlinghaus and M. Holthaus. *Driven optical lattices as strong-field simulators*. *Physical Review A* **81**, 063612 (2010). Cited on page: 24
- [167] J. H. Shirley. *Solution of the Schrödinger Equation with a Hamiltonian Periodic in Time*. *Physical Review* **138**, B979–B987 (1965). Cited on page: 24
- [168] H.-P. Breuer and F. Petruccione. *The Theory of open quantum systems*. Clarendon Press, Oxford (2010). Cited on page: 24
- [169] A. Eckardt. *Colloquium: Atomic quantum gases in periodically driven optical lattices*. *Reviews of Modern Physics* **89**, 1–30 (2017). Cited on pages: 24, 25, 26, 27, 28
- [170] C. Cohen-Tannoudji, J. Dupont-Roc, and G. Grynberg. *Atom-Photon Interactions: Basic Processes and Applications*. Wiley-VCH (1998). Cited on page: 25
- [171] F. Gesztesy and H. Mitter. *A note on quasi-periodic states*. *Journal of Physics A: Mathematical and General* **14**, L79–L83 (1981). Cited on page: 26
- [172] W. R. Salzman. *Quantum mechanics of systems periodic in time*. *Physical Review A* **10**, 461–465 (1974). Cited on page: 27
- [173] A. Eckardt and E. Anisimovas. *High-frequency approximation for periodically driven quantum systems from a Floquet-space perspective*. *New Journal of Physics* **17** (2015). Cited on page: 28
- [174] S. Rahav, I. Gilary, and S. Fishman. *Effective Hamiltonians for periodically driven systems*. *Physical Review A* **68**, 013820 (2003).
- [175] T. P. Grozdanov and M. J. Raković. *Quantum system driven by rapidly varying periodic perturbation*. *Physical Review A* **38**, 1739–1746 (1988). Cited on page: 28
- [176] M. M. Maricq. *Application of average Hamiltonian theory to the NMR of solids*. *Physical Review B* **25**, 6622–6632 (1982). Cited on page: 28
- [177] K. F. Milfeld and R. E. Wyatt. *Study, extension, and application of Floquet theory for quantum molecular systems in an oscillating field*. *Phys. Rev. A* **27** (1983).
- [178] F. Casas, J. A. Oteo, and J. Ros. *Floquet theory: exponential perturbative treatment*. *Journal of Physics A: Mathematical and General* **34** (2001). Cited on page: 28
- [179] M. Bukov, L. D’Alessio, and A. Polkovnikov. *Universal high-frequency behavior of periodically driven systems: From dynamical stabilization to Floquet engineering*. *Advances in Physics* **64**, 139–226 (2015). Cited on pages: 28, 29, 112
- [180] P. A. M. Dirac. *The Quantum Theory of the Emission and Absorption of Radiation*. *Proceedings of the Royal Society A: Mathematical, Physical and Engineering Sciences* **114**, 243–265 (1927). Cited on page: 30

- [181] F. Schwabl. *Quantenmechanik (QM I)*. Springer Verlag, Berlin, 7. auflage edition (2007). Cited on page: 30
- [182] W. Magnus and S. Winkler. *Hill's Equation*. Interscience Publishers John Wiley & Sons, New York, London, Sydney (1966). Cited on page: 33
- [183] G. Teschl. *Ordinary Differential Equations and Dynamical Systems*. American Mathematical Society, Wien (2012). Cited on page: 33
- [184] G. W. Hill. *On the part of the motion of the lunar perigee which is a function of the mean motions of the sun and moon*. *Acta Mathematica* **8**, 1–36 (1886). Cited on page: 33
- [185] P. Kapitza. *Dynamical Stability of a Pendulum When its Point of Suspension Vibrates*. *Sov. Phys. JETP* **21** (1951). Cited on page: 33
- [186] W. Demtröder. *Experimentalphysik 1*. Springer-Lehrbuch. Springer Berlin Heidelberg, Berlin, Heidelberg (2015). Cited on pages: 33, 35, 118, 119
- [187] W. B. Case and M. A. Swanson. *The pumping of a swing from the seated position*. *American Journal of Physics* **58**, 463–467 (1990). Cited on page: 34
- [188] W. B. Case. *The pumping of a swing from the standing position*. *American Journal of Physics* **64**, 215–220 (1996). Cited on page: 34
- [189] C. E. Creffield. *Instability and control of a periodically driven Bose-Einstein condensate*. *Physical Review A - Atomic, Molecular, and Optical Physics* **79**, 1–5 (2009). Cited on pages: 37, 38
- [190] M. Bukov, S. Gopalakrishnan, M. Knap, and E. Demler. *Prethermal Floquet Steady States and Instabilities in the Periodically Driven, Weakly Interacting Bose-Hubbard Model*. *Physical Review Letters* **115**, 205301 (2015). Cited on pages: 38, 125
- [191] L. D. Landau and E. M. Lifshitz. *Theoretical Physics - Vol. 1 Mechanics*. Pergamon Press, New York (1969). Cited on page: 38
- [192] J. Näger, K. Wintersperger, M. Bukov, S. Lellouch, E. Demler, U. Schneider, I. Bloch, N. Goldman, and M. Aidelsburger. *Parametric instabilities of interacting bosons in periodically-driven 1D optical lattices*. arXiv pages 1–18 (2018). Cited on pages: 38, 39, 40, 53, 64, 70, 73, 74, 75, 76, 77, 80
- [193] L. Duca. *Probing topological properties of Bloch bands with ultracold atoms in a honeycomb optical lattice*. PhD Thesis (2015). Cited on page: 44
- [194] L. Duca. *Probing topological properties of Bloch bands with ultracold atoms in a honeycomb optical lattice*. PhD thesis, Ludwig-Maximilians-Universität (2015). Cited on page: 45

- [195] S. Chaudhuri, S. Roy, and C. S. Unnikrishnan. *Realization of an intense cold Rb atomic beam based on a two-dimensional magneto-optical trap: Experiments and comparison with simulations.* *Physical Review A* **74**, 023406 (2006). Cited on page: 45
- [196] K. Dieckmann, R. J. C. Spreeuw, M. Weidemüller, and J. T. M. Walraven. *Two-dimensional magneto-optical trap as a source of slow atoms.* *Physical Review A* **58**, 3891–3895 (1998).
- [197] J. Catani, P. Maioli, L. De Sarlo, F. Minardi, and M. Inguscio. *Intense slow beams of bosonic potassium isotopes.* *Physical Review A* **73**, 033415 (2006).
- [198] J. Schoser, A. Batär, R. Löw, V. Schweikhard, A. Grabowski, Y. B. Ovchinnikov, and T. Pfau. *Intense source of cold Rb atoms from a pure two-dimensional magneto-optical trap.* *Physical Review A* **66**, 023410 (2002).
- [199] T. G. Tiecke, S. D. Gensemer, A. Ludewig, and J. T. M. Walraven. *High-flux two-dimensional magneto-optical-trap source for cold lithium atoms.* *Physical Review A* **80**, 013409 (2009). Cited on page: 45
- [200] W. Ketterle, K. B. Davis, M. A. Joffe, A. Martin, and D. E. Pritchard. *High densities of cold atoms in a dark spontaneous-force optical trap.* *Physical Review Letters* **70**, 2253–2256 (1993). Cited on page: 45
- [201] W. Petrich, M. H. Anderson, J. R. Ensher, and E. A. Cornell. *Behavior of atoms in a compressed magneto-optical trap.* *Journal of the Optical Society of America B* **11**, 1332 (1994). Cited on page: 46
- [202] C. Fort, A. Bambini, L. Cacciapuoti, F. Cataliotti, M. Prevedelli, G. Tino, and M. Inguscio. *Cooling mechanisms in potassium magneto-optical traps.* *The European Physical Journal D - Atomic, Molecular and Optical Physics* **3**, 113–118 (1998). Cited on page: 46
- [203] M. Landini, S. Roy, L. Carcagní, D. Trypogeorgos, M. Fattori, M. Inguscio, and G. Modugno. *Sub-Doppler laser cooling of potassium atoms.* *Physical Review A* **84**, 043432 (2011). Cited on pages: 46, 48
- [204] M. Greiner, I. Bloch, T. W. Hänsch, and T. Esslinger. *Magnetic transport of trapped cold atoms over a large distance.* *Physical Review A* **63**, 031401 (2001). Cited on page: 46
- [205] E. Majorana. *Teoria Relativistica di Particelle Con Momento Intrinseco Arbitrario.* *Il Nuovo Cimento* **9**, 335–344 (1932). Cited on page: 46
- [206] D. S. Naik and C. Raman. *Optically plugged quadrupole trap for Bose-Einstein condensates.* *Physical Review A* **71**, 033617 (2005).

- [207] D. M. Brink and C. V. Sukumar. *Majorana spin-flip transitions in a magnetic trap*. *Physical Review A* **74**, 035401 (2006). Cited on page: 46
- [208] A. L. Migdall, J. V. Prodan, W. D. Phillips, T. H. Bergeman, and H. J. Metcalf. *First Observation of Magnetically Trapped Neutral Atoms*. *Physical Review Letters* **54**, 2596–2599 (1985). Cited on page: 46
- [209] L. De Sarlo, P. Maioli, G. Barontini, J. Catani, F. Minardi, and M. Inguscio. *Collisional properties of sympathetically cooled ^{39}K* . *Physical Review A* **75**, 022715 (2007). Cited on page: 46
- [210] S. Chu, J. E. Bjorkholm, A. Ashkin, and A. Cable. *Experimental Observation of Optically Trapped Atoms*. *Physical Review Letters* **57**, 314–317 (1986). Cited on page: 46
- [211] J. Weiner, V. S. Bagnato, S. Zilio, and P. S. Julienne. *Experiments and theory in cold and ultracold collisions*. *Reviews of Modern Physics* **71**, 1–85 (1999). Cited on pages: 46, 48
- [212] H. Feshbach. *Unified Theory of Nuclear Reactions*. *Reviews of Modern Physics* **36**, 1076–1078 (1964). Cited on pages: 46, 52
- [213] F. Ferlaino, C. D’Errico, G. Roati, M. Zaccanti, M. Inguscio, G. Modugno, and A. Simoni. *Feshbach spectroscopy of a K-Rb atomic mixture*. *Physical Review A* **73**, 040702 (2006).
- [214] G. Roati, M. Zaccanti, C. D’Errico, J. Catani, M. Modugno, A. Simoni, M. Inguscio, and G. Modugno. *^{39}K Bose-Einstein Condensate with Tunable Interactions*. *Physical Review Letters* **99**, 010403 (2007). Cited on pages: 46, 47
- [215] C. D’Errico, M. Zaccanti, M. Fattori, G. Roati, M. Inguscio, G. Modugno, and A. Simoni. *Feshbach resonances in ultracold ^{39}K* . *New Journal of Physics* **9**, 223–223 (2007). Cited on page: 47
- [216] D. E. Pritchard, E. L. Raab, V. Bagnato, C. E. Wieman, and R. N. Watts. *Light Traps Using Spontaneous Forces*. *Physical Review Letters* **57**, 310–313 (1986). Cited on page: 48
- [217] M. Vangeleyn, P. F. Griffin, E. Riis, and A. S. Arnold. *Single-laser, one beam, tetrahedral magneto-optical trap*. *Optics Express* **17**, 13601 (2009). Cited on page: 48
- [218] D. A. Steck. *Rubidium 87D Line Data*. Technical report, Los Alamos National Laboratory, Los Alamos (2001). Cited on pages: 48, 49
- [219] T. G. Tiecke. *Properties of Potassium*. *Physics* **02**, 1–14 (2010). Cited on pages: 48, 49, 52

- [220] P. Zeeman. *On the influence of magnetism on the nature of the light emitted by a substance*. *The London, Edinburgh, and Dublin Philosophical Magazine and Journal of Science* **43**, 226–239 (1897). Cited on pages: 48, 50
- [221] V. Gokhroo, G. Rajalakshmi, R. K. Easwaran, and C. S. Unnikrishnan. *Sub-Doppler deep-cooled bosonic and fermionic isotopes of potassium in a compact 2D+ 3D MOT set-up*. *Journal of Physics B: Atomic, Molecular and Optical Physics* **44**, 115307 (2011). Cited on page: 48
- [222] R. Grimm, M. Weidemüller, and Y. B. Ovchinnikov. *Optical Dipole Traps for Neutral Atoms*. *Advances in Atomic, Molecular and Optical Physics* **42**, 95–170 (2000). Cited on page: 51
- [223] C. H. Townes and F. R. Merritt. *Stark Effect in High Frequency Fields*. *Physical Review* **72**, 1266–1267 (1947). Cited on page: 51
- [224] B. E. A. Saleh and M. C. Teich. *Grundlagen der Photonik*. Wiley-VCH, Berlin, 2. auflage edition (2008). Cited on page: 51
- [225] U. Fano. *Effects of Configuration Interaction on Intensities and Phase Shifts*. *Physical Review* **124**, 1866–1878 (1961). Cited on page: 52
- [226] a. J. Moerdijk, B. J. Verhaar, and A. Axelsson. *Resonances in ultracold collisions of 6-Li, 7-Li, and 23-Na*. *Physical Review A* **51**, 4852–4861 (1995). Cited on page: 52
- [227] E. Timmermans, P. Tommasini, M. Hussein, and A. Kerman. *Feshbach resonances in atomic Bose–Einstein condensates*. *Physics Reports* **315**, 199–230 (1999).
- [228] K. Góral, T. Köhler, S. A. Gardiner, E. Tiesinga, and P. S. Julienne. *Adiabatic association of ultracold molecules via magnetic-field tunable interactions*. *Journal of Physics B: Atomic, Molecular and Optical Physics* **37**, 3457–3500 (2004).
- [229] T. Köhler, K. Góral, and P. S. Julienne. *Production of cold molecules via magnetically tunable Feshbach resonances*. *Reviews of Modern Physics* **78**, 1311–1361 (2006). Cited on page: 52
- [230] A. Kastberg, W. D. Phillips, S. L. Rolston, R. J. C. Spreeuw, and P. S. Jessen. *Adiabatic Cooling of Cesium to 700 nK in an Optical Lattice*. *Physical Review Letters* **74**, 1542–1545 (1995). Cited on page: 56
- [231] M. Greiner, I. Bloch, O. Mandel, T. W. Hänsch, and T. Esslinger. *Exploring Phase Coherence in a 2D Lattice of Bose-Einstein Condensates*. *Physical Review Letters* **87**, 160405 (2001). Cited on page: 56
- [232] G. Reinaudi, T. Lahaye, Z. Wang, and D. Guéry-Odelin. *Strong saturation absorption imaging of dense clouds of ultracold atoms*. *Optics Letters* **32**, 3143 (2007). Cited on page: 57

- [233] M.-O. Mewes, M. R. Andrews, N. J. van Druten, D. M. Kurn, D. S. Durfee, C. G. Townsend, and W. Ketterle. *Collective Excitations of a Bose-Einstein Condensate in a Magnetic Trap*. *Physical Review Letters* **77**, 988–991 (1996). Cited on page: 60
- [234] D. S. Jin, J. R. Ensher, M. R. Matthews, C. E. Wieman, and E. A. Cornell. *Collective Excitations of a Bose-Einstein Condensate in a Dilute Gas*. *Physical Review Letters* **77**, 420–423 (1996). Cited on page: 60
- [235] I. Tamm. *Über eine mögliche Art der Elektronenbindung an Kristalloberflächen*. *Zeitschrift für Physik* **76**, 849–850 (1932). Cited on page: 76
- [236] F. Damon, B. Georgeot, and D. Guéry-Odelin. *Probing surface states with many-body wave packet scattering*. *EPL (Europhysics Letters)* **115**, 20010 (2016). Cited on page: 76
- [237] M. Babadi, M. Knap, I. Martin, G. Refael, and E. Demler. *Theory of parametrically amplified electron-phonon superconductivity*. *Physical Review B* **96**, 014512 (2017). Cited on page: 82
- [238] A. González-Tudela, C.-L. Hung, D. E. Chang, J. I. Cirac, and H. J. Kimble. *Sub-wavelength vacuum lattices and atom–atom interactions in two-dimensional photonic crystals*. *Nature Photonics* **9**, 320–325 (2015). Cited on page: 82
- [239] V. Peano, M. Houde, F. Marquardt, and A. A. Clerk. *Topological Quantum Fluctuations and Traveling Wave Amplifiers*. *Physical Review X* **6**, 041026 (2016). Cited on page: 82
- [240] K. Sun, Z. Gu, H. Katsura, and S. Das Sarma. *Nearly Flatbands with Nontrivial Topology*. *Physical Review Letters* **106**, 236803 (2011). Cited on page: 82
- [241] F. Wilczek. *Quantum Mechanics of Fractional-Spin Particles*. *Physical Review Letters* **49**, 957–959 (1982). Cited on page: 82
- [242] C. Nayak, S. H. Simon, A. Stern, M. Freedman, and S. Das Sarma. *Non-Abelian anyons and topological quantum computation*. *Reviews of Modern Physics* **80**, 1083–1159 (2008). Cited on page: 82
- [243] N. R. Cooper. *Optical Flux Lattices for Ultracold Atomic Gases*. *Physical Review Letters* **106**, 175301 (2011). Cited on page: 83
- [244] N. R. Cooper and J. Dalibard. *Optical flux lattices for two-photon dressed states*. *EPL (Europhysics Letters)* **95**, 66004 (2011). Cited on page: 83
- [245] N. Levy, S. A. Burke, K. L. Meaker, M. Panlasigui, A. Zettl, F. Guinea, A. H. C. Neto, and M. F. Crommie. *Strain-Induced Pseudo-Magnetic Fields Greater Than 300 Tesla in Graphene Nanobubbles*. *Science* **329**, 544–547 (2010). Cited on page: 83

- [246] V. M. Pereira, A. H. Castro Neto, and N. M. R. Peres. *Tight-binding approach to uniaxial strain in graphene*. *Physical Review B* **80**, 045401 (2009).
- [247] F. Guinea, M. I. Katsnelson, and A. K. Geim. *Energy gaps and a zero-field quantum Hall effect in graphene by strain engineering*. *Nature Physics* **6**, 30–33 (2010).
- [248] M. O. Goerbig. *Electronic properties of graphene in a strong magnetic field*. *Reviews of Modern Physics* **83**, 1193–1243 (2011). Cited on page: 83
- [249] G. Salerno, T. Ozawa, H. M. Price, and I. Carusotto. *How to directly observe Landau levels in driven-dissipative strained honeycomb lattices*. *2D Materials* **2**, 034015 (2015). Cited on page: 83
- [250] J. Stenger, S. Inouye, A. P. Chikkatur, D. M. Stamper-Kurn, D. E. Pritchard, and W. Ketterle. *Bragg Spectroscopy of a Bose-Einstein Condensate*. *Physical Review Letters* **82**, 4569–4573 (1999). Cited on page: 83
- [251] S. A. Weidinger and M. Knap. *Floquet prethermalization and regimes of heating in a periodically driven, interacting quantum system*. *Scientific Reports* **7**, 45382 (2017). Cited on page: 126
- [252] A. Chandran and S. L. Sondhi. *Interaction-stabilized steady states in the driven $O(N)$ model*. *Physical Review B* **93**, 174305 (2016). Cited on page: 126
- [253] P. Blakie, A. Bradley, M. Davis, R. Ballagh, and C. Gardiner. *Dynamics and statistical mechanics of ultra-cold Bose gases using c-field techniques*. *Advances in Physics* **57**, 363–455 (2008). Cited on page: 127
- [254] A. Polkovnikov. *Phase space representation of quantum dynamics*. *Annals of Physics* **325**, 1790–1852 (2010). Cited on page: 127
- [255] O. Howell, P. Weinberg, D. Sels, A. Polkovnikov, and M. Bukov. *Frequency-Controlled Thermalization Phase Transition in a Chaotic Periodically-Driven Classical Spin Chain*. ArXiv (2018). Cited on page: 127
- [256] A. Rajak, R. Citro, and E. G. Dalla Torre. *Stability and pre-thermalization in chains of classical kicked rotors*. *Journal of Physics A: Mathematical and Theoretical* **51**, 465001 (2018).
- [257] S. Notarnicola, F. Iemini, D. Rossini, R. Fazio, A. Silva, and A. Russomanno. *From localization to anomalous diffusion in the dynamics of coupled kicked rotors*. *Physical Review E* **97**, 022202 (2018). Cited on page: 127

Danksagung

Eine Doktorarbeit ist ein großes Projekt, das nicht alleine bewältigt werden kann. Ich möchte all den Leuten danken, die mir auf die ein oder andere Weise geholfen haben und durch die diese Arbeit erst möglich wurde:

Immanuel Bloch dafür, dass er mir die Promotion an seinem Lehrstuhl ermöglicht hat.

Ulrich Schneider dafür, dass er mich in seine Arbeitsgruppe aufgenommen und mich mit täglichem Coaching durch die ersten Monate geleitet hat.

Dem Fermi II Team um Lucia Duca, Tracy Li und Martin Reitter dafür, dass sie mich in ihr Team integriert und mir viele Fragen (auch mehrfach) beantwortet haben.

Martin Reitter dafür, dass er mehrere Jahre darauf verwendet hat, mir geduldig so viel wie möglich über den experimentellen Aufbau bei zu bringen.

Michael Schreiber, Henrik Lüschen und Martin Reitter dafür, dass sie sich viel Zeit genommen haben, mit mir fachliche Probleme zu erörtern und mich an ihrem reichen Erfahrungsschatz teilhaben ließen.

Karen Wintersperger für die gute Zusammenarbeit und die vorbildliche Arbeitsmoral.

Unseren Kollaborateuren Marin Bukov, Nathan Goldman, André Eckardt, Christoph Sträter, Samuel Lellouch und Eugene Demler für gute Arbeit in der Theorie und viel Geduld mit nicht funktionsfähigen Setups.

Marin Bukov, Nathan Goldman, André Eckardt für die Zeit, die sie sich genommen haben, um mir während des Verfassens der Dissertation vieles zu erklären, das ich schon vorher hätte verstehen sollen.

Monika Aidelsburger dafür, dass sie die Betreuung unseres Experiments mitten im laufenden Projekt übernommen und dieses zu einem guten Ende geführt hat.

Den Lektoren Monika Aidelsburger, Karen Wintersperger, Christoph Braun und Sebastian Scherg für das Korrekturlesen der Arbeit.

Monika Aidelsburger dafür, dass sie in den letzten Zügen des Schreibens meiner Arbeit viel Zeit auf die kleinen Details verwendet hat und das Niveau der Arbeit damit deutlich angehoben hat.

Dem Fermi I Team um Henrik Lüschen, Pranjal Bordia, Sean Hodgeman, Sebastian Scherg und Thomas Kohlert für ihr gut sortiertes Ersatzteillager, aus dem zahllose optische Komponenten für das Fermi II Experiment gestohlen wurden.

Ildiko Kecskesi dafür, dass sie den Lehrstuhl so gut im Griff hat und einem jedes organisatorische Problem abnimmt und zuverlässig löst.

Bodo Hecker dafür, dass er mir die Grundlagen der Elektronik beigebracht hat, seine Zeit für meine privaten Fortbildungsprojekte geopfert hat und dafür, dass er zuverlässig dafür sorgt, dass wir Doktoranden uns nicht mit unsachgemäß verbauter Hochspannung umbringen.

Henrik Lüschen, Martin Reitter, Sebastian Scherg und Thomas Kohlert dafür, dass sie stets wussten, wann die Mensa die richtige Anlaufstelle zum Mittagessen ist (immer).

Frau Baumgärtner dafür, dass sie mir in den ersten Monaten in München ein Dach (und einen Fußboden) über dem Kopf gegeben hat.

Rainer Dietrich dafür, dass er mich mit einem exzellenten Physik Leistungskurs hervorragend auf das Physikstudium vorbereitet hat.

Matthias Zorn dafür, dass er drei Jahre ein hervorragender Mitbewohner war, mit dem das Zusammenleben riesigen Spaß gemacht hat.

Meinen Eltern dafür, dass sie mich all die Jahre nach Kräften in meiner Ausbildung unterstützt und mir diese ermöglicht haben.

Meinem Papa dafür, dass er schon in jungen Jahren den Forscherdrang in mir geweckt hat.

Angela Huber dafür, dass sie mir während des Schreibens den Rücken frei gehalten und den Haushalt praktisch alleine geschmissen hat.

Zu guter Letzt dem gesamten Lehrstuhl Bloch für die gute Atmosphäre und vier tolle Jahre.